UNIVERSITÄT HAMBURG
FACHBEREICH PHYSIK

An experimental Test of Newton's Law of Gravitation for small Accelerations

Dissertation

zur Erlangung des Doktorgrades

des Fachbereichs Physik

der Universität Hamburg

vorgelegt von

Dipl.-Phys. Sven Schubert

aus Oschatz

Hamburg

2011

Gutachter der Dissertation:	Prof. Dr. Günter Sigl
	Prof. Dr. Hinrich Meyer
Gutachter der Disputation:	Prof. Dr. Günter Sigl
	Prof. Dr. Dieter Horns
Datum der Disputation:	12. Oktober 2011
Vorsitzender des Prüfungsausschusses:	Prof. Dr. Dieter Horns
Vorsitzender des Promotionsausschusses:	Prof. Dr. Peter H. Hauschildt
Leiterin des Fachbereichs Physik:	Prof. Dr. Daniela Pfannkuche
Dekan der MIN-Fakultät:	Prof. Dr. Heinrich Graener

Abstract

The experiment presented in this thesis has been designed to test Newton's law of gravitation in the limit of small accelerations caused by weak gravitational forces. It is located at DESY, Hamburg, and is a modification of an experiment that was carried out in Wuppertal, Germany, until 2002 in order to measure the gravitational constant G. The idea of testing Newton's law in the case of small acclerations emerged from the question whether the flat rotation curves of spiral galaxies can be traced back to Dark Matter or to a law of gravitation that deviates from Newton on cosmic scales like e.g. MOND (Modified Newtonian Dynamics).

The core of this experiment is a microwave resonator which is formed by two spherical concave mirrors that are suspended as pendulums. Masses between 1 and 9 kg symmetrically change their distance to the mirrors from far to near positions. Due to the increased gravitational force the mirrors are pulled apart and the length of the resonator increases. This causes a shift of the resonance frequency which can be translated into a shift of the mirror distance. The small masses are sources of weak gravitational forces and cause accelerations on the mirrors of about 10^{-10} m/s^2. These forces are comparable to those between stars on cosmic scales and the accelerations are in the vicinity of the characteristic acceleration of MOND $a_0 \approx 1.2 \cdot 10^{-10}$ m/s^2, where deviations from Newton's law are expected. Thus Newton's law could be directly checked for correctness under these conditions.

First measurements show that due to the sensitivity of this experiment many systematic influences have to be accounted for in order to get consistent results. Newton's law has been confirmed with an accuracy of 3%. MOND has also been checked. The interpolation function presented in [Bek05] respectively [Cap09] can be excluded. In order to be able to distinguish Newton from MOND with other interpolation functions the accuracy of the experiment has to be improved.

Zusammenfassung

Das in dieser Arbeit vorgestellte Experiment dient dazu, das Newtonsche Gravitationsgesetz im Grenzfall kleiner, gravitationsbedingter Beschleunigungen zu überprüfen. Es wurde am DESY in Hamburg aufgebaut und ist aus einem Experiment hervorgegangen, mit dem in Wuppertal die Gravitationskonstante G gemessen wurde. Hintergrund ist die Frage, ob die nach außen hin abflachenden Rotationskurven von Spiralgalaxien auf Dunkle Materie zurückzuführen sind oder auf ein Gravitationsgesetz, dass im Bereich kosmischer Skalen vom Newtonschen Gesetz abweicht wie z.B. MOND (Modified Newtionian Dynamics).

Herzstück des Experiments ist ein Mikrowellenresonator, der aus zwei sphärischen Hohlspiegeln besteht. Diese hängen sich als Pendel gegenüber. Massen zwischen 1 und 9 kg werden symmetrisch von einer entfernten Stellung an die Spiegel heranbewegt. Die von den Massen verursachte Gravitationskraft vergrößert sich und die Spiegel werden auseinander gezogen. Dadurch verschiebt sich die Resonanzfrequenz. Diese Frequenzverschiebung lässt sich in eine Abstandsänderung der Spiegel umrechnen. Die kleinen Massen sind Quellen schwacher Gravitationsfelder und verursachen Beschleunigungen von etwa 10^{-10} m/s^2 auf die Spiegel. Dies liegt im Bereich der für MOND charakteristischen Beschleunigung $a_0 \approx 1.2 \cdot 10^{-10}$ m/s^2 und ist vergleichbar mit den Beschleunigungen, die auf kosmischen Skalen vorherrschen und wo Abweichungen vom Newtonschen Gesetz erwartet werden. Das Newtonsche Gesetz kann somit direkt unter diesen Bedingungen geprüft werden.

Erste Messungen zeigen, dass das aufgrund der Empfindlichkeit des Experiments viele systematische Einflüsse berücksichtigt werden müssen, um konsistente Ergebnisse zu erhalten. Das Newtonsche Gesetz wurde mit einer Genauigkeit von 3% bestätigt. MOND wurde ebenfalls geprüft. Die Interpolationsfunktion aus [Bek05] bzw. [Cap09] kann ausgeschlossen werden. Um jedoch das Newtonsche Gesetz von MOND mit anderen Interpolationsfunktionen unterscheiden zu können, muss die Genauigkeit des Experiments erhöht werden.

Contents

Chapter 1

Motivation

In this chapter the motivation to test the law of gravitation at small acclerations is explained. The sections 1.1 to 1.3 are dedicated to develop the theoretical background that is necessary to understand the experiment. In Chap. 1.4 the process of measurement is discussed which, for the experiment, leads to important restrictions.

1.1 MOND

In [Mil83] M. Milgrom proposed an alternative theory of gravitation, called MOND (Modified Newtonian Dynamics) in order to explain large scale dynamics, like e.g. the motion of the stars within a galaxy (s.a. [Mil01] [Sca06] and [Bek06]). In contrast to the introduction of Dark Matter, Milgrom has suggested to alter the law of motion in a way that it describes galaxy dynamics without the need of extra matter. Unlike Newton's law of gravitation with its Poisson equation

$$\vec{\nabla} \cdot \vec{\nabla} \Phi(\vec{r}) = 4\pi G \, \rho(\vec{r}) \tag{1.1}$$

with $\Phi(\vec{r})$ as the gravitational potential, $\rho(\vec{r})$ as the matter density and G as the gravitational constant, the modified law of gravitation is governed by the field equation

$$\vec{\nabla} \cdot \left[\mu(|\vec{\nabla}\Phi_M(\vec{r})|/a_0) \, \vec{\nabla}\Phi_M(\vec{r}) \right] = 4\pi G \, \rho(\vec{r}) \tag{1.2}$$

with $\Phi_M(\vec{r})$ as the modified gravitational potential, $a_0 \approx 1.2 \cdot 10^{-10} \mathrm{m/s^2}$ as a new constant and the interpolation function $\mu(x)$ which has to satisfy the boundary conditions

$$\mu(x) \approx \begin{cases} 1 & \text{for} \quad x \gg 1 \\ x & \text{for} \quad x \ll 1 \end{cases} \tag{1.3}$$

with $x = a/a_0$ and $a = -\vec{\nabla}\Phi_M$. Apart from the boundary conditions (1.3), the interpolation function $\mu(x)$ has to be determined experimentally. Eq. (1.2) and

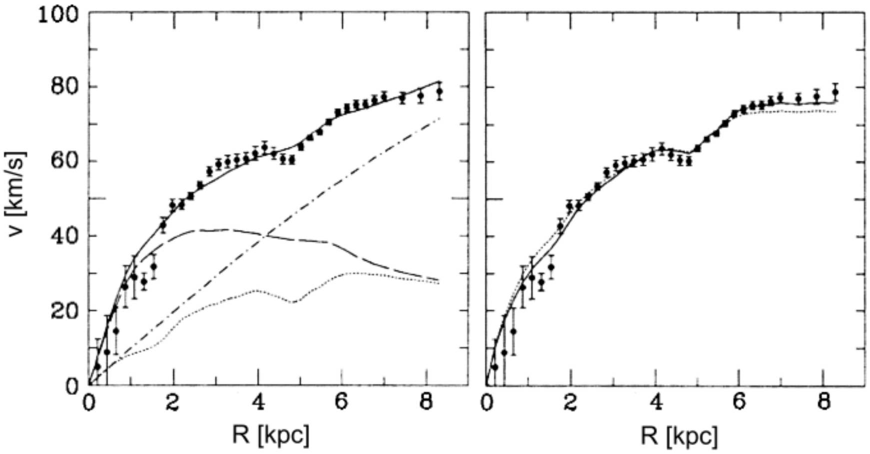

Figure 1.1: example rotation curves of the gas-dominated galaxy NGC 1560, i.e. the rotation velocity v plotted against the distance R from the center of the galaxy: **Left:** Three-parameter dark-matter halo fit (solid curve). The fit parameters are the mass-to-luminosity-ratio (M/L), the halo core radius and the halo asymptotic velocity. Also shown are the rotation curve for stellar (dashed), gas (dotted) and dark halo (dash-dotted). **Right:** MOND fits: one-parameter fit (dotted) with the M/L ratio as the fit parameter and two-parameter fit (solid curve) with the M/L ratio and the distance from the center of the galaxy. From [Sca06]

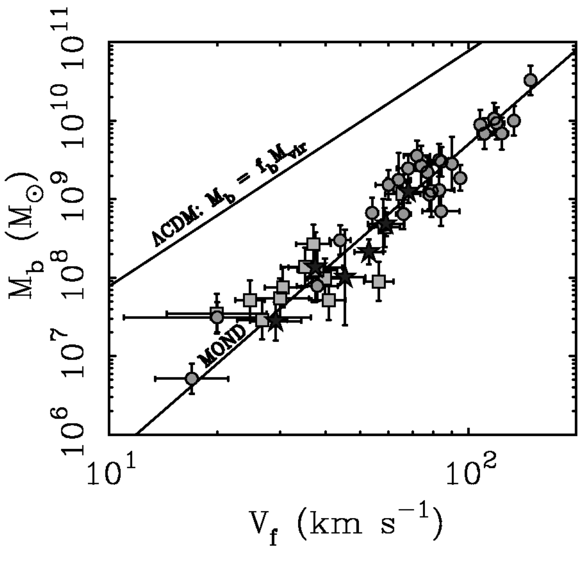

Figure 1.2: Tully-Fisher relation: Total baryonic mass M_b of disc galaxies plotted against the asymptotic rotational speed v_f. The upper line is the prediction of standard cosmology ΛCDM. The lower line is predicted by MOND. From [McG11]

(1.3) imply that Newton's law will only be a good approximation if $|\vec{\nabla}\Phi(\vec{r})| \gg a_0$ and therefore a_0 has the meaning of a threshold acceleration. Since MOND has been derived to explain the observations, it produces the flat rotation curves of spiral galaxies in a natural way (s. Fig. 1.1). As a non-trivial prediction it leads to the Tully-Fisher relation

$$M_b \propto v_f^{\beta}, \qquad \beta \approx 3.0 - 4.2 \tag{1.4}$$

with M_b as the baryonic mass of a spiral galaxy and v_f its asymptotic rotation speed (s. Fig. 1.2). This relation was empirically found by [Tul77].

Finally Milgrom pointed out the numerical relation

$$a_0 \approx cH_0 \tag{1.5}$$

which, according to him, suggests some deep connection between relativistic cosmology and the threshold acceleration a_0. If there is more behind that relation than merely a coincidence, the modifications that extend standard cosmology due to MOND may already be contained in standard cosmology itself since a_0 could be calculated by using only the constants c and the Hubble constant H_0.

1.2 Interpolation Functions

According to (1.3), MOND is undefined between the boundary conditions since (1.2) does not contain a rule to determine the interpolation function $\mu(x)$ that fulfills the conditions (1.3).

To narrow down the choice, first of all one has to demand that MOND, endowed with a specific interpolation function, has to be in accordance with the astrophysical observations. Interpolation functions that have been determined in this way are

$$\mu(x) = x/\sqrt{1+x^2} \tag{1.6}$$

and

$$\mu(x) = x/(1+x) \tag{1.7}$$

with $x = a/a_0$ and $a = -\vec{\nabla}\Phi_M$ the effective acceleration due to the modified gravitational potential Φ_M. The interpolation function (1.6) was primarily proposed by [Mil83] and is according to [Sca06] the most used function in the literature. The function (1.7) was mentioned in [Fam05].

However MOND defined by Eq. (1.2) and (1.3), with an interpolation function like (1.6) or (1.7), still gives rise to some questions. It is non-relativistic and above all, purely phenomenological. A relativistic generalization named *TeVeS*[1] has been proposed by [Bek05], extending general relativity with addional vector and

---

[1] TeVeS = abbr. for Tensor Vector Scalar

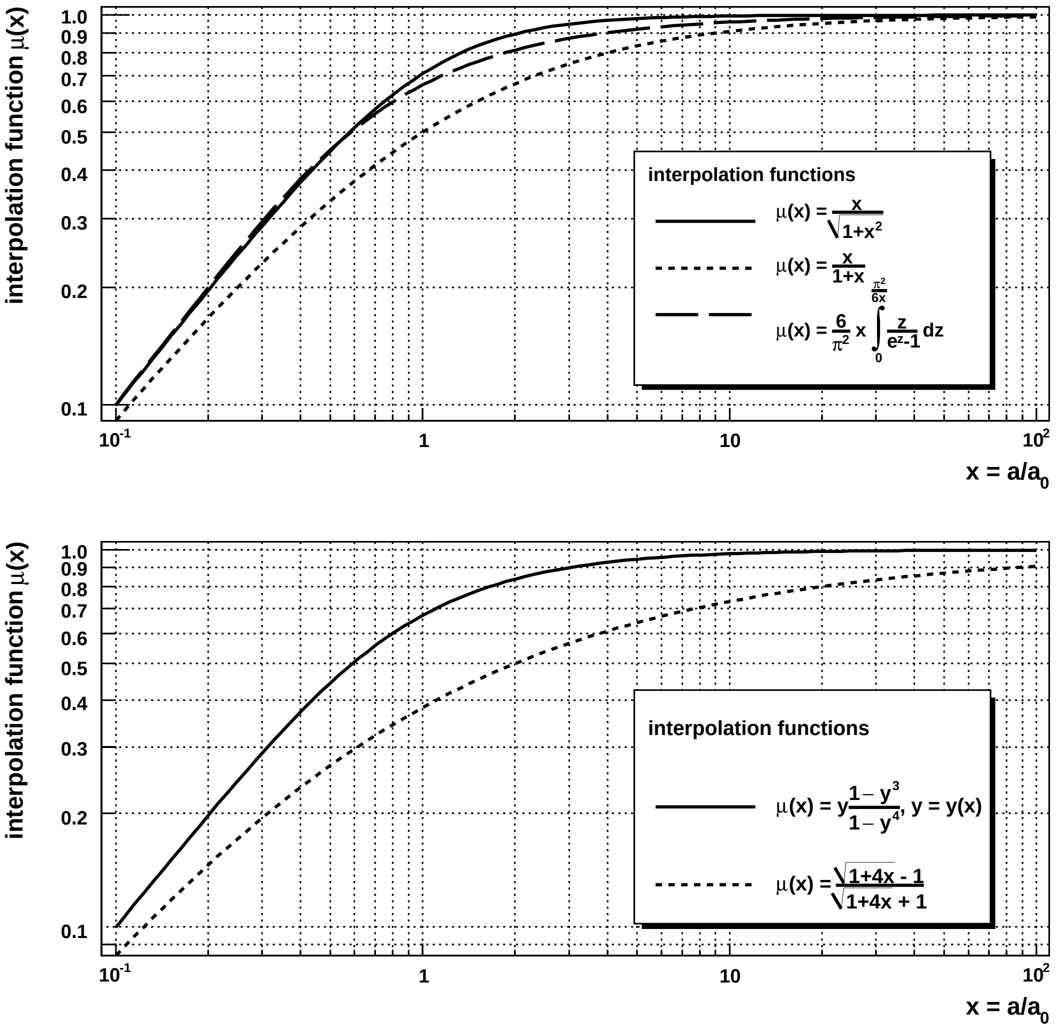

Figure 1.3: Interpolation functions $\mu(x)$ presented in Chap. 1.2, plotted against $x = a/a_0$ with $a = -\vec{\nabla}\Phi_M$ the effective acceleration due to the modified gravitational potential Φ_M.

scalar fields. In the non-relativistic limit, *TeVeS* yields an interpolation function $\mu(x)$ that strongly depends on these additional fields. A linearization in the case of spherically symmetric systems results in

$$\mu(x) = \frac{\sqrt{1+4x}-1}{\sqrt{1+4x}+1} \tag{1.8}$$

As shown in [Fam05], this interpolation function is not consistent with astrophysical observations concerning the Milky Way.

An alternative way that could result in a fundamental theory behaving like MOND in the non-relativistic case has been proposed by [Li10]. They adapted the idea of [Ver10] who assumed that each gravitational system within a specific volume is equivalent to a system of bits on the boundary of this volume. As a result of that kind of a holographic principle the gravitational force can be interpreted as an entropic force that only emerges at macroscopic scales. In addition [Li10] described the excitations of the bits on the boundary by a one dimensional Debye model. As a consequence of this, the law of gravitation will have to be modified in a way that within weak gravitational potentials it leads to (1.2) with the interpolation function

$$\mu(x) = \frac{6}{\pi^2} x \int_0^{\frac{\pi^2}{6x}} \frac{z}{e^z - 1}\, dz \tag{1.9}$$

This approach gives also rise to the relation (1.5). Further developments connected with entropic gravitation are mentioned e.g. in [Paz11].

A modified, still non-relativistic gravitational theory that is endowed with a broken scale invariance due to the appearance of a mass-length scale has been proposed by [Men10]. This theory results in MOND with the interpolation function

$$\mu(x) = y\,\frac{1-y^3}{1-y^4} \tag{1.10}$$

where $y = y(x)$ and has to be calculated by solving

$$x = y\,\frac{1-y^4}{1-y^3} \tag{1.11}$$

for y.

In [Cap09], an $f(R)$-gravity model is studied that in the case of a weak field approximation is equivalent to MOND with the interpolation function

$$\mu(x) = \frac{1+2x-\sqrt{1+4x}}{2x} \tag{1.12}$$

which is identical to (1.8).

1.3 MOND vs. Dark Matter

In contrast to MOND, the Dark Matter paradigm assumes that Newton's law of gravitation is valid. To be nonetheless in accord with the astrophysical observations, extra matter has to be introduced which only interacts gravitationally with ordinary matter. Since such extra matter has not been observed yet, it is called *Dark Matter*. It is assumed that within most of the galaxies the Dark Matter is distributed such that it encloses the galaxy like a halo. This idea was first proposed by [Zwi33].

Now the crucial question is: Has the law of gravitation to be modified or is Dark Matter the correct way? Both ways have their strong and weak points in explaining large scale dynamics. On the one hand MOND can not explain the dynamics within galaxy clusters as long as the distribution of hydrogen within the universe is estimated correctly. On the other hand Newton's law with Dark Matter fails to describe the motion of binary stars that are separated beyond 7000 AU so that the mutual accelerations are around a_0 (see [Her11]). The Tully-Fisher relation can not be reproduced as well (see Fig. 1.2). A comparison of both approaches can be found e.g. in [Bek06] and [Mil11]. Thus a lab-based experiment that can decide between Newton's law and MOND would be a valuable contribution to this debate.

1.4 Restrictions concerning Measurements

According to [Mil94], modified gravitation is not the only way of interpreting Eq. (1.2). It is also possible to consider MOND to be modified inertia. This approach leads to a non-local theory where the interpolation function $\mu(x)$ is not fixed but depends on the trajectory of the particle respectively on the experimental setup. That complicates the interpretation of measurements. However [Bek06] showed that in the case of interpreting MOND as modified inertia, the formula (1.2) does not conserve momentum, angular momentum and energy. Therefore modified intertia has to be rejected and Eq. (1.2) has to be read as modified gravitation.

An ambiguity still remains: Does $|\vec{\nabla}\Phi(\vec{r})| \approx a_0$ mean that the acceleration due to the gravitational potential $\Phi(\vec{r})$ has to be weak to observe any deviation from Newton's law? Or do only the relative accelerations need to be weak? The latter would mean that although the experiment is earthbound and hence is exposed to strong gravitational accelerations compared to a_0 we could measure deviations from Newton's law if we studied small, gravitational accelerations between two bodies that accelerate one another perpendicular to the acceleration field of the earth. Since the experiment described in Chap. 2 is earthbound, it could only measure deviations corresponding to MOND in the latter case. If however absolute accelerations have to be weak, the measurement of that deviations will be beyond our scope and will require an experiment carried out in space.

Chapter 2

The Experiment

In Chap. 2.1 an overview is given on the experiment and on how the measurement is carried out. The subsequent sections 2.2 to 2.8 are dedicated to explain important parts of the experiment in detail.

2.1 Overview

Fig. 2.1 shows a simplified illustration of the experiment. Two spherical concave mirrors are suspended as pendulums, with a pendulum length of about 3 m. Face to face with each other and 24 cm apart, both mirrors form a microwave resonator (see Chap. 2.2.1). Field masses M, placed at the positons A, are moved to the inner positions B. Then the mirror pendulums are exposed to a higher gravitational force due to the decreased distance of the field masses. As a result the mirrors are pulled apart and the length of the resonator increases. This causes a shift of the resonance frequency of the resonator. By measuring the resonance frequency before and after the shift of the field masses (see Chap. 2.5), the frequency shift can be determined. Translating this shift back into a change of the mirror distance (see Chap. 2.2.2), the gravitational law can be tested. After moving the field masses back to position A, the whole procedure of measuring the change of the mirror distance is repeated until enough data are collected in order to be able to test the law of gravitation with the required precision.

Field masses between 1 and 9 kg are used. Such masses cause the mirrors to change their distance by 3 to 10 nm (see Chap. 3). If field masses of 3 kg or lighter are used, the mirror pendulums will be exposed to gravitational accelerations comparable to a_0, such that if MOND was correct a deviation from Newton would be observable.

To reduce disturbances caused by Brownian motion of air particles and variations of air pressure and temperature, the pendulums are placed inside a cryostat that serves as a vacuum vessel. The vacuum system is described in detail in Chap.

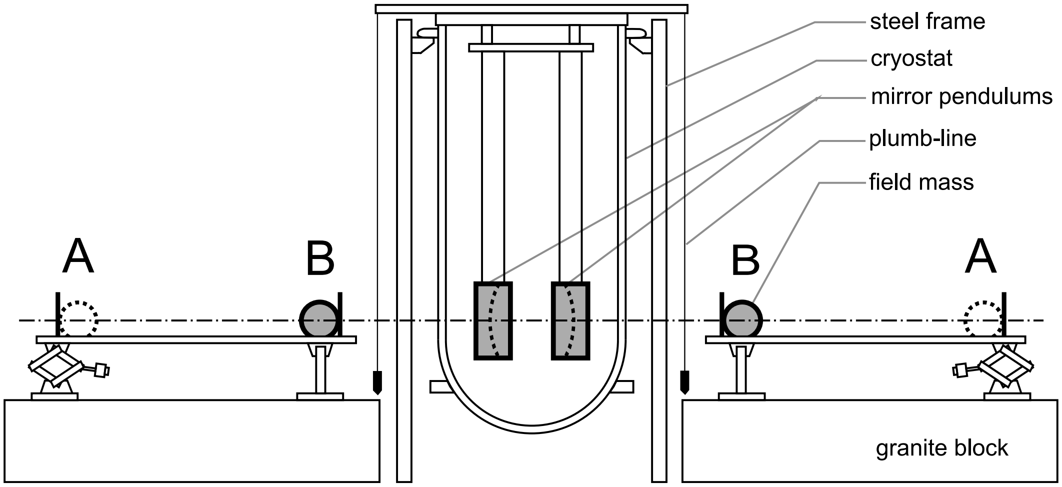

Figure 2.1: Simplified illustration of the experiment: Two mirror pendulums will be pulled apart due to gravitation if field masses on both sides change their position from A to B.

2.8. Furthermore two plumb-lines are suspended from the lid of the cryostat and point onto the granite blocks in order to determine the position of the cryostat relative to the field masses.

Apart from the lighter field masses and the improved measurement electronics, this experiment is similar to the one carried out in Wuppertal until 2002 to measure the gravitational constant G (see [Sch92], [Wal95], [Sch99], [Kle02] and [Kle99]). There, in order to maximize the signal-to-noise ratio, field masses of about 500 kg were used.

2.2 The Resonator

After the detailed description of the resonator in Chap. 2.2.1, it is shown how its resonance modes can be calculated and how a shift of the resonance frequency caused by the repositioning of the field masses can be translated back into the change of the mirror distance (see Chap. 2.2.2). The final part, Chap. 2.2.3, is dedicated to the sensitivity of the resonator in respect of seismically induced excitation.

2.2.1 Detailed Description

Fig. 2.2 shows an illustration of the resonator. The resonator consists of two spherical concave mirrors. Each mirror is made of copper, has a curvature radius of 58 cm and has an aluminum coating. The mass of one mirror is about 3.8 kg. The center of mass is at the center of the concave surface. Each mirror is

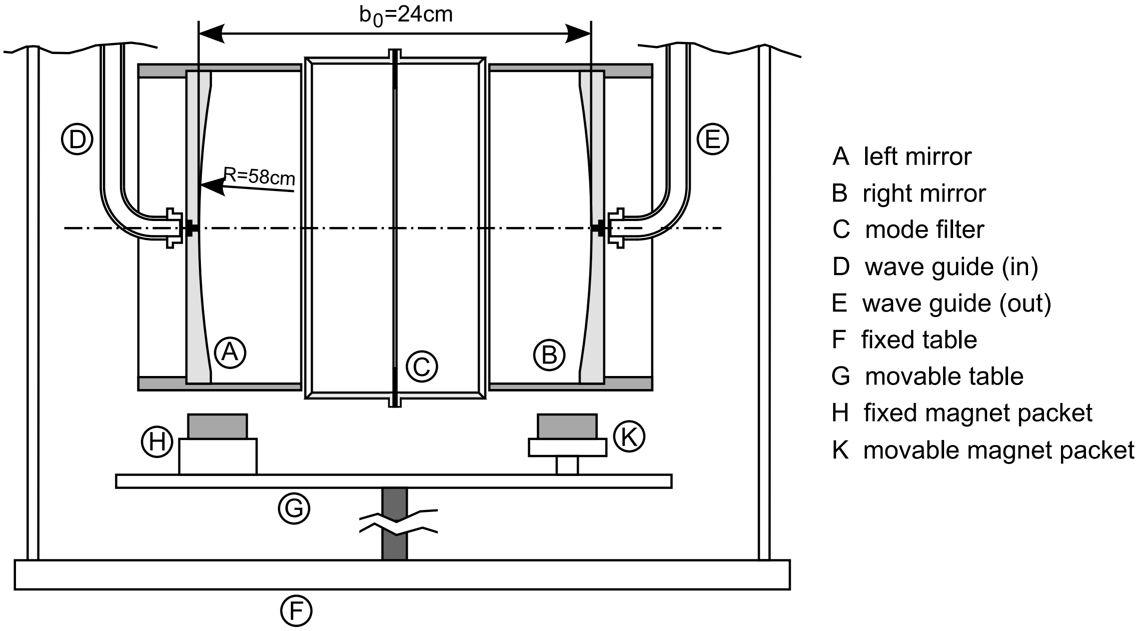

Figure 2.2: Simplified illustration of the two mirror pendulums that form a microwave resonator. Between the mirrors a mode filter is suspended as a pendulum in order to suppress high order transversal modes and to close the resonator. Magnet packets are mounted on a table under the mirrors in order to damp their oscillations.

suspended by two tungsten wire straps[1] that are fixed at a plate mounted under the lid of the cryostat, such that the pendulum length is about 2.7 m. The plate is made of zerodur, a material with a low thermal expansion coefficient. Due to that kind of suspension the distance of the mirrors is insensitive to small tilts of the frame caused by microseismics or temperature-induced deformations of the frame (see [Kle02]). A microwave, generated with an HP 8340b frequency generator, is fed into the resonator via a wave guide on the left side of the resonator. The wave passes the left mirror through an axial hole that is filled with a dielectricum. Behind the right mirror a wave guide catches the part of the wave that leaves the resonator through the axial hole of the right mirror. A diode[2] transforms the power of this transmitted wave into a DC voltage proportional to that power. This signal is detected. Dependent on the distance of the mirrors, standing waves occur between the mirrors at specific frequencies, i.e. resonances emerge. In that case the power of the transmitted wave and therefore the measured DC voltage becomes maximal. Two other diodes are installed to measure the power of the ingoing wave as well as the wave that is reflected from the left mirror.

To optimize the coupling between the wave guides and the resonator, the wave guides can be adjusted using stepper motors. To minimize the electromagnetic

---

[1] diameter of the wires $\approx 200\mu$m

[2] Millitech DXP-42

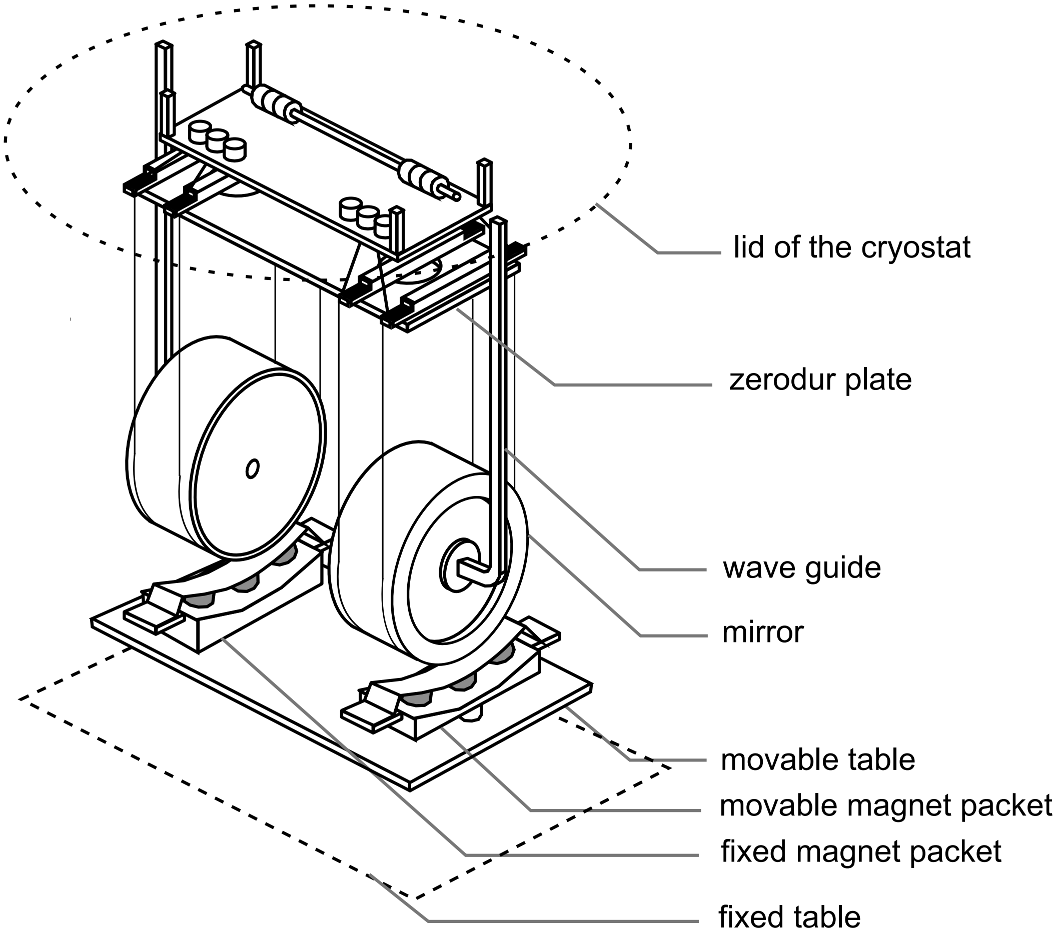

Figure 2.3: Simplified illustration of the two mirror pendulums that form a microwave resonator. They are suspended under the lid of the cryostat. The mode filter, which closes the resonator, is not shown. The movable table with the magnet packets is connected with a table that is attached to the lid. This attachment is not shown.

loss in case of a resonance, the resonator is closed with a hollow cylinder that also serves as a mode filter and is not mechanically connected with the mirrors. A more detailed descripton of the resonator, especially of the coupling mechanism, can be found in [Kle02], [Sch99] and [Wal95]. The microwave circuit is explained in detail in [Sch08] and [Kle02].

2.2.2 Mode Spectrum and Resonator Geometry

Assuming b as the distance between the centers of mass of both mirrors, according to [Kle02] the length of the resonator is also given by b. With R as the curvature radius of the mirrors, the possible resonance frequencies can be calculated by

$$f_R = \frac{c}{2b}\left[q + \frac{n}{\pi}\arccos(1 - b/R) + N^{(\pm)}\frac{c}{8\pi^2\, R\, f_R} + \mathcal{O}\left((k\Omega)^{-6}\right)\right] \tag{2.1}$$

with c as the speed of light in vacuum, k the wave number of the microwave and Ω the beam waist of the resonance mode given by

$$\Omega = \sqrt{\frac{b}{k}} \cdot \left(\frac{2R}{b} - 1\right)^{1/4} \tag{2.2}$$

Furthermore it is

$$\begin{aligned} n &= 2p + m + 1 \\ N^{(\pm)} &= 2p^2 + 2pm - m^2 + 2p - 2 + m \pm 4m \end{aligned} \tag{2.3}$$

with p, m and q as the number of the radial, azimutal and axial knots of the resonance mode. As Eq. (2.1) shows, a change in the distance $b + \Delta b$ of the mirrors causes a change of $f_R + \Delta f_R$. If, like in our case, $\Delta b \ll b$ a Taylor expansion of (2.1) leads to

$$\Delta b = \beta \cdot \Delta f_R \tag{2.4}$$

with

$$\beta = -\frac{b}{f_R}\left(1 - \frac{n\, c}{2\pi\, f_R}\sqrt{\frac{1}{2\, R\, b - b^2}} + \mathcal{O}\left((k\Omega)^{-6}\right)\right)^{-1} \tag{2.5}$$

where $\beta \approx -10$ nm/kHz, dependent on the mode that is used. Both b and R can be calculated if the pattern of resonance modes of the resonator is known, i.e. if the resonance frequencies are measured and the knot parameters p, m, q and $N^{(\pm)}$ are assigned to each of these frequencies. Such a method is explained in [Sch92] and [Kle02]. In [Sch08], the software HEXENWERK was written in order to assign the knot parameters automatically. As a cross check the curvature radius R of both mirrors can be measured independently. A method that allows to calculate b without the knowledge of the knot parameters is presented in Chap. 7.2.

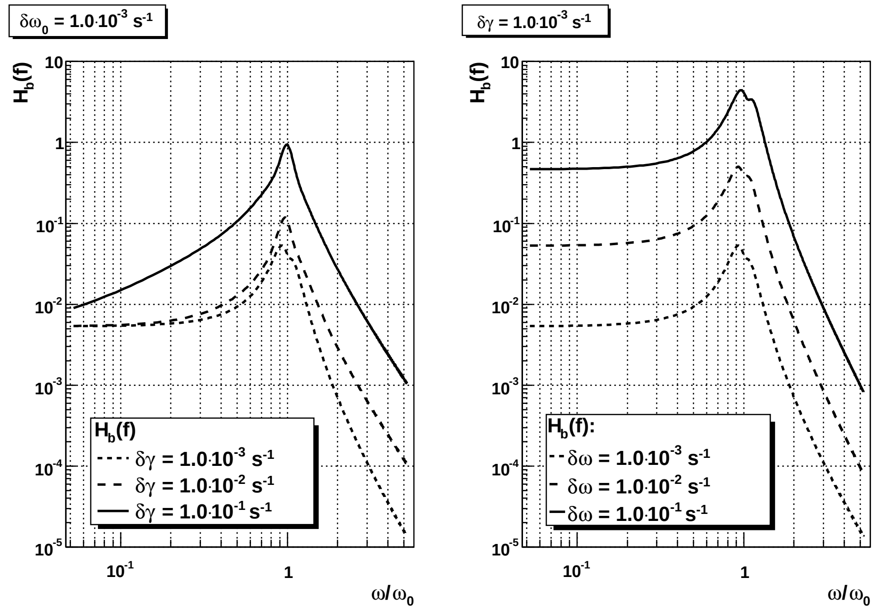

Figure 2.4: Transition function $H_b(\omega)$, plotted against the ratio ω/ω_0: **left:** with $\delta\omega_0 = 1\cdot10^{-3}\mathrm{s}^{-1}$ and the difference $\delta\gamma$ of the damping constants of both pendulums as a parameter, **right:** with $\delta\gamma = 1\cdot10^{-3}\mathrm{s}^{-1}$ and the difference $\delta\omega_0$ of the natural frequencies of both pendulums as a parameter.

2.2.3 Transition Characteristics

Both mirrors are suspended as pendulums because that makes the mirror distance, b, insensitive to seismically induced motion of the frame. To study this effect in detail, it is assumed that a mirror pendulum is excited by an external periodic force of frequency ω and amplitude $S_{\text{ext}}(\omega)$.

The equation of the i-th mirror pendulum excited by an external periodic force will be given by

$$\frac{1}{\omega_{0_i}^2}\,\ddot{\varphi}_i + \frac{2\gamma_i}{\omega_{0_i}^2}\,\dot{\varphi}_i + \varphi_i = S_{\text{ext}}(\omega)e^{i\omega t} \tag{2.6}$$

with ω_{0_i} as the natural frequency of that pendulum and γ_i as its damping constant. Due to that excitation the mirror distance b oscillates with the amplitude $S_b(\omega)$. The transition function is then given by

$$H_b(\omega) = \frac{S_b(\omega)}{S_{\text{ext}}(\omega)} = \frac{g}{\omega_{0_1}^2}\,H_1(\omega)\,e^{i\phi_1(\omega)} - \frac{g}{\omega_{0_2}^2}\,H_2(\omega)\,e^{i\phi_2(\omega)} \tag{2.7}$$

with $g = 9.81$ m/s^2 and

$$H_i(\omega) \;=\; \frac{\varphi_i(\omega)}{S_{\mathrm{ext}}(\omega)} = \frac{\omega_{0_i}^2}{\sqrt{(\omega^2 - \omega_{0_i}^2)^2 + (\omega\gamma_i)^2}} \tag{2.8}$$

$$\phi_i(\omega) \;=\; \arctan\left(\frac{2\,\gamma_i\,\omega}{\omega^2 - \omega_{0_i}^2}\right) \tag{2.9}$$

The transition function (2.7), plotted in Fig. 2.4, shows that the two mirrors form a bandpass filter. Fig. 2.4 shows that seismics are the better suppressed the higher the synchronicity of the mirror pendulums is. If $\omega_{0_1} = \omega_{0_2}$ and $\gamma_1 = \gamma_2$, seismic excitations of the frame would not be transfered to the mirror distance, b, at all.

As shown in [Sch08] and [Gos04], the transition characteristics are also modified due to the finite deflection of the mirror pendulums, the nonvanishing anelasticity of the pendulum wires and the additional damping of the pendulums that follows from these effects. Compared to the effects mentioned above, this is neglegible, especially if the accuracy of our measurement is taken into account.

2.3 The Magnetic Brakes

The sensitivity of the mirror distance, b, to seismic excitations can be minimized using adjustable magnetic brakes. With these brakes the damping constant of both mirror pendulums can be adjusted separately to synchronize their oscillations.

The magnetic brake consists of two magnet packets mounted on a table that can be moved up and down, relative to the mirrors (see Fig. 2.2 and 2.3). The table sits inside a frame that is attached to the lid of the cryostat from below, such that the table hangs under the mirrors and is not mechanically connected with them, except via the lid (see [Sch92], [Wal95], [Sch99] and [Kle02]). The left magnet packet is fixed on that table. The right packet can be additionally moved relatively to the left packet, in order to adjust the damping of the mirror pendulums separately. Both the table and the right packet are moved via stepper motors controlled by the software FULLTHROTTLE. Since the position of the magnet packets cannot be reproducibly measured via the internal counters of the stepper motors, two slide resistances are installed to measure the positions of both magnet packets relative to the mirrors. One resistance records the position of the table relative to the mirrors. The other one records the position of the movable magnet packet relative to the table.

These brakes can only damp oscillations of the mirrors relative to the table at which the magnet packets are mounted. Since the table can be also treated as a pendulum, which is excited to oscillate due to seismics, the transition function

material	no.	weight [kg]	diameter [mm]
plastic	1	$1,001$	$127,136$
	2	$1,001$	$127,133$
granite	1	$2,926$	$127,136$
	2	$2,917$	$127,133$
marble	1	$2,925$	$127,186$
	2	$2,924$	$127,205$
brass	1	$9,020$	$127,0$
	2	$9,020$	$127,0$

Table 2.1: Material, diameter and weight of the homogeneous spheres that are used as field masses. The uncertainty of the diameter is given by $7\,\mu$m, that of the weight by $0,1$ g.

(2.7) will change to

$$H_b^2(\omega) = \frac{\omega_0^4 + (\omega\gamma)^2 \cdot H_M^2(\omega)}{(\omega^2 - \omega_0^2)^2 + (\omega\gamma)^2} \tag{2.10}$$

with ω_0 the natural frequency of the mirrors, γ the damping due to the brakes and $H_M(\omega)$ the transition function of the brakes. More details about that can be found in [Sch92]. Furthermore the oscillating table excites the attachment at which the mirrors are suspended. Since the natural frequency of the table is much higher than the resonance frequency of the mirrors, this effect can be separated and is therefore negligible.

2.4 The Field Masses

The field masses are solid homogeneous spheres of different material and different mass but with the same diameter (s. Tab. 2.1). On each side of the experiment one sphere is placed on a guide rail that is placed itself on a granite block. As an expample the right hand rail is illustrated in Fig. 2.5. The spheres will move between the positions A and B automatically when the rail moves up or down at its far end C. This movement is done via stepper motors. If the far end of the rails moves up the spheres will roll from the far to the near position. If the rails move down, the spheres will roll back to the far position. This movement needs about 2 minutes. Both at A and B, stoppers determine the position of the spheres. Before and after a measurement, these stoppers can be moved manually to adjust these positions.

Like in the case of the magnetic brakes, the stepper motors of both guide rails are also controlled via FullThrottle. To move the masses automatically during the measurement, the measurement software EagleEye communicates

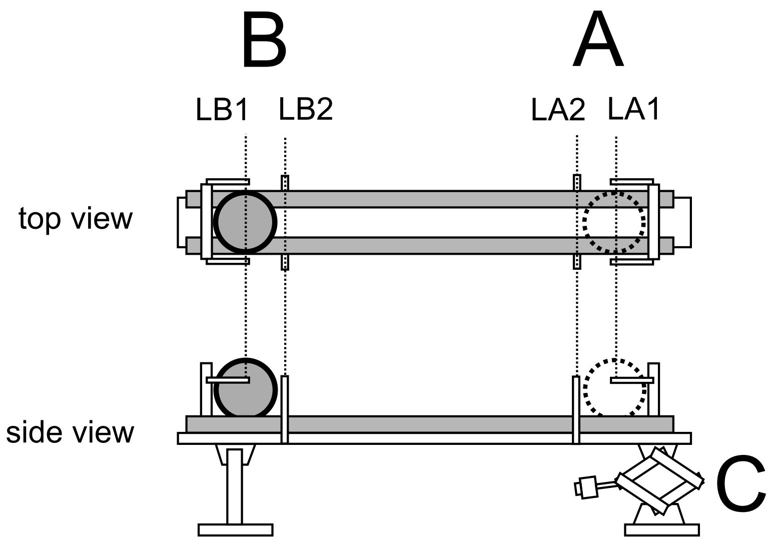

Figure 2.5: Simplified illustration of the right hand guide rail with a sphere placed at the near position B. The far light barriers are indicated as LA1 and LA2, the near ones as LB1 and LB2. At position C a stepper motor can move the guide rail up and down.

with FullThrottle remotely via TCP/IP, such that the spheres change their positions between A and B with a period of 40 minutes. To assure that the spheres are always at a well-defined position, i.e. touch the designated stoppers, light barriers are used: The spheres will be at the positions A if the light barriers LA1 are open whereas LA2 are closed. The same would be true for the positions B and the barriers LB1 and LB2. If an error occures during the movement of the spheres, EagleEye will cancel the measurement and will send the TCP/IP communication report via e-mail to all users that want to be informed about that error.

2.5 Measurement of the Resonance Frequency

To determine the change of the mirror distance, Δb, according to Eq. (2.4) the shift of the resonance frequency, Δf_R, has to be measured. To get Δf_R, the resonance frequency has to be found before and after the shifting of the field masses. Finding the resonance frequency of the cavity is done in the following way: If a resonance is at f_R and if a microwave with frequency f around f_R is fed into the cavity and the transmitted power is detected using a DC voltage diode, one will measure the voltage

$$U(f) = U_{\max} \cdot \left[1 + 4 \left(\frac{f - f_R}{f_{1/2}} \right)^2 \right]^{-1} \tag{2.11}$$

if $U_{\max}$ is the maximal amplitude of the resonance and $f_{1/2}$ its width. The maximal amplitude depends on the power of the wave that is fed into the resonator. It also depends on the coupling. Due to the setup the coupling is maximal for axial modes, i.e. modes with $p = m = 0$. The ratio $U_{\max}/f_{1/2}$, as well as how the shape of the measured resonance resembles the profile Eq. (2.11), depends on the quality of the cavity. The quality is the higher the lower the energy loss is within the resonator. More details about quality issues can be read in [Sch92] or [Kle02].

To measure f_R, first of all a resonance frequency f_R^* is guessed. Symmetrically around f_R^* an interval $[f_l, f_h]$ is choosen such that its width $f_h - f_l$ is of the order of the guessed width $f_{1/2}^*$ of the resonance and that f_R can be found within $[f_l, f_h]$. Beside f_R, other resonance modes must not be within this interval. To guarantee this, a membrane is fixed inside the mode filter that is suspended between the mirrors. This suppresses the resonance modes of high transversal order. To find the real resonance frequency f_R, a number of equidistant frequencies $f_k (k \in \mathbb{N})$ within $[f_l, f_h]$ are generated by the frequency generator. For each f_k the amplitude U_k of the transmitted wave is measured with the diode. Then the values (f_k, U_k) are fitted to the resonance profile (2.11) to get the parameters of the resonance f_R, $f_{1/2}$ and $U_{\max}$. Using the χ^2 of this fit, one can check, if Eq. (2.11) is adequate to describe the resonance. If this is not the case, the deviation of the resonance from Eq. (2.11) has to be determined and the fit results have to be corrected. In Chap. 6.4 it is explained how this can be done.

In an iteration, the estimated resonance frequency f_R^* and the estimated width $f_{1/2}^*$, the fitted parameters of the previous fit are used. For the first measurement, f_R^* is read from the generator. Thus before the measurement starts, the resonance mode has to be found manually via an oscilloscope. The width, $f_{1/2}^*$, of that resonance can also be guessed using the oscilloscope.

Such a resonance measurement, i.e. the sweep and the subsequent fit, is automatically done by the software EagleEye which also writes the measured data to disk. The measurement period can be arbitrarily chosen by the user, but has to be at least 0.5 s due to hardware constraints.

2.6 Environmental Measurements

Since the mirror distance is measured with high precision, all external influences that spoil the signal are measured with high precision as well. To extract the signal from the background caused by these influences, one has to understand how these influences affect the signal. Therefore a number of environmental parameters are recorded during the measurement.

First of all the temperature is measured at six different positions using 4-wire RTD circuits: three sensors are placed at the three supporting points where the vacuum containter is fixed within the steel frame. One sensor is placed within the

Channel No.	Measured Quantity
105	temperature inside the DVM that measures the amplitude of the resonance
106	temperature inside the DVM that is connected to the environment channels
107	auxiliary channel, temperature lid
108	temperature hall
109	temperature tent
110	ambient pressure
111	tilt lid, along the axis
112	tilt lid, perpendicular to the axis
113	tilt frame, along the axis
114	tilt frame, perpendicular to the axis
115	temperature north
116	temperature south
117	temperature west
118	voltage, pre vacuum
119	voltage, high vacuum

Table 2.2: Assignment of environment channels that are connected to the KE2701 with the Model 7700 switch channel module.

temperature-insulated tent that encloses the whole experiment. Another sensor measures the temperature of the hall wherein the tent is placed. Furthermore a sensor measures the temperature of the DVM that is connected with the DC voltage diode that measures the power of the microwave transmitted through the resonator. Finally a sensor measures the temperature inside the DVM that is connected to the environment sensors described in this chapter. Inside the tent, also the air pressure is measured.

Additionally the tilt is measured on the lid and on the steel frame, in each case both along and perpendicular to the symmetry axis of the resonator. As tilt sensors, single axis electrolytic sensors of type Spectron RG-33T are used. Temperature, air pressure and tilt sensors are connected with a multi-channel DVM of type Keithley KE2701 extended with a Model 7700 switch channel module. The detailed assignment of that channels can be found in Tab. 2.2. The measurement is conducted by the software Envy, that has been written in LabVIEW. Finally the seismic motion is measured with a Güralp CMG-T30-0038 broadband seismometer. This data acquisition is done with a separate PC.

2.7 GPS Synchronization

According to [Sch92], the frequency of the microwave that is generated by the HP8340b has an accuracy of 4 Hz. Furthermore the frequency drifts slowly due to deterioration of the internal quartz oscillator. To improve the longterm stability of the generated frequency, a GPS receiver is connected to the HP8340b in order to be used as an external reference clock. As a reference signal it generates a periodic rectangular 10 MHz signal that is fed into the HP8340b.

2.8 The Vacuum System

The mirror pendulums are placed in an evacuated cryostat to avoid noise from thermal and convection effects of the surrounding air. According to [Sch92] a pressure of 10^{-5} mbar is required inside the cryostat.

To obtain this vacuum, first of all a rotary vane pump is used to reach a prevacuum of 10^{-2} mbar. A turbomolecular pump reduces this vacuum to 10^{-5} mbar. To keep that vacuum during the measurement, both vacuum pumps run all the time. Since they are connected to the lid of the cryostat via flexible tubes, the transmission of their vibrations to the mirror pendulums is suppressed as long as the frame is adjusted properly. A noise measurement that was done after switching off the vacuum pumps showed no difference between that measurement and a measurement with running pumps. Thus the vacuum pumps do not increase the displacement noise of the mirror distance.

Both the prevacuum and the high-vacuum are measured. To get the pressure of the prevacuum a thermal conductivity vacuum gauge is used, and a Penning gas discharge tube measures the pressure of the high-vacuum.

Chapter 3

Calculation of the expected Signal

This chapter is dedicated to the calculation of the change of the mirror distance, Δb, that is caused by the shifting of the field masses described in Chap. 2.1. This calculation is done both for Newton's law and for MOND with the interpolation functions proposed in 1.2.

3.1 Calculation of the expected Distance Shift

First of all the gravitational force to which a mirror is exposed due to one sphere is computed. To do this, the sphere that serves as the field mass is assumed to have volume V and mass density $\rho(\vec{r})$ and that it is placed at the center of the coordinate system. According to the field equation (1.2) of MOND and $\vec{a}(\vec{r}) = -\vec{\nabla}\Phi(\vec{r})$, the sphere is the source of an acceleration field $\vec{a}(\vec{r})$ given by

$$\vec{\nabla} \cdot \left[\mu\left(|\vec{a}(\vec{r})|/a_0\right)\, \vec{a}(\vec{r})\right] = 4\pi G \cdot \rho(\vec{r}) \tag{3.1}$$

Since the mass density of the field masses, $\rho(\vec{r})$, is approximately spherically symmetric, the integration of Eq. (3.1) yields

$$\int_S \mu\left(|\vec{a}(\vec{r})|/a_0\right)\, \vec{a}(\vec{r})\, d\vec{S} = 4\pi G \cdot M \tag{3.2}$$

The interpolation function $\mu(|\vec{a}'(\vec{r})|/a_0)$ modifies the acceleration according to the Newtionan case only by rescaling it without changing its direction. Therefore the integral of Eq. (3.2) can be solved like in the Newtonian case. This results in

$$\mu(a(r)/a_0)\, a(r) \; = a_N(r), \qquad a_N(r) = G\,\frac{M}{r^2} \tag{3.3}$$

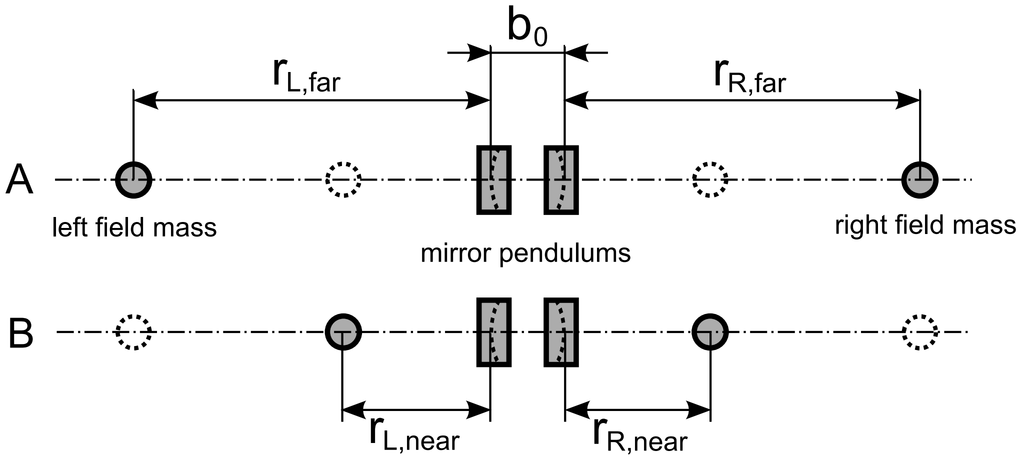

Figure 3.1: Schematic illustration of repositioning the field masses from the far position A to the near position B. Compare in this context the description provided in Chap. 2.1 and Fig. 2.1.

with a_N the acceleration according to Newton's law of gravitation. Eq. (3.3) has to be solved for $a(r)$ dependent on the interpolation function. The procedure of calculating $a(r)$ is explained in Chap. 3.2. Having calculated $a(r)$, the acceleration field $\vec{a}(\vec{r})$ due to the sphere is given by

$$\vec{a}(\vec{r}) = -a(r)\,\frac{\vec{r}}{r} \tag{3.4}$$

After that it is assumed that a mirror with volume V_{mirr} and mass distribution $\rho_{\text{mirr}}(\vec{r})$ is placed within this acceleration field with its center of mass given by $\vec{r}_{\text{CM}}$. Then the force on the mirror due to the sphere can be calculated by

$$\vec{F}(\vec{r}_{\text{CM}}) = \int_{V_{\text{mirr}}(\vec{r}_{\text{CM}})} \rho_{\text{mirr}}(\vec{r},\vec{r}_{\text{CM}})\,\vec{a}(\vec{r})\,d^3\vec{r} \tag{3.5}$$

In case of the experiment, the mirror is a pendulum with natural frequency ω_0. Then the force $\vec{F}(\vec{r}_{\text{CM}})$ causes a deflection $\Delta\vec{b}$ of the pendulum of

$$\Delta\vec{b} = \frac{\vec{a}_{\text{res}}(\vec{r}_{\text{CM}})}{\omega_0^2}, \qquad \vec{a}_{\text{res}} = \frac{\vec{F}(\vec{r}_{\text{CM}})}{M_{\text{mirr}}} \tag{3.6}$$

with M_{mirr} as the mass of the mirror. Finally one has to calculate the change of the mirror distance, Δb, caused by moving the field masses from the far to the near positions, as described in Chap. 2.1 and illustrated in Fig. 3.1. Moving the field masses that way causes a change of the mirror distance along the symmetry axis of the resonator given by

$$\Delta b = \frac{1}{\omega_0^2} \sum_{i \in \{L,R\}} \big(a_{\text{res}}(r_{i,\text{near}}) - a_{\text{res}}(r_{i,\text{near}} + b_0) - a_{\text{res}}(r_{i,\text{far}}) + a_{\text{res}}(r_{i,\text{far}} + b_0)\big) \quad (3.7)$$

with $a_{\text{res}}(r)$ as the projection of $\vec{a}_{\text{res}}(r)$ onto the symmetry axis. In the case of a symmetric movement of the spheres one has

$$\begin{aligned} r_{L,\text{near}} &= r_{R,\text{near}} = r_{\text{near}} \\ r_{L,\text{far}} &= r_{R,\text{far}} = r_{\text{far}} \end{aligned}$$

and Eq. (3.7) simplifies to

$$\Delta b = \frac{2}{\omega_0^2} \big(a_{\text{res}}(r_{\text{near}}) - a_{\text{res}}(r_{\text{near}} + b_0) - a_{\text{res}}(r_{\text{far}}) + a_{\text{res}}(r_{\text{far}} + b_0)\big) \quad (3.8)$$

The expected results, i.e. the change of the mirror distance, Δb, depending on the position and the mass of the field masses, are discussed in detail in Chap. 3.3.

3.2 Calculation of modified Accelerations

If both the acceleration $a_N = GM/r^2$ according to Newton's law and the interpolation function $\mu(x)$ are given, the modified acceleration $a(r)$ can be calculated by solving Eq. (3.3) for $a(r)$.

In the case of the interpolation functions (1.6), (1.7), (1.8) and (1.10) the accelerations $a(r)$ can be calculated by solving analytically Eq. (3.3) for $a(r)$. With a_0 as the threshold acceleration due to MOND, the interpolation function (1.6) leads to

$$a(r) = a_N \cdot \sqrt{\frac{1}{2} + \frac{1}{2} \cdot \sqrt{1 + \left(\frac{2a_0}{a_N}\right)^2}} \quad (3.9)$$

where (1.7) results in

$$a(r) = \frac{a_N}{2} + \sqrt{\left(\frac{a_N}{2}\right)^2 + a_N a_0} \quad (3.10)$$

The function (1.12) respectively (1.8) are associated with

$$a(r) = a_N + \sqrt{a_N a_0} \quad (3.11)$$

According to [Men10], the interpolation function (1.10) is associated with

$$a(r) = a_0 y \, \frac{1-y^4}{1-y^3} = a_0 y \, \frac{1+y+y^2+y^3}{1+y+y^2}, \qquad y = \sqrt{a_N/a_0} \tag{3.12}$$

In the case of (1.9), the modified acceleration $a(r)$ as well as the interpolation function $\mu(x)$ itself have be to calculated numerically. Since the integrand of (1.9) becomes singular at $x = 0$, QAGS[1] is used as an algorithm which should be able to cope with such singularities. However by virtue of all these complications, it has to be verified that $\mu(x)$ is integrated correctly. That can be done by comparing the analytical calculation of $\mu(x)$ with its numerical counterpart at the level of the first derivatives: Rearranging Eq. (1.9) leads to

$$\mu(x) \, \frac{\pi^2}{6x} = \int_0^{\frac{\pi^2}{6x}} \frac{z}{e^z - 1} \, dz \tag{3.13}$$

Differentiating both sides of Eq. (3.13) gives

$$\frac{d}{dx}\left(\mu(x) \, \frac{\pi^2}{6x}\right) = \frac{\pi^4}{36x^3} \cdot \frac{1}{1 - e^{\frac{\pi^2}{6x}}} \tag{3.14}$$

Since $\mu(x)$ can only be integrated numerically, the left hand side of Eq. (3.14) has to be differentiated numerically as well. Both sides of Eq. (3.14) are equal for all x. Thus the numerical integration of $\mu(x)$, given by (1.9), can be trusted and the associated calculation of the modified acceleration $a(r)$ gives reasonable results.

3.3 Discussion of the expected Results

Fig. 3.2 shows the change, Δb_N, of the mirror distance that will be expected in the case of Newton's law if the spheres are symmetrically moved from the far to the near positions. It is plotted against the distance between a mirror and its adjacent sphere at the near position. To associate this with Fig. 3.1, Δb_N is plotted against r_{near}. This dependency is shown separately for field masses of 1, 3 and 9 kg. The distance between a mirror and its adjacent sphere at the far position is always assumed to be $r_{\text{far}} = 250$ cm. It can be seen that in the case of Newton's law, $\Delta b_N \propto M$ is valid with M the mass of the spheres.

Fig. 3.3, 3.4 and 3.5 show the expected deviation $\Delta b - \Delta b_N$ from Newton's law in case of MOND with the interpolation functions $\mu(x)$ presented in Chap. 1.2. Like in Fig. 3.2, the deviation is plotted against r_{near} and is separately

---

[1] An algorithm that numerically integrates functions with singularities using adaptive quadrature, implemented e.g. in GNU Scientific Library (GSL)

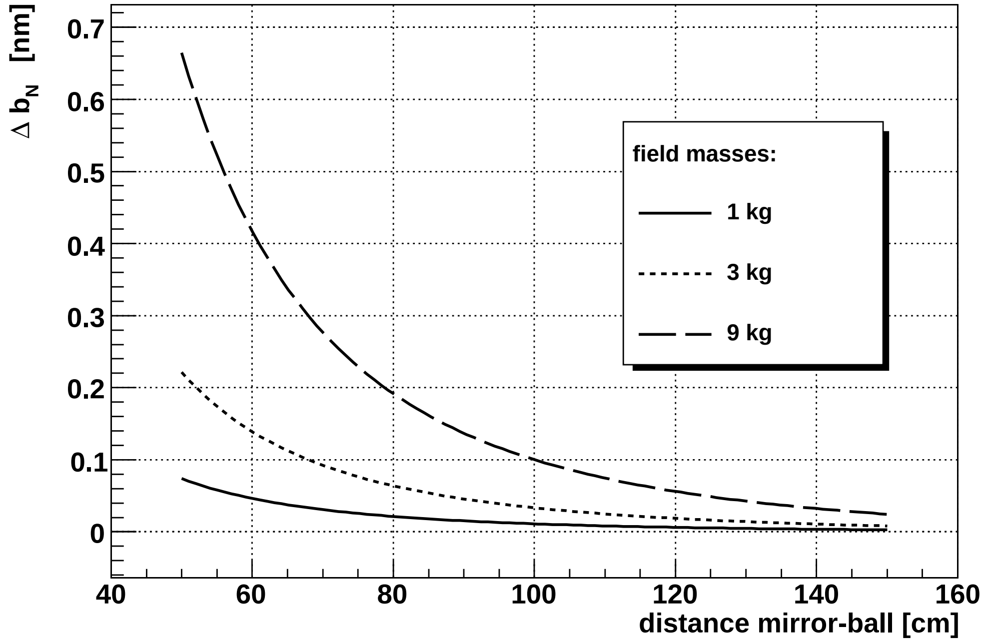

Figure 3.2: Expected change, Δb_N, of the mirror distance in the case of Newton's law if the spheres that are symmetrically moved from far to near positions. It is plotted against the distance, r_{near}, between a mirror and its adjacent sphere at the near position. The distance of the far position is assumed to be 250 cm. These plots are separately shown for spheres of 1, 3 and 9 kg.

shown for the field masses 1, 3 and 9 kg. The 1 kg spheres cause the largest deviation, $\Delta b - \Delta b_N$, from Newton's law since they are the source of the weakest acceleration field. The deviation will increase if r_{near} decreases. Thus the nearest possible r_{near} has to be chosen to measure the largest deviation. Due to the setup of the experiment, the nearest possible distance is given by $r_{\text{near}} = 77$ cm.

According to Fig. 3.2, the symmetric movement of the 1 kg spheres from 250 cm to 77 cm causes a change of the mirror distance of $\Delta b_N \approx 0.02$ nm. The relative deviation in the case of MOND would then be between $+20\%$ and -10%, dependent on the interpolation function. Thus, if MOND was realized in nature, a measurement could distinguish between different interpolation functions. The smallest deviation from Newton's law would be expected in case of the interpolation function (1.9). Unlike in the case of Newton's law, the relation $\Delta b \propto M$ is not valid for MOND.

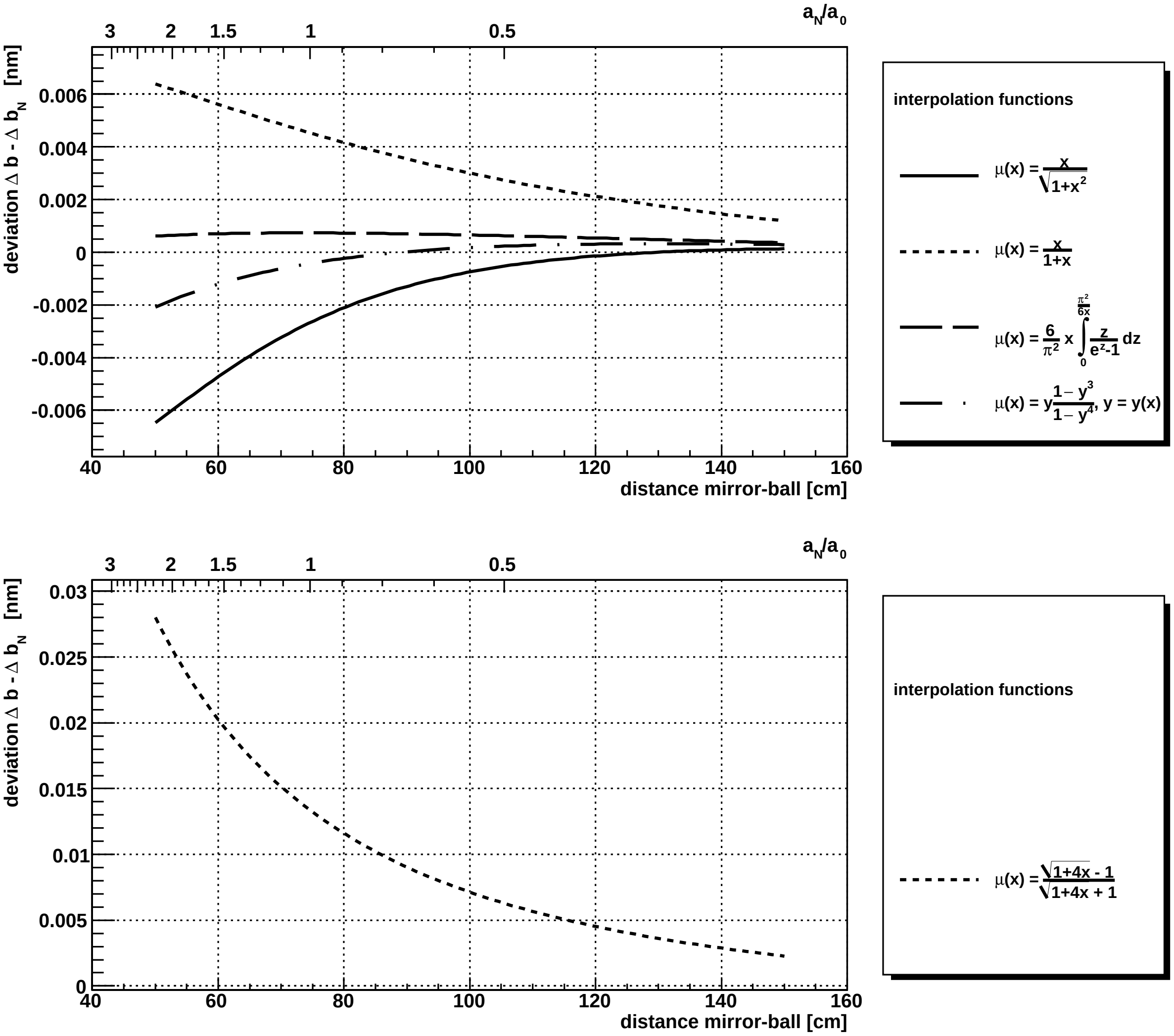

Figure 3.3: Expected deviation $\Delta b - \Delta b_N$ from Newton's law in the case of MOND and 1 kg field masses, dependent on the interpolation function $\mu(x)$. As in Fig. 3.2, the deviation is plotted against the near position of the spheres, r_{near}. The upper axis shows a_N/a_0 with a_N the acceleration of a mirror due to a sphere at r_{near} according to Newton's law.

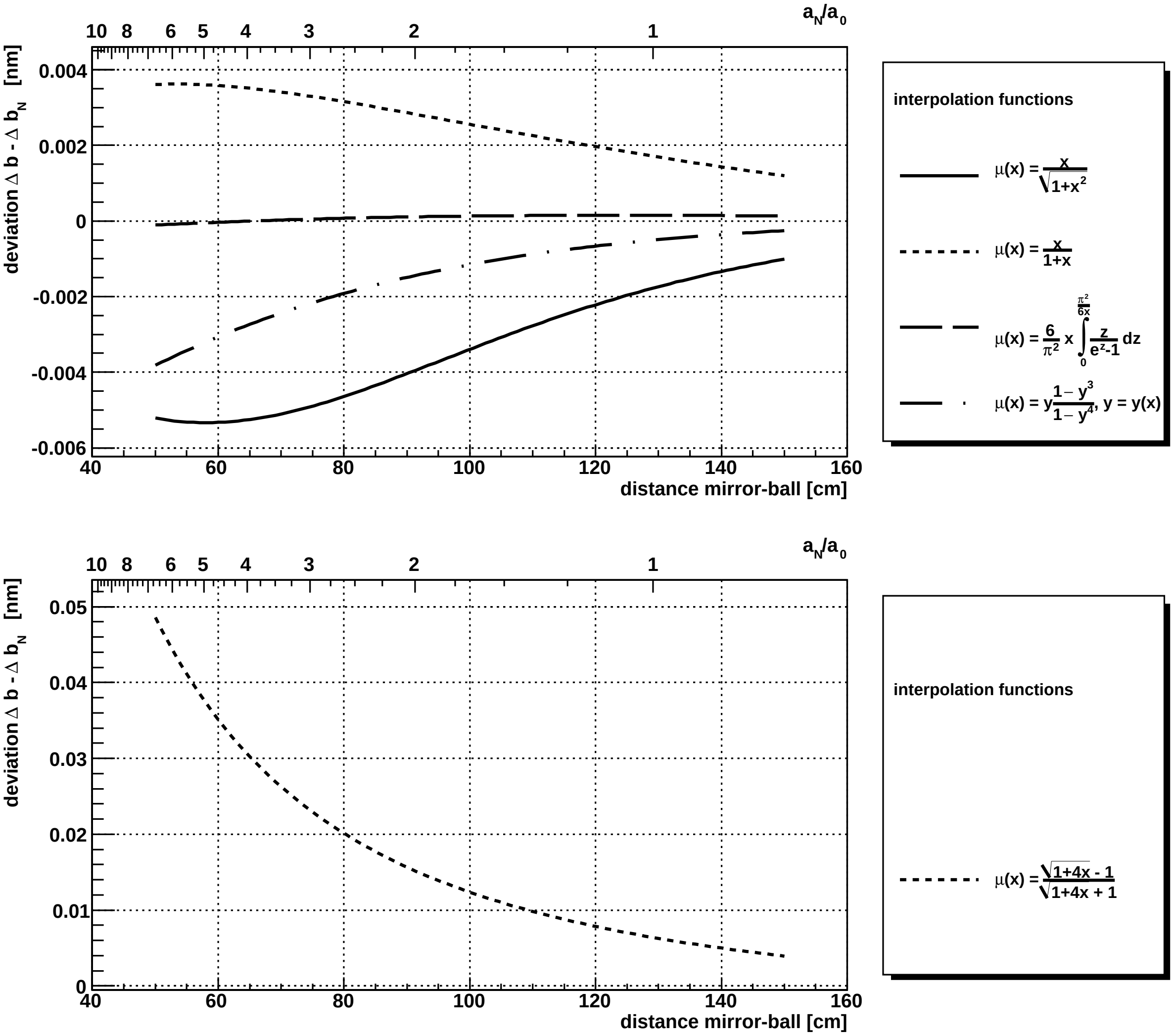

Figure 3.4: Expected deviation $\Delta b - \Delta b_N$ from Newton's law in the case of MOND and 3 kg field masses, dependent on the interpolation function $\mu(x)$. As in Fig. 3.2, the deviation is plotted against the near position of the spheres, r_{near}. The upper axis shows a_N/a_0 with a_N the associated acceleration of one mirror according to Newton's law due to a sphere at r_{near}.

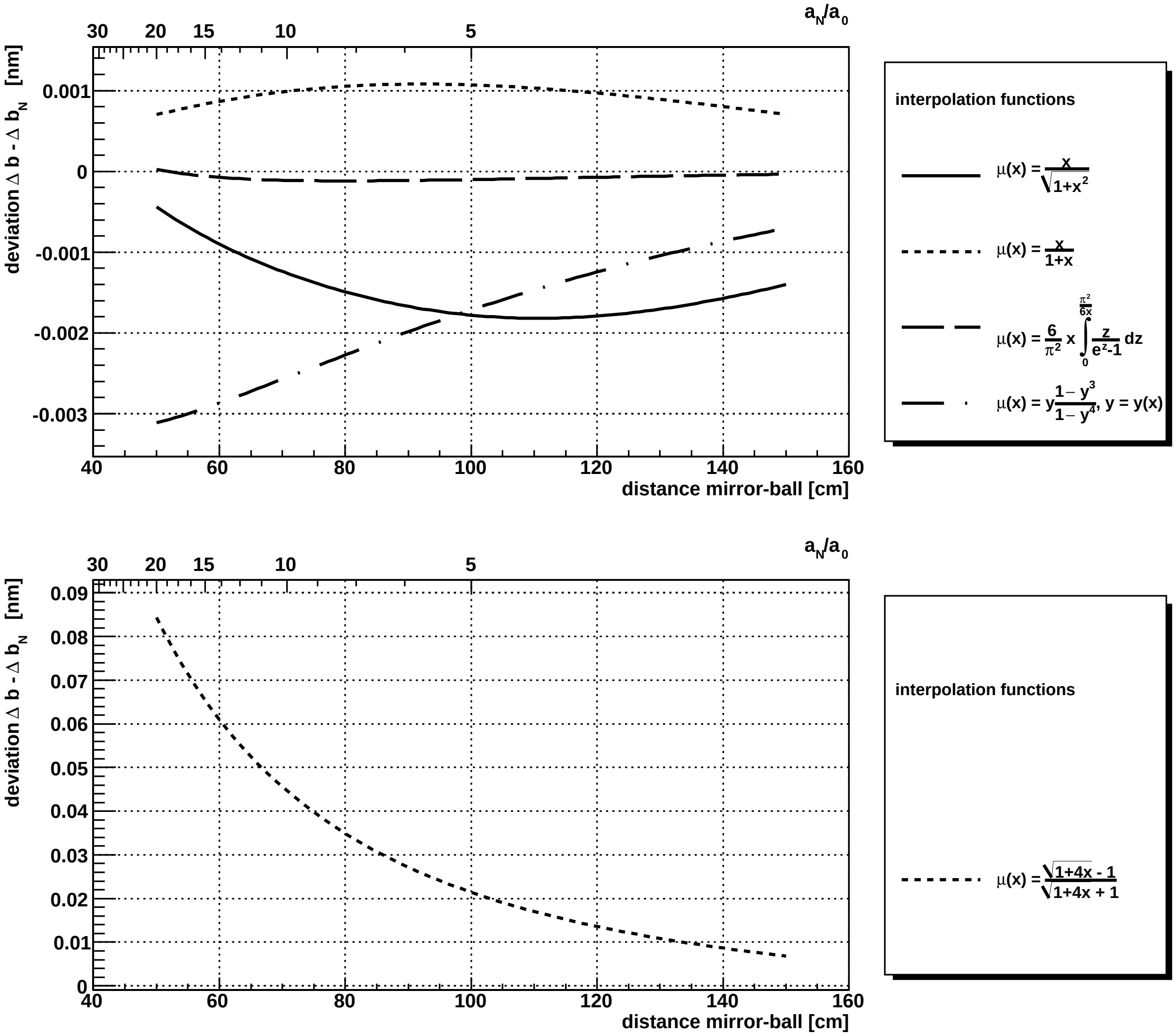

Figure 3.5: Expected deviation $\Delta b - \Delta b_N$ from Newton's law in the case of MOND and 9 kg field masses, dependent on the interpolation function $\mu(x)$. As in Fig. 3.2, the deviation is plotted against the near position of the spheres, r_{near}. The upper axis shows a_N/a_0 with a_N the acceleration of a mirror due to a sphere at r_{near} according to Newton's law.

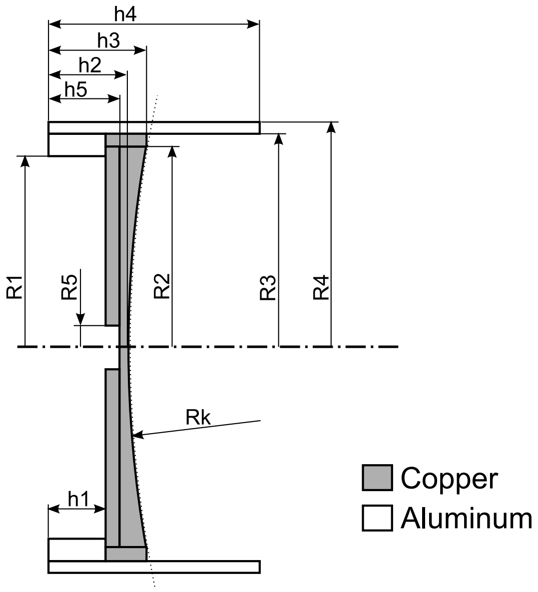

Figure 3.6: Decomposition of a mirror into cylinders, with $\rho_{\mathrm{Cu}} = 8.92$ g/cm^3 and $\rho_{\mathrm{Al}} = 2.7$ g/cm^3. The corresponding measurements can be found in Tab. 3.1.

3.4 Corrections due to the Mirror Geometry

According to Fig. 2.2, the mirrors are far from being point masses. This section is dedicated to the correction which has to be taken into account when calculating the change, Δb, of the mirror distance. If this effect was neglegible, the force between a mirror and a sphere could be calculated according to

$$\vec{F}(\vec{r}_{\mathrm{CM}}) = M_{\mathrm{mirr}} \cdot \vec{a}(\vec{r}_{\mathrm{CM}}) \tag{3.15}$$

instead of using the integral (3.5) that has to be calculated numerically. To get the correct answer, the expected result Δb has to be calculated using both (3.15) and (3.5). According to Fig. 3.6, each mirror can be seen as a composition of different sized cylinders that are made of different materials, i.e. copper and aluminum, but with constant mass density. Thus Eq. (3.5) can be simplified, and the force between a mirror and a sphere can be written as

$$\vec{F}(\vec{r}_{\mathrm{CM}}) = \sum_i \rho_i \int_{V_i(\vec{r}_{\mathrm{CM}})} \vec{a}(\vec{r})\, d^3\vec{r} \tag{3.16}$$

where V_i is the volume of the i-th cylinder with ρ_i as its constant mass density and $\vec{a}(\vec{r})$ is the acceleration field (3.4) due to one sphere.

The integration of the gravitational force has been done numerically in case of Newton and MOND with the interpolation functions presented in Chap. 1.2. To provide the functionality of integrating over the mirrors, an object oriented

	left mirror	right mirror
R1	9.29	9.29
R2	9.4	9.38
R3	9.6	9.6
R4	9.9	9.9
R5	0.37	0.37
Rk	57.99	57.99
h1	3.03	3.05
h2	3.88	3.91
h3	4.65	4.68
h4	10.0	10.0
h5	3.43	3.42

Table 3.1: Measurements of both mirrors in cm according to Fig. 3.6. All quantities have been measured with an accuracy of 10 μm.

geometry integration framework has been written in C++. This framework allows to integrate the gravitational force between 3-dimensional bodies that have been created with the geometry package of ROOT.[2] Furthermore the mass, the center of mass and the moment of inertia of these bodies can be integrated. In the case of the moment of inertia, the rotation axis can be arbitrarily chosen. As the integration algorithm a Monte Carlo algorithm has been imported from the GNU Scientific Library (GSL) but has been adapted such that it can integrate vector valued densities. Furthermore an interface exists that enables the user to provide more sophisticated algorithms via external classes without recompiling the integration framework. In the case of the integration of the gravitational force assuming MOND, the framework can optionally be instructed to automatically approximate the interpolation functions, $\mu(x)$, by B-splines[3]. In the case of MOND with interpolation function (1.9), this reduces the time required for the numerical integration by a factor of about 100.

Fig. 3.7 to 3.8 show the ratio $\Delta b/\Delta b_P$ between the result of the integration, Δb, and that of the point mass calculation, Δb_P. That ratio is plotted against the distance, r_{near}, between a mirror and its adjacent sphere at the near position (see Fig. 3.1). It can be seen that $\Delta b/\Delta b_P$ depends on the distance r_{near}. In the case of $r_{\text{near}} = 80$ cm, the ratio is about 0.97. Thus the integration must not be neglected. In order to calculate Δb, the partial accelerations in (3.7) respectively (3.8) have to be integrated according to (3.5) instead of using (3.15).

---

[2] These bodies can be simple shapes that inherit from TGeoShape or of type TGeoCompositeShape, i.e. can be any boolean composition of simpler shapes like e.g. tubes, spheres or boxes.

[3] B-splines are a special kind of smoothly connected third-order polynomials (see [Blo98])

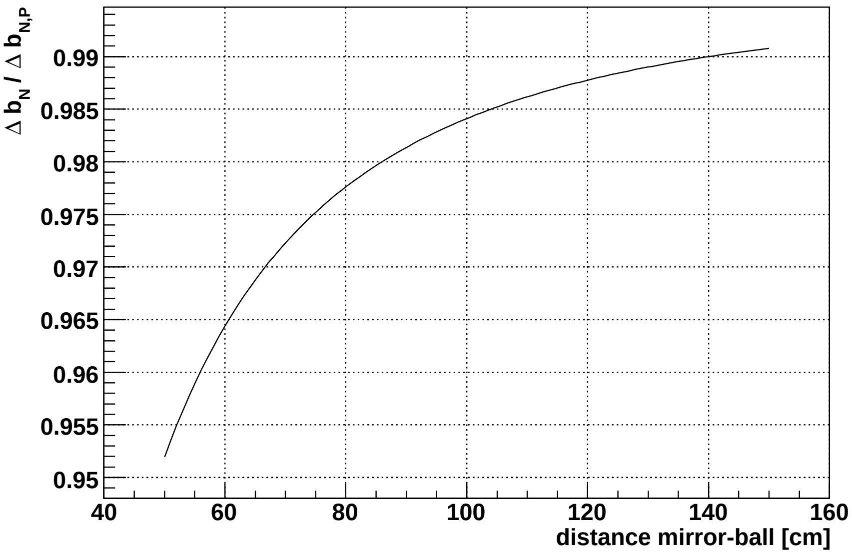

Figure 3.7: Ratio $\Delta b_N/\Delta b_{N,P}$ between the result of numerical integration, Δb_N, and that of the point mass calculation, $\Delta b_{N,P}$, in case of Newton's law. This ratio does not depend on the mass M of the field masses, since in the case of Newton $\Delta b \propto M$. As in Fig. 3.2, the deviation is plotted against the near position of the spheres.

Analytical vs Numerical Integration

In the case of Newton's law of gravitation, the force between a mirror and a sphere can be integrated analytically as long as the mirror and the sphere share the same symmetry axis. In that case the numerical integration can be compared directly to the analytical integration. This has been done, and both calculations lead to the same result. If the sphere is shifted perpendicularly out of the symmetry axis by a small Δx, the force can no longer be integrated analytically. To check anyway the numerical integration for consistency, the force can be approximated using a taylor expansion with respect to Δx which gives

$$F(r, \Delta x) = F_{\mathrm{sym}}(r) \cdot \left(1 + f_2(r)\Delta x^2 + f_4(r)\Delta x^4 + \mathcal{O}(\Delta x^6)\right) \tag{3.17}$$

whereas $F_{\mathrm{sym}}(r)$ is the force in the symmetrical case and $f_2(r)$ and $f_4(r)$ are the 2nd- and 4th-order expansion terms that can be calculated analytically as well. The terms $f_2(r)$ and $f_4(r)$ have been calculated using MATHEMATICA. All odd expansion terms vanish since the force $F(r, \Delta x)$ does not depend on the sign of Δx. The numerically integrated force has been compared with the force approximated by Eq. (3.17) and both calculations give the same result.

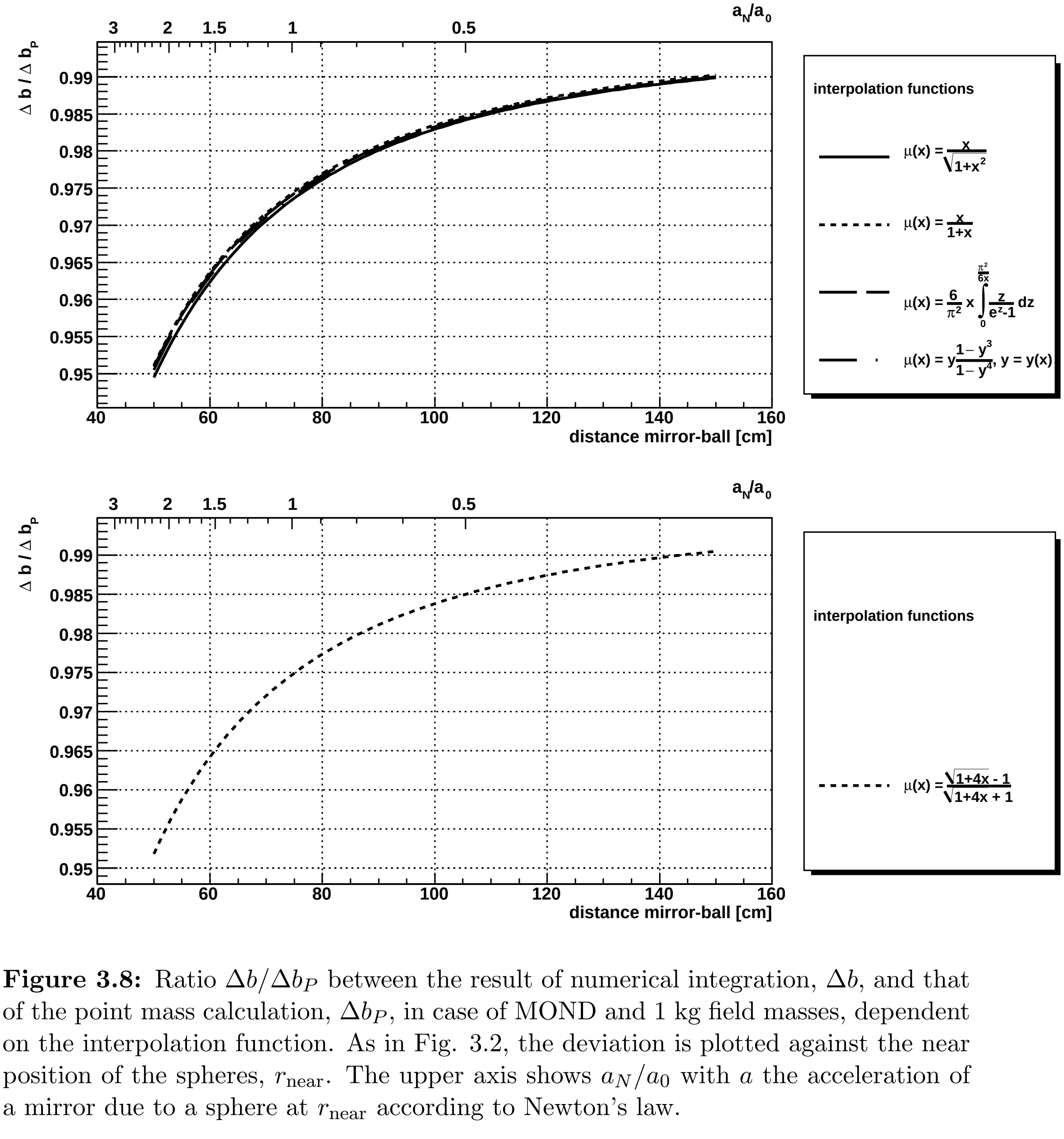

Figure 3.8: Ratio $\Delta b/\Delta b_P$ between the result of numerical integration, Δb, and that of the point mass calculation, Δb_P, in case of MOND and 1 kg field masses, dependent on the interpolation function. As in Fig. 3.2, the deviation is plotted against the near position of the spheres, r_{near}. The upper axis shows a_N/a_0 with a the acceleration of a mirror due to a sphere at r_{near} according to Newton's law.

3.5 Ambiguities connected with MOND

To close this chapter, a still open question has to be addressed that can be traced back to Chap. 1.4 which was dedicated to deal with the restrictions concerning the measurement process. According to Eq. (3.7) in Chap. 3.1, the following prescription is provided to calculate the change, Δb, of the mirror distance: First of all the acceleration $a_{\text{res}} = F/M_{\text{mirr}}$ has to be calculated separately for the cases

$$\begin{array}{ll} a_{\text{res}}(r_{L,\text{near}}) & a_{\text{res}}(r_{R,\text{near}}) \\ a_{\text{res}}(r_{L,\text{near}} + b_0) & a_{\text{res}}(r_{R,\text{near}} + b_0) \\ a_{\text{res}}(r_{L,\text{far}}) & a_{\text{res}}(r_{R,\text{far}}) \\ a_{\text{res}}(r_{L,\text{far}} + b_0) & a_{\text{res}}(r_{R,\text{far}} + b_0) \end{array}$$

Each of these terms describes a gravitationally induced acceleration of one mirror (left or right) due to one sphere (left or right) at a specific position (near or far). These accelerations have then to be summed up properly according to Eq. (3.7) and have to be divided finally by ω_0^2 in order to get Δb. In the case of MOND the sum goes over the modified accelerations.

Instead of doing it that way, one could argue differently: First of all one could calculate the resulting acceleration of each mirror according to Newton's law both for the spheres at the near and at the far positions

$$\begin{aligned} \Delta a_{N,L,near} &= a_N(r_{L,\text{near}}) - a_N(r_{R,\text{near}} + b_0) \\ \Delta a_{N,R,near} &= a_N(r_{R,\text{near}}) - a_N(r_{L,\text{near}} + b_0) \\ \Delta a_{N,L,far} &= a_N(r_{L,\text{far}}) - a_N(r_{R,\text{far}} + b_0) \\ \Delta a_{N,R,far} &= a_N(r_{R,\text{far}}) - a_N(r_{L,\text{far}} + b_0) \end{aligned} \tag{3.18}$$

with $\Delta a_{N,L,near}$ as the resulting acceleration of the left mirror due to the spheres at the near positions and $\Delta a_{N,R,near}$ as the analogous acceleration of the right mirror, etc...

In that case Δb would finally be given by

$$\Delta b = \frac{1}{\omega_0^2}\big(a(\Delta a_{N,L,near}) + a(\Delta a_{N,R,near}) - a(\Delta a_{N,L,far}) - a(\Delta a_{N,R,far})\big) \tag{3.19}$$

with e.g. $a(\Delta a_{N,L,near})$ as the modified acceleration that can be calculated from its Newtonian counterpart $\Delta a_{N,L,near}$ according to Chap. 3.2.

In the case of Newton's law, both ways of calculating Δb are equivalent. In the case of MOND this equivalence does not hold. This ambiguity leads to the following question: Do we have to calculate Δb for both summation philosophies in order to complete this chapter? The second way of summing up will only predict deviations from Newton if absolute accelerations are weak. This can be seen using Eqn. (3.18). If the resulting accelerations of the mirrors are calculated according to (3.18), all partial accelerations that act upon the mirrors have to be regarded on the right hand side, including the g-vector. Thus the magnitude of the resulting acceleration of each mirror exceeds by far a_0, since on earth the mirrors are exposed to a strong gravitational potential. But according to the assumption in Chap. 1.4, an experiment carried out on earth could only measure deviations if relative accelerations need to be weak. This way of interpreting MOND corresponds to the first way of calculating Δb that is explained in Chap. 3.1. Thus only this way has to be regarded in the context of the experiment.

Chapter 4

Analysis Methods

This chapter is dedicated to the question of how the change of mirror distance, Δb, respectively the shift of the resonance frequency, Δf_R, caused by the movement of the spheres, can be determined from a measurement. Different methods that can separate the signal from the background are proposed and their advantages and disadvantages are discussed.

4.1 Introduction

Fig. 4.1 shows a measurement of resonance frequencies lasting about 13 hours that was started on August 27, 2009. With a period of 40 minutes, test spheres of 11.7 kg were moved periodically between the far and the near positions. The resonance frequency is measured once every second and averaged over 2 minutes. The averages are plotted against the elapsed time. After separating the signal from a slowly varying background that is mainly caused by alignment changes of the resonator due to longterm effects like e.g. variation of temperature (see Chap. 6), a periodic rectangular profile remains that is overlayed with noise. The lower values (black) correspond to the resonance frequency measured when the spheres were placed at the near position. These are called the signal values. The upper values (grey) correspond to the far position of the spheres and are called reference values.

As long as the measurement is not spoiled by systematics, the histograms of both the signals and the references give a gaussian distribution (see Fig. 4.2). The shift of the resonance frequency, Δf_R, is then given by the difference of the means of both distributions. Using Eq. (2.4), the frequency shift can finally be translated into a change, Δb, of the mirror distance.

But since the signal is modulated with a slowly varying background, it has to be extracted from the background before the frequency shift, Δf_R, can be determined according to the above procedure. Methods to get rid of the background are explained in Chap. 4.2.

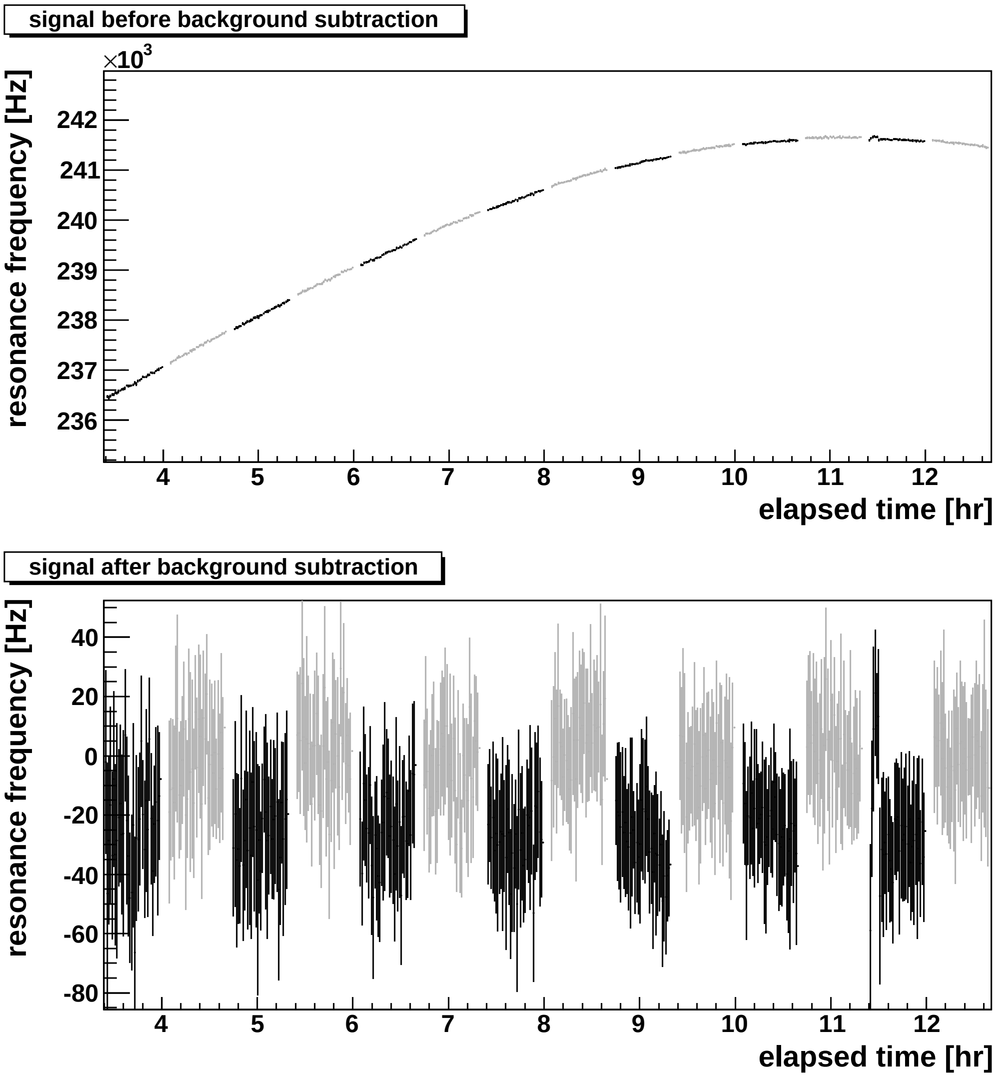

Figure 4.1: A measurement of the resonance frequency, startet on August 27, 2009, averaged over 2 minutes: The resonance frequency is plotted against the elapsed time of the measurement, **above:** before the background subtraction, **below:** after the background subtraction. With a period of 40 minutes, spheres of 11.7 kg were repositioned between far and near positions. This period can be seen in the below plot. The grey values (references) were measured with the spheres at the far position. The black values (signals) correspond to the near position. The gaps indicate the mass movement. The data taken during this time are rejected.

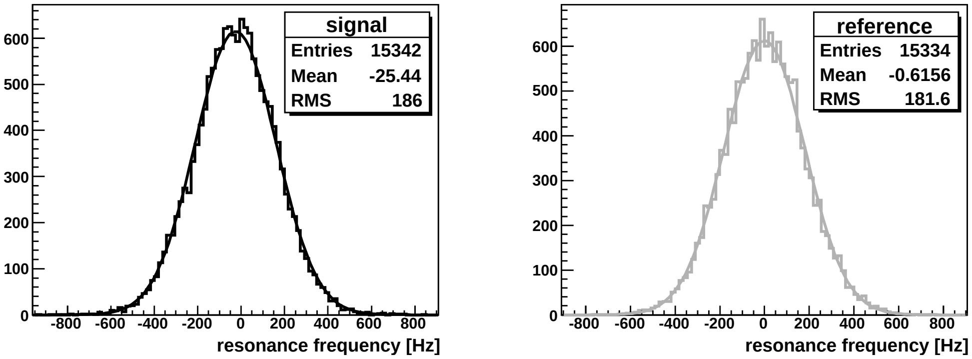

Figure 4.2: Histograms of the signals and the references of the measurement shown in Fig. 4.1, but without averaging over 2 minutes: Both histograms give gaussian distributions. The shift of the resonance frequency, Δf_R, is given by the difference of the means of both distributions, in this case $\Delta f_R = (25 \pm 2)$ Hz.

4.2 Separating Signal from Background

4.2.1 Approximating the Background by a Polynomial

The first method approximates the background by a polynomial that covers the whole range of the measurement. This method can be applied in the case of a smooth background. If the background is discontinuous, the data will have to be separated at these discontinuities into pieces with a smooth background.

For each of these pieces, the measured resonance frequencies are separated into signals and references as explained in Chap. 4.1. The background polynomial is only fitted to the references. After that the polynomial is subtracted from both the signals and the references. To finally get the frequency shift, Δf_R, the method of Chap. 4.1 is applied to these data. As a cross-check the references and the signals can be interchanged which should give the same result.

But if the background polynomial is only fitted to the references, only half of the data will be used for the fit. The signals, which are not used, include additional information. Using also them would improve the fit. If on the other hand both the signals and the references are used to fit the background polynomial, parts of the periodic rectangular signal will be mistaken as background. Then the frequency shift would systematically be too small. To avoid that, one could think of subtracting the spectral components that correspond to the periodic rectangular signal from the fitted background polynomial before this polynomial is subtracted from the data. If Δf_R is the expected shift of the resonance frequency due to the movement of the spheres, with T_{FM} as the time the spheres spend in the near or in the far position, the fourier expansion of the periodic rectangular signal will be given by

$$f_R(t) = \frac{\Delta f_R}{\pi} \sum_{n=1}^{\infty} \frac{1}{n} \big(1 - \cos(n\pi)\big) \sin(2\pi n t / 2T_{FM}) \tag{4.1}$$

Correcting the fitted background polynomial $p_{BK}(t)$ from artefacts of $f_R(t)$ means to apply a bandstop filter to $p_{BK}(t)$ at the frequencies $n/2T_{FM}$ with $n = 1 \ldots \infty$. As shown in Chap. 2, the resonance frequencies are measured with at least a period of $T = 0.5$ s. According to the Nyquist criterion, only spectral components with $n/2T_{FM} < 1/2T$ appear at its designated positions. Higher frequencies fold back and the associated spectral components show up at positions within the interval $0 \ldots 1/2T$ that can not be associated unambiguously with the periodic rectangular signal, $f_R(t)$. Thus, instead of providing a satisfying solution, the subsequent application of a bandstop filter would only complicate the analysis. A method that allows to fit the background polynomial to both the reference and the signal data at the same time without the need of correcting the fitted polynomial afterwards is explained in the next section.

4.2.2 Including a periodic Step Function

The following method extends the previous one, proposed in Chap. 4.2.1, by fitting additionally a step function to the data. This allows to fit the background polynomial to both the signal and the reference data without mistaking parts of the periodic rectangular signal as background.

Assuming Δf_R as the frequency shift that has to be extracted and $p_{\mathrm{BK}}(t)$ as the background polynomial, the data can be modelled as

$$F(t) = \Delta f_R \cdot T(t) + p_{\mathrm{BK}}(t) \tag{4.2}$$

where $T(t)$ is a step function with $T = -1/2$ when the field masses are at the near position and $T = +1/2$ otherwise. In order to separate the signal from the background, the model $F(t)$ is fitted to both the signal and the reference data with Δf_R and the coefficients of $p_{\mathrm{BK}}(t)$ as the free parameters. This method is equivalent to simultanously fitting a polynomial to the reference data and another one to the signal data whereupon both polynomials share the same coefficients apart from the constant shift. The difference in the constant shift is then given by Δf_R.

The frequency shift, Δf_R, can either be taken directly from the corresponding parameter, Δf_R, of the fitted $F(t)$ or it can be calculated as explained in Chap. 4.1 after the fitted background polynomial $p_{\mathrm{BK}}(t)$ has been subtracted from the data. The latter way allows to apply some post processing algorithm to improve the result, like e.g. filter techniques or subtracting the sliding average that is explained in Chap. 4.2.6.

4.2.3 Determining the Degree of the Polynomial

The methods explained in Chap. 4.2.1 and 4.2.2 approximate the background by a polynomial $p_{\mathrm{BK}}(t)$. This section is dedicated to the question of how overfitting can be avoided, in other words: how the degree of the polynomial can be determined such that it describes the data sufficiently without approximating also the statistical fluctuations.

The standard method is to start a polynomial fit assuming degree 1 and to repeat this fit with ascending degree until the χ^2 falls below $d = n - k$ with d the number of degrees of freedom, n the number of data points to which the polynomial is fitted and k the number of the coefficients of the polynomial.

To extend this method, the Bayesian information criterion [Sch78] can be used. This approach is based on the concept of entropy. If a polynomial $p_{\mathrm{BK}}(t)$ of degree d is fitted to n data points, the number

$$\mathrm{BIC} = \chi^2 + d \cdot \ln n \tag{4.3}$$

will have the meaning of the relative loss of information when a given model $p_{\mathrm{BK}}(t)$ is chosen to describe the data. The BIC value (4.3) will be minimal if the degree d of the fitted polynomial is optimal. Fig. 4.3 shows the data of a frequency measurement started on November 17, 2009. The above plot shows a polynomial of degree 18 fitted to the data. The polynomial of degree 50 shown in the below plot already has the tendency to approximate the statistical fluctuations and additionally oscillates at the boundaries. In Fig. 4.4 the BIC value is plotted against the degree of a polynomial that has been fitted to the data shown in Fig. 4.3. A sharp minimum at degree 8 can be seen.

An alternative and quite sophisticated way to determine the degree of the polynomial is inspired by [Bis95]: First of all the n data points to which the polynomial has to be fitted are randomly partitioned into fit and control samples. This is done by randomly marking each data point with equal probability as fit or control sample. Only the $n/2$ points marked as fit samples are used to fit the background polynomial. In order to find the degree of the polynomial, it is fitted to the fit samples with increasing degree, starting with degree 1. For each fit, the χ^2 is calculated as

$$\chi^2 = \chi^2_{\mathrm{fit}} + \chi^2_{\mathrm{ctrl}} \tag{4.4}$$

with χ^2_{fit} and χ^2_{ctrl} the χ^2 values of the fit respectively the control samples. The value χ^2_{fit} goes to zero as the degree of the polynomial goes to $n/2 - 1$. But since the control samples are not used for the fit, χ^2_{ctrl} will increase if the polynomial starts to overfit the fit samples. Hence, the χ^2 according to Eq. (4.4) will have a minimum if the degree of the background polynomial will be optimal. In Fig. 4.4 the χ^2 given by Eq. (4.4) is plotted against the degree of a polynomial that is fitted to the data of the measurement shown in Fig. 4.3. It can be seen that a polynomial with a degree between 15 and 25 is acceptable. Therefore the

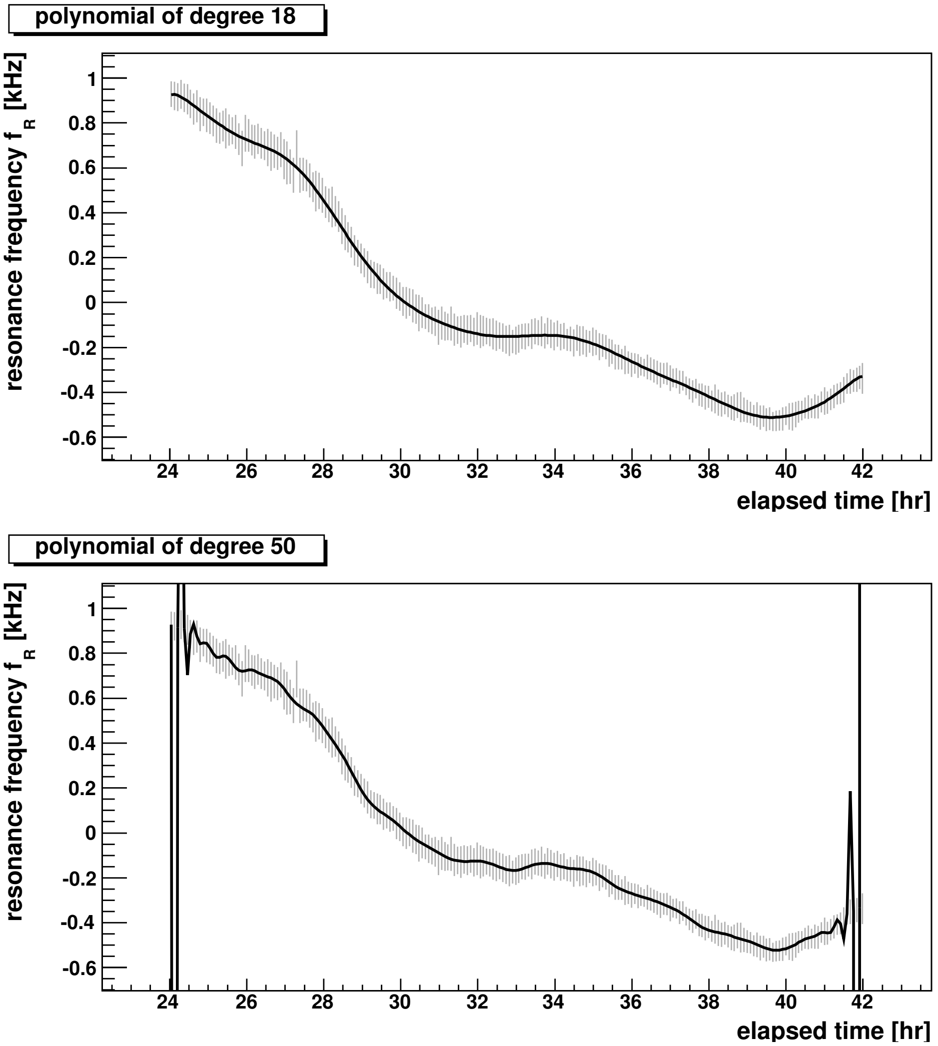

Figure 4.3: A measurement of the resonance frequency startet on November 17, 2009, averaged over 5 minutes, 216 data points: **above:** a polynomial with degree 18 describes the data (grey) sufficiently, **below:** a polynomial with degree 50 is already overfitted and additionally shows oscillations at the boundaries.

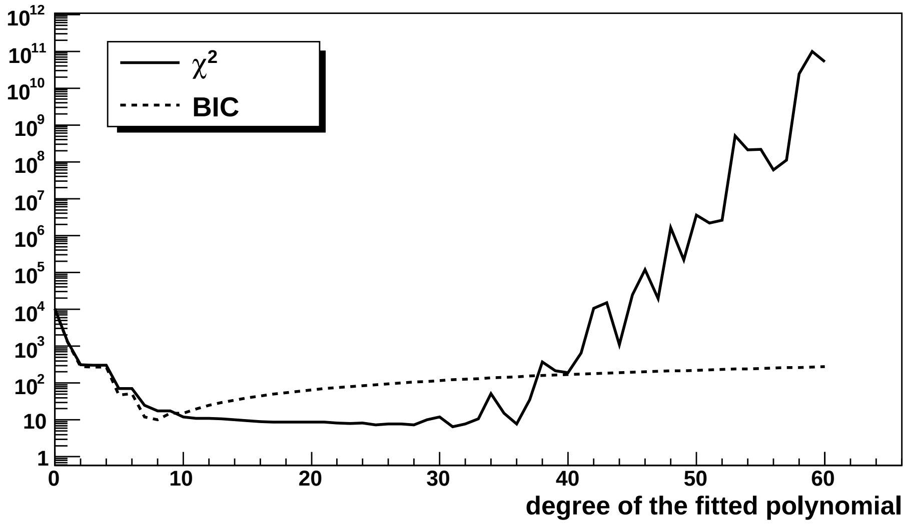

Figure 4.4: The values χ^2, see Eq. (4.4), and BIC, see Eq. (4.3), plotted against the degree of the polynomial that is fitted to the data of the measurement shown in Fig. 4.3: To the BIC a constant was added such that its minimum is equal to that of χ^2. The optimal degree of the polynomial can be found at the minimum of χ^2 respectively BIC.

polynomial of degree 18 plotted in Fig. 4.3, above, describes the data sufficiently. The sharp increase of χ^2 between degree 30 and 60 indicates overfitting and is mainly caused by oscillations of high order polynomials at the boundaries (see Fig. 4.3, below).

If the background polynomial $p_{\mathrm{BK}}(t)$ is a sum of orthonormal base polynomials, e.g. Tchebycheff polynomials, its coefficients can be calculated independently. This simplifies the numerical calculations in such a way that especially the polynomial fit with ascending degree is accelerated tremendously. The whole procedure of randomly partitioning the data into fit and control samples, fitting $p_{\mathrm{BK}}(t)$ respectively the model (4.2) to the fit samples until (4.4) becomes minimal, subtracting $p_{\mathrm{BK}}(t)$ from the data and determining Δf_R is repeated until enough Δf_R are collected to create a gaussian distribution. The final result is then given by the mean $\langle \Delta f_R \rangle$ of this distribution.

The method that randomly partitions the data into fit and control samples and the one that uses the Bayesian information criterion (BIC) differ in their predictions concerning the optimal degree of the polynomial (see Fig. 4.4). On the one hand the BIC method is faster because the polynomial only has to be fitted once. On the other hand the random partition method is very sensitive to unexpected oscillations caused by high order polynomials. The BIC method seems to be „blind“ to these oscillations because (4.3) only increases in case of high order polynomials due to the additional term $d \cdot \ln n$. Thus, if these oscillations have to be avoided randomly partitioning the data into fit and control samples will be the recommended way. Furthermore this method combines the information from fitting different partitions which could lead to better robustness in the case of irregular noise.

4.2.4 Approximating the Background by B-Splines

If the background is of a more complicated structure and if a polynomial is fitted to the whole range of the measurement, a high order polynomial will be needed in order to approximate the background sufficiently. But as already shown in Fig. 4.3, below, polynomials of high order can lead to unexpected behaviour like e.g. oscillations.

In order to avoid this, the background can be approximated by fitting B-splines to the references and subtracting them from the data. B-splines are chains of smoothly connected, usually cubic polynomials. The positions along the x-axis at which these polynomials are connected are called knots. A method of approximating data by B-splines is explained in detail e.g. in [Blo98]. But calculations of the frequency shift using B-splines show that the result is very sensitive to the number and the position of the knots. Furthermore artefacts occur at the positions of the knots. This additionally biases the result. Thus, approximating the background by a B-spline is not recommended. Since the knots have to be chosen carefully, especially those spline algorithms are not suitable that determine the number and the position of the knots automatically.

4.2.5 Sliding Background Polynomials

A method that approximates complex backgrounds without using high order polynomials but does not share the disadvantages of B-splines has been proposed in [Sch99]. As described in Chap. 4.2.1, the data are separated into signals and references. For each connected signal interval the background is approximated separately. This is done in the following way: Each signal interval is considered that has at least one reference interval at its left and its right side. To all data points within these both reference intervals, a polynomial is fitted. In that case polynomials of degree 5 are adequate to approximate the background. The degree can also be determined using the methods of Chap. 4.2.3. After the fit, the background polynomial is subtracted from the data of the enclosed signal interval. This procedure is repeated for each signal interval. The corrected data of all signal intervals should distribute according to gaussian distribution with its mean at the frequency shift, Δf_R. If, as in Chap. 4.2.2, a step function is used, the data of the enclosed signal interval can also be used to fit the polynomial. That could lead to better robustness.

Alternativley one could fit for each signal interval a straight line to both the left and the right reference interval. The background of the signal interval could then be estimated by a third order polynomial that interpolates smoothly between the left and the right line.

4.2.6 Sliding Average Method

Backgrounds of a more irregular nature can not be modelled as polynomials. In that case the sliding average of the measured signal may be a better approximation of the background. If T_{FM} is the time the spheres spend in the near or in the far position, then for each data point at time t, the background is computed as the average of all measured frequencies between $t - T_{FM}$ and $t + T_{FM}$. If the background varies strongly within this interval, the average has to be corrected by fitting a polynomial and subtracting it from the data before calculating the average. Moreover data with excessive noise have to be rejected. After calculating the sliding average at each data point, the data have to be corrected by subtracting the background.

The procedure of approximating the background by the sliding average and subtracting it from the data can be repeated iteratively.

4.3 Error Estimation

The result of a measurement is given by a frequency shift Δf_R and its error $\sigma_{\Delta f_R}$. To see if the error, $\sigma_{\Delta f_R}$, is correctly estimated, a statistically significant number of similar measurements has to be analysed. From the result of each measurement, Δf_R, the pull is calculated according to

$$\Delta_{\text{pull}} = \frac{\Delta f_R - \langle \Delta f_R \rangle}{\sigma_{\Delta f_R}} \tag{4.5}$$

with $\langle \Delta f_R \rangle$ the weighted average of all individual measurements, Δf_R.

If the errors of the single measurements, $\sigma_{\Delta f_R}$, are correctly estimated, the pulls are distributed according to a gaussian distribution with center 0 and width 1. If the width is greater than 1, the individual errors are very likely underestimated. In that case the individual errors have to be multiplied by the width of the pull distribution to obtain their correct values. A width of the pull distribution that is lower than 1 indicates that the errors may have been overestimated.

4.4 List of Analysis Methods

To finalize this chapter, six analysis methods are presented which mainly differ in their ways of separating the signal from the background. In order to subtract the background they use a method explained in Chap. 4.2. The analysis method

A1 has been developed by the author of this thesis. The methods A2 to A6 are used as control methods.

A1 The data are separated into pieces with a smooth background. Data with high fluctuations are rejected. For each smooth piece the following method is applied: The background is approximated by a sum of orthogonal base polynomials whose recursion formula is calculated according to [Blo98]. Additionally a step function is fitted as explained in Chap. 4.2.2, so that both the signal and reference data can be used for the fit. As a first guess the Bayesian information criterion is used to determine the degree of the polynomial (see Chap. 4.2.3). After the fit the background polynomial is subtracted from the data. Data with a spread of more than 5σ are rejected. Then the background polynomial is fitted again to the remaining data. The degree of the polynomial is now determined by randomly separating the data into fit and control samples (see Chap. 4.2.3). After subtracting this polynomial from both the signal and the reference data, the frequency shift is calculated as explained in Chap. 4.1.

A2 After separating the data into smooth pieces, the background is approximated for each piece by the sliding average as explained in Chap. 4.2.6. The sliding average is iterated twice and a correction is applied to take into account the effect of the gaps in the data during the movement of the spheres.

A3 Like in method A1, the background is approximated by a periodic step function and the sum of orthogonal base polynomials. In contrast to method A1, Tchebycheff polynomials are used as base polynomials. To prevent overfitting the data are randomly separated into fit and control samples (see Chap. 4.2.3). The degree of the polynomial is increased until the χ^2 is in the vicinity of the minimum, i.e. until $\chi^2 < 1.05\chi^2_{\text{min}}$.

A4 The background is approximated separately for each signal interval by fitting a straigt line to both the left and the right reference interval and smoothly interpolating a third order polynomial between these lines (see Chap. 4.2.5). Data with high fluctuations are rejected

A5 The background is approximated by the sliding average as explained in Chap. 4.2.6. In contrast to A2 no iteration is applied.

A6 The data are separated into smooth pieces of at least 4 hours. For each a 5-th or a 7-th order polynomial is fitted to the reference data in order to approximate the background. As a cross-check the polynomial is also fitted to the signal data.

Chapter 5

Monte Carlo Tests

In order to compare the analysis methods of Chap. 4.4 and check them for correctness, resonance measurements with a frequency shift of 6 Hz and different backgrounds were created by a Monte Carlo generator.

5.1 Description of the Monte Carlo Data

Five data samples were generated. Each sample contains either 50 or 100 measurements. Each measurement has a length of 40 hours and is a time series of resonance frequencies with a period of 72 seconds in order to simulate a measurement with 1s intervals that has been averaged over 72 seconds. The frequency shift of 6 Hz is simulated with a period of 2 hours in order to simulate a change of the field mass positions each hour. As the slowly varying background, a third order polynomial was added to each measurement. In order to simulate regular statistical noise, at each data point a value between $+7.5$ and -7.5 Hz was randomly chosen with equal probability. This value was added to the data point. To four of these five Monte Carlo samples highly irregular noise was added. The irregular noise was introduced in order to approximate the characteristic short term fluctuations that can be seen in all frequency measurements and whose nature is still unknown. This noise was generated by one of the following two methods:

1. each 40 hour measurement is randomly separated into intervals of variable length between 0.06 and 0.3 hours. For each interval, uniformly distributed noise is added to its data points. The value of the noise is chosen with equal probability between 0 and ± 14 Hz respectively.

2. each 40 hour measurement is randomly separated into intervals of variable length between 0.5 and 1 hours. For each interval, a constant frequency value is randomly chosen between ± 22 Hz. This value is added to all the frequencies within this interval.

In both cases the irregular noise averages to zero by construction. The data samples created by the Monte Carlo generator are:

1. 50 measurements with irregular noise created by method 1
2. 50 measurements with irregular noise created by method 1 but fluctuations have double amplitude
3. 50 measurements without irregular noise, only with the regular ±7.5 Hz noise
4. 50 measurements with irregular noise created by method 1, background polynomials have opposite curvature
5. 100 measurements with irregular noise created by method 2

5.2 Results

Tab. 5.1 and 5.2 summarize the results of the five Monte Carlo samples. The first row shows the results obtained by the analysis method A1. The results of the five control methods can be found in the below rows. In Fig. 5.1 to 5.4 the distributions of the 50 respectively 100 results $\Delta f_i \pm \sigma_{\Delta f,i}$ and their pulls $\Delta_{\text{pull},i} = (\Delta f_i - \Delta\bar{f})/\sigma_{\Delta f,i}$ are plotted for each MC sample.

The results of method A1 agree with 6 Hz for each MC sample. In the case of MC sample 3 with regular noise, the width of the pull distribution is about 0.8. Thus the errors of the 50 individual results within this sample are slightly overestimated. In the case of the MC samples with irregular noise the individual errors are underestimated since the width of the pull distribution is up to ≈ 4.5. A single measurement does not provide sufficient information to estimate the error correctly. A statistically significant number of similar measurments has to be analysed, especially in the case of irregular noise.

Fig. 5.6 shows the distribution of the degrees of the background polynomials that are associated with the 50 measurements of MC sample 4. Each entry represents the degree of the background polynomial of one of the 50 measurements within this sample. Although only a second order polynomial was used to simulate the background (see Chap. 5.1), polynomials with a degree between 23 and 81 are necessary to approximate the additional irregular noise. Polynomials of smaller degrees do not describe the noise adequately and lead to a bias. Thus the degree has to be predicted correctly. As shown in Chap. 4.2.3, Fig. 4.4, the Bayesian information criterion predicts smaller degrees than the separation of the data into fit and control samples. Consequently the degree of the background polynomial should be determined with the latter method.

method	$\Delta f_R(1)$ [Hz]	$\Delta f_R(2)$ [Hz]	$\Delta f_R(3)$ [Hz]
A1	6.03 ± 0.21	5.86 ± 0.24	6.000 ± 0.028
A2	6.03 ± 0.18	6.02 ± 0.35	6.028 ± 0.024
A3	6.06 ± 0.11	5.95 ± 0.21	6.000 ± 0.028
A4	6.01 ± 0.18	6.03 ± 0.34	6.028 ± 0.026
A5	6.03 ± 0.18	6.03 ± 0.32	6.028 ± 0.024
A6		6.83 ± 0.09	

Table 5.1: Results of the Monte Carlo data samples 1, 2 and 3, dependent on the analysis method.

method	$\Delta f_R(4)$ [Hz]	$\Delta f_R(5)$ [Hz]
A1	6.10 ± 0.18	5.982 ± 0.028
A2	6.59 ± 0.26	6.020 ± 0.027
A3	6.04 ± 0.17	5.982 ± 0.027
A4	6.66 ± 0.27	
A5	6.59 ± 0.26	
A6	6.42 ± 0.13	5.892 ± 0.025

Table 5.2: Results of the Monte Carlo data samples 4 and 5, dependent on the analysis method.

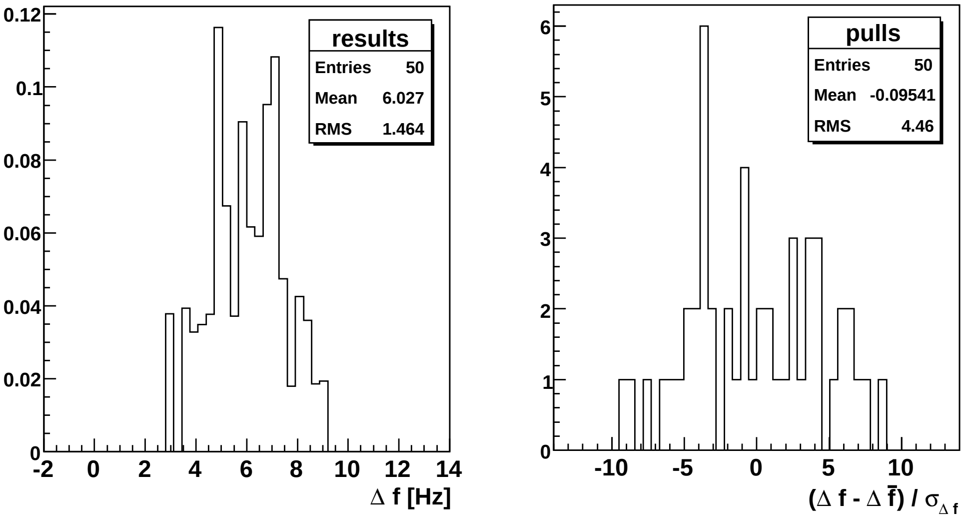

Figure 5.1: MC sample 1: Distributions of the results, Δf, and the pulls, $(\Delta f - \Delta\bar{f})/\sigma_{\Delta f}$, obtained by analysis method A1.

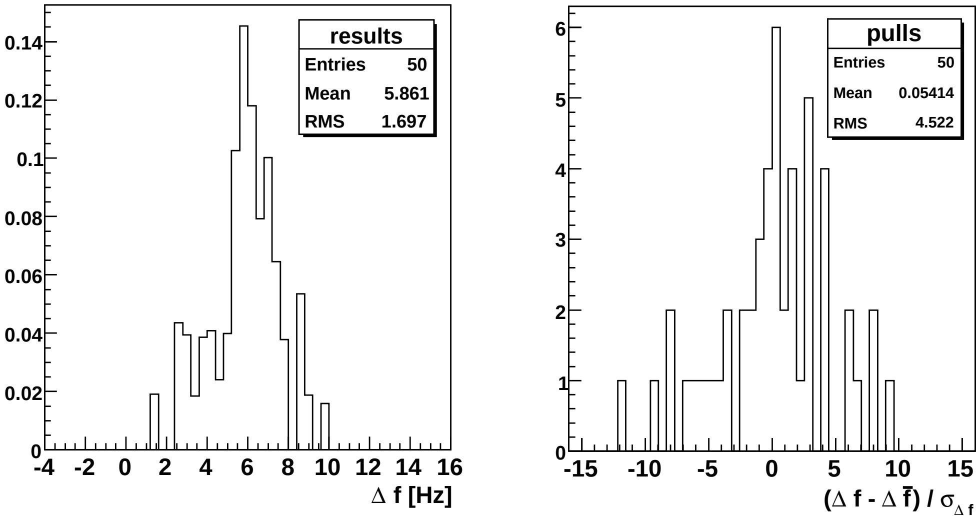

Figure 5.2: MC sample 2: Distributions of the results, Δf, and the pulls, $(\Delta f - \Delta\bar{f})/\sigma_{\Delta f}$, obtained by analysis method A1.

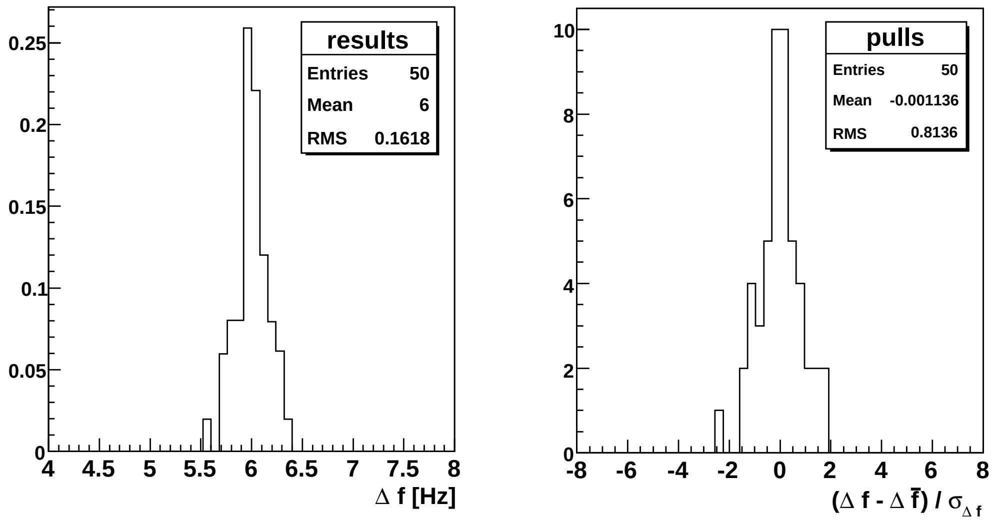

Figure 5.3: MC sample 3: Distributions of the results, Δf, and the pulls, $(\Delta f - \Delta \bar{f})/\sigma_{\Delta f}$, obtained by analysis method A1.

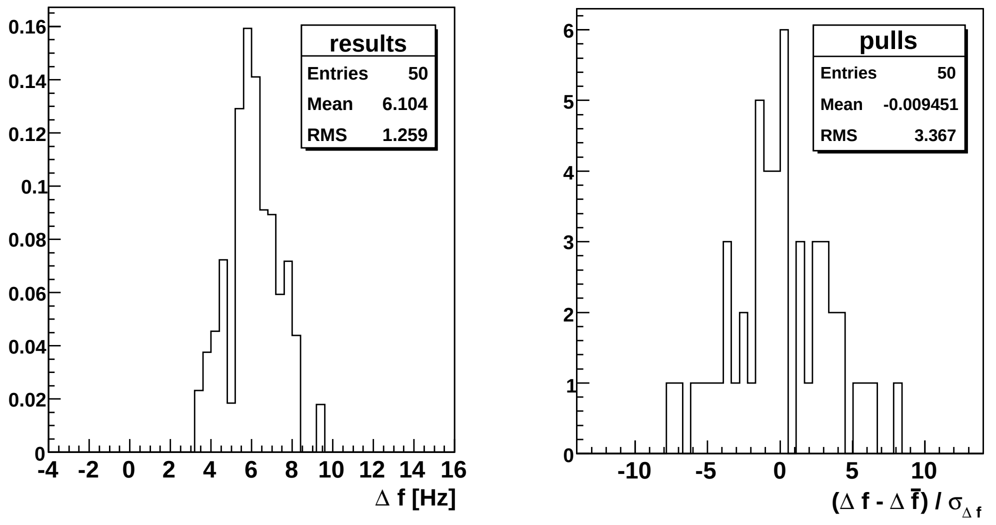

Figure 5.4: MC sample 4: Distributions of the results, Δf, and the pulls, $(\Delta f - \Delta \bar{f})/\sigma_{\Delta f}$, obtained by analysis method A1.

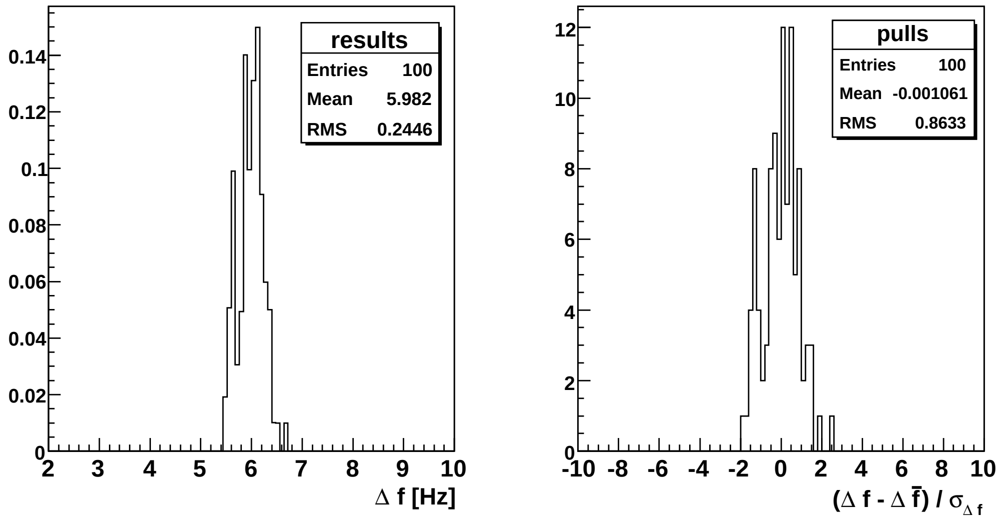

Figure 5.5: MC sample 5: Distributions of the results, Δf, and the pulls, $(\Delta f - \Delta\bar{f})/\sigma_{\Delta f}$, obtained by analysis method A1.

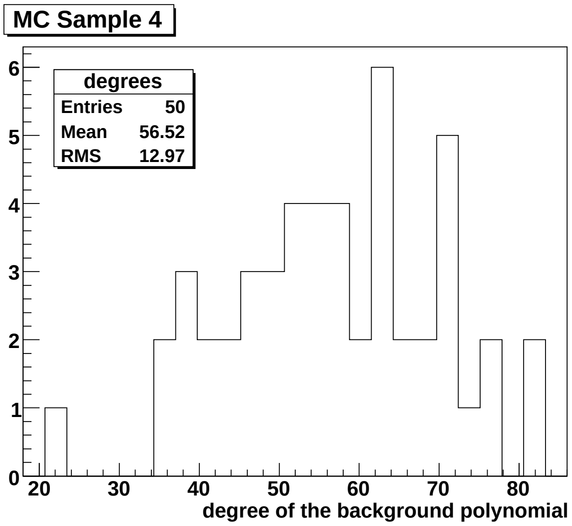

Figure 5.6: Distribution of the degrees of the 50 background polynomials in the case of MC sample 4 with irregular noise: each entry represents the degree of the background polynomial of one of the 50 measurements within this sample.

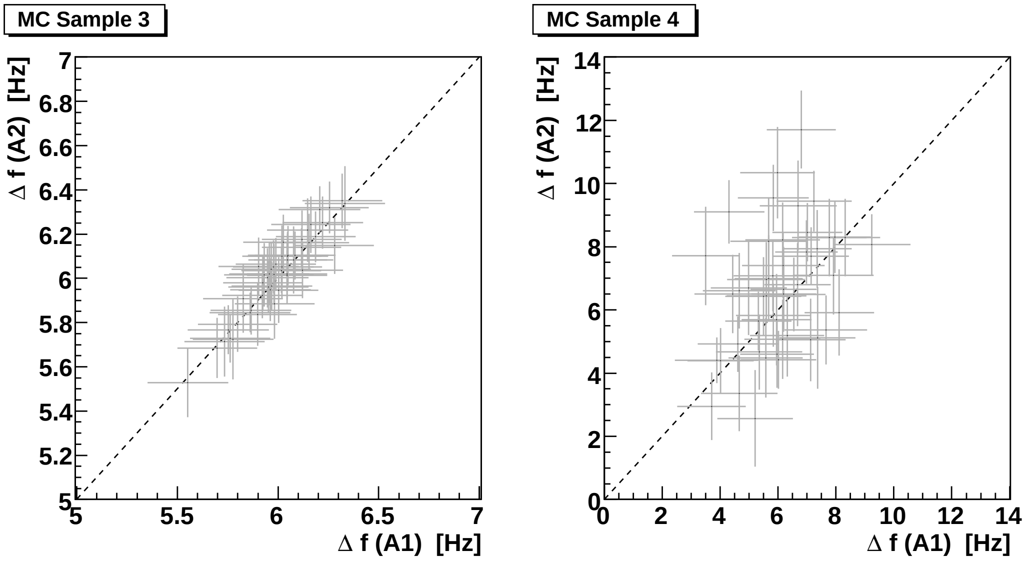

Figure 5.7: Correlation between the results obtained by method A1 and A2 in case of **left:** Monte Carlo sample 3 with regular noise and **right:** Monte Carlo sample 4 with highly irregular noise. In both cases each point represents one of the 50 measurements of the sample. The x-coordinate of a point shows the result of method A1, the y-axis the result of method A2. The dotted lines show the expected correlations.

5.3 Comparison of the Analysis Methods

In the case of sample 3 the results of all analysis methods agree with 6 Hz. Fig. 5.7, left, shows the correlation between method A1 and method A2. Each point represents one of the 50 measurements of sample 3. The x-coordinate and the horizontal error bar are the result and the error obtained by the method A1. The y-coordinate and the vertical error bar are the result and the error of method A2. The points cumulate around $(6, 6)$ and the correlation is quite clear. Thus the results of both methods agree with 6 Hz. All other possible correlation plots between the analysis methods show the same behaviour in the case of sample 3.

In the case of the Monte Carlo samples with irregular noise the results of the different analysis methods show a large spread, especially those associated with sample 4. The results of the control methods A2, A4, A5 and A6 deviate from 6 Hz by at least 2σ. Furthermore the correlation between the different analysis methods is very poor. Fig. 5.7 shows the correlation between method A1 and A2 in the case of Monte Carlo sample 4. The points still cumulate around $(6, 6)$, but the correlation is very poor. This means that in the case of a single measurement the results of the different analysis methods may neither agree with 6 Hz nor with each other. If however a statistically significant number of measurements is evaluated, the results of the analysis methods will converge since by construction the irregular noise of the Monte Carlos samples averages to zero.

It can be seen that even in the case of 50 or 100 measurements the results of the different analysis methods do not agree very well. Since irregular noise was introduced to simulate real data, a large number of similar measurements has to be analysed in order to obtain a consistent result.

Finally measurements were simulated without a signal, i.e. with 0 Hz frequency shift. The results of the different analysis methods are in agreement with 0 Hz.

Chapter 6

Systematics

According to the Monte Carlo studies shown in Chap. 5, the analysis methods explained in Chap. 4 are adequate in the case of data affected by external influences that can be described by a slowly varying background function modulated with highly irregular noise as long as this noise averages to zero.

In order to check whether this is a good model for real data, external influences are presented in this chapter. If such an influence can not be modelled in the way mentioned above, methods to minimize this influence are proposed.

6.1 Misalignment of the Resonator

According to [Kle02], a vertical tilt of the cryostat by an angle Θ along the symmetry axis of the resonator causes the mirror distance, δb, to change by

$$\delta b = \delta l \cdot \Theta \tag{6.1}$$

with δl the difference of the pendulum length of both mirror pendulums. Hence, δl has to be minimized in order to obtain the maximal insensitivity of the mirror distance to tilts. This can be done with an accuracy of about $\delta l \approx 1$ mm. A constant tilt of the cryostat only results in a constant shift of the measured mirror distance. Since only differences, Δb, of the mirror distance are measured, a constant tilt would not influence the signal. If, however, this tilt varies with time, Δb will also be time dependent. A non-constant tilt is usually caused by seismically excited motion of the steel frame or by non-uniform temperature changes within the frame that finally causes the frame to deform itself irregularly. But a time dependent temperature will not only influence the alignment of the resonator due to the changing tilt of the frame. If the suspension wires of the mirrors differ in their length, a non-constant temperature will also cause an unequal change of the length of the wires. But since the temperature only varies slowly, the corresponding variation of the resonator alignment only contributes to the slowly varying background that can be described by a polynomial. Furthermore temperature

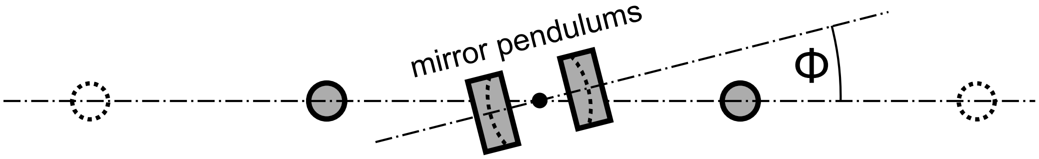

Figure 6.1: Schematic illustration of the misalignment due to a twist of the symmetry axis of the resonator by an angle Φ (top view).

induced variations of the tilt can be reduced by keeping the temperature as constant as possible. This is done via an air condition that keeps the temperature constant within 0.3 °C. Furthermore the experiment is thermally isolated.

Apart from estimating the dependency of the signal, Δb, on the tilt of the cryostat, Eq. (6.1) can be used to measure the difference, δl, of the penulum length of both mirrors: Measuring the change of the mirror distance, Δb, at different tilt angles Θ of the cryostat results in a number of associated pairs $(\Delta b, \Theta)$, since Θ can be measured independently using the tilt sensors. To obtain δl, Eq. (6.1) has to be fitted to all pairs $(\Delta b, \Theta)$ with δl as the free parameter. This measurement is time intensive and requires a well adjusted experiment. The major part of the work described by this thesis consisted of adjusting the resonator. Thus a possible measurement of δl had to be postponed to further research.

Another bias of the measured signal, Δb, due to a misalignment of the experiment occurs if the symmetry axis of the resonator is not equal to the symmetry axis of the moving field masses. If, as shown in Fig. 6.1, both axes were twisted by a small angle Φ, it would bias the measured change of the mirror distance, Δb, since

$$\Delta b \propto \cos\Phi \tag{6.2}$$

To minimize systematic errors due to misalignment, on the one hand air levels are used to adjust the lid of the cryostat horizontally, both along and perpendicular to the symmetry axis of the resonator. On the other hand laser beams are mounted on the lid. These beams point to the walls of the tent, inside which the experiment is placed, in order to be able to position the cryostat relative to the tent. On the other hand, two plumb-lines are suspended from the lid of the cryostat (see Chap. 2.1). That allows to determine the position of the cryostat relative to the field masses.

6.2 Seismic Excitations

As shown in Chap. 2.3, the pendulum resonator is a bandpass filter with frequency ω_0 which means that the transmission of seismic excitations to the mirrors depends on the frequencies of these excitations.

Seismic excitations with frequencies that are higher than the natural frequency

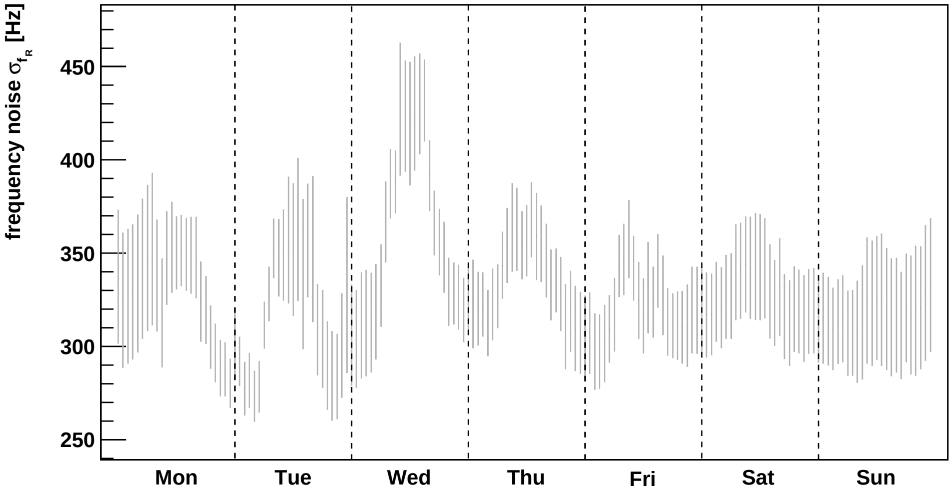

Figure 6.2: rms of the measured resonance frequency, σ_{f_R}, plotted against the weekday. The averaged frequency data have been taken from the measurements between September 1, 2009, and February 19, 2010.

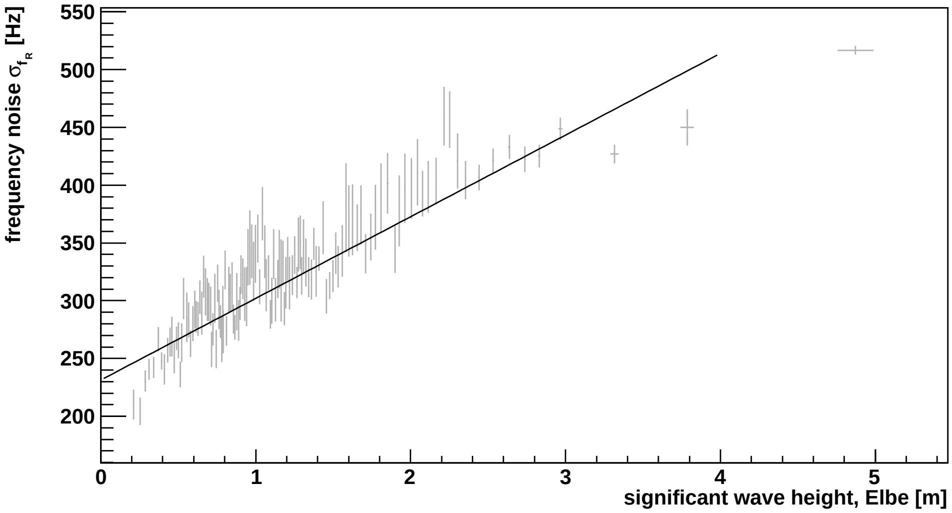

Figure 6.3: rms of the measured resonance frequency, σ_{f_R}, plotted against the wave height of the Elbe river. The frequency data have been taken from the measurements between September 1, 2009, and February 19, 2010.

ω_0 of the mirrors, e.g. frequencies between roughly 4 and 300 Hz, are usually caused by traffic, industry and related human activities. According to [Sch92] the band pass filter will reduce this noise effectively by a factor of $(\omega_0/\omega)^2$ with ω the frequency of the noise. Excitations with frequencies $\omega \ll \omega_0$ are also damped effectively. On the contrary excitations with frequencies around ω_0 are amplified due to the resonance at ω_0 by a factor of about 2.

Noise with frequencies around ω_0 is also caused by traffic. Additional sources are wind that blows against buildings or swell of nearby seas or rivers. Fig. 6.2 shows the rms of the resonance frequency, σ_{f_R}, plotted against the weekday. In Fig. 6.3 the rms is plotted against the wave height of the Elbe river. To create both plots, all measurements between September 1, 2009, and February 19, 2010, were evaluated. In Fig. 6.2 it can be seen that at daytime the noise is significantly higher than at night or at the weekend. This means that the noise is dominated by traffic.

Fig. 6.3 reveals an almost linear correlation between the wave height of the Elbe and the frequency noise. A straight line fitted to the data intersects the vertical axis at $\sigma_{f_R} = 230$ Hz. Thus noise above 230 Hz is significantly influenced by the swell of the Elbe river. Noise below 230 Hz is dominated by other sources like e.g. traffic.

As shown in Chap. 5, the seismic noise that is transmitted to the mirrors is not a problem for the analysis of the measurement as long as it is regular. Even irregular noise does not bias the result as long as the average of this noise agrees statistically with zero. In both cases the accuracy of the result only depends on the amount of data that are analysed. Furthermore averaging and filter techniques can be used to increase the accuracy. On the contrary highly irregular and sudden excitations, for example caused by earthquakes, destroy the data quality. Fig. 6.16, above, shows the Chile earthquake on February 26, 2010, at 8:00. The corresponding data have to be rejected.

6.3 Torsion and Violin Modes

Since the mirrors are not point masses and each mirror is suspended with two wire straps, a mirror can oscillate in more complex ways than a simple mathematical pendulum. Torsion modes of the mirror pendulums are possible, as well as transversal modes of the wires.

The frequency ω of a torsion mode can be calculated as

$$J\ddot{\phi} = D(\phi) \tag{6.3}$$

with ϕ a small torsion angle, $D(\phi)$ the torque of the mirror and J as the moment of inertia with respect to the center of mass of the mirror. The moment of inertia has been integrated numerically and is given by $J = 118.9$ kg cm^2. According to

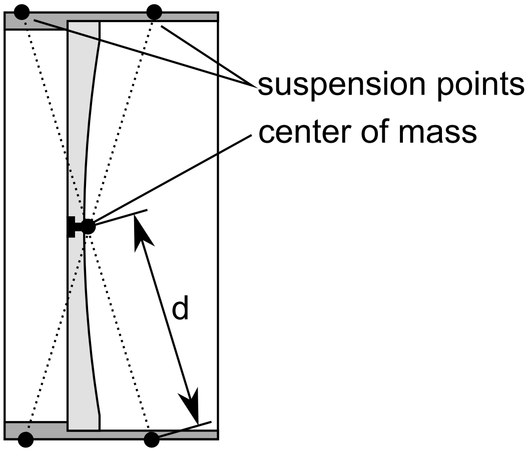

Figure 6.4: Illustration of a mirror pendulum (top view) in order to derive its torsion frequency: The four suspension points are shown. The mirror is deflected by a small angle ϕ around its center of mass whereas its rotation axis is perpendicular to the plane of projection.

Fig. 6.4, each mirror can be seen as being suspended by four wires. Then the torque $D(\phi)$ is given by

$$D(\phi) = g\, M_{\mathrm{mirr}}\, \frac{d^2}{l}\phi \tag{6.4}$$

with l the pendulum length, $M_{\mathrm{mirr}} = 3.872$ kg the mass of a mirror, $g = 9.81\ \mathrm{m/s}^2$ the local acceleration due to gravity and $d = 10.2$ cm. Replacing $D(\phi)$ in Eq. (6.3) using Eq. (6.4) results in the differential equation

$$J\ddot{\phi} = g\, M_{\mathrm{mirr}}\, \frac{d^2}{l}\phi \tag{6.5}$$

Solving Eq. (6.5) leads to a torsion frequency of

$$f_{\mathrm{tors}} = \frac{d}{2\pi}\sqrt{\frac{g\, M_{\mathrm{mirr}}}{J\, l}} = 0.55\,\mathrm{Hz} \tag{6.6}$$

The tendency of the mirrors to exhibit torsion modes can be reduced by adjusting both wire straps of each mirror, such that they carry the same fraction of the mirror weight and each wire strap is symmetrically loaded. After that the influence of the remaining torsion modes can be neglected according to [Sch92].

In addition to torsion modes each wire can be individually excited to transversal oscillations, also called violin-modes. According to [Gos04] the frequency of the n-th violin-mode of a wire is given by

$$\omega_n = \frac{n\pi}{l}\sqrt{\frac{P}{\rho\pi R^2}}\left(1 + \frac{2}{l}\sqrt{\frac{EI}{P}} + \mathcal{O}(1/l^2)\right) \tag{6.7}$$

violin mode n	1	2	3	4
f_n in Hz	22.9	45.9	68.9	91.9

Table 6.1: Frequency f_n of the n-th transversal mode of a wire according to Eq. 6.7. It is assumed that each of the four wires has to carry a quarter of the weight of one mirror that is given by $M_{\rm mirr} = 3.8$ kg.

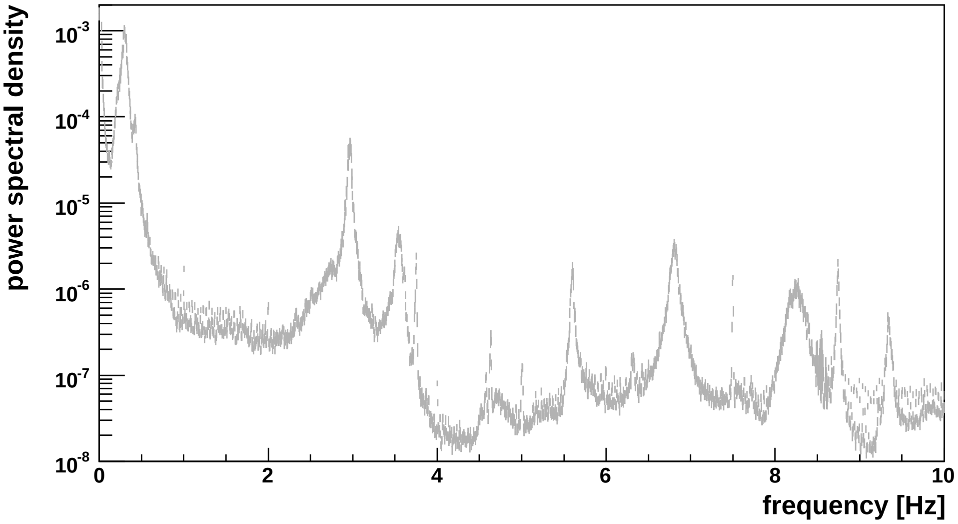

Figure 6.5: Power spectral density of the amplitude measurement started on May 27, 2010, at 11:45, plotted against the frequency: In order to get the spectrum, the amplitude of the transmitted wave was measured with 20 Hz at a fixed frequency.

where $l = 2.7$ m is the length of the wire, $\rho = 19.3$ g/cm^3 its mass density, $R = 100$ μm its radius, $P = M_{\rm mirr}\, g/4$ the tension, $E = 411$ kN/mm^2 the elasticity modulus and $I = \pi R^4/4$ the fiber's bending moment of inertia. According to [Gos04] each violin-mode contributes to the power spectral density of the displacement noise of each mirror.

Both torsion and violin modes modify the transition function (2.7) which makes the pendulum resonator less capable of damping seismic excitations. Fig. 6.5 shows the power spectral density of amplitude of the transmitted wave. It has been measured by generating a microwave of constant frequency on the right side of a resonance and reading the amplitude of the transmitted wave with 20 Hz. The peak at 0.3 Hz is due to the natural frequency of the mirror pendulums. The smaller peaks at higher frequencies can be caused by e.g. violin modes or oscillations of the wave guides respectively the steel frame. Due to the discrete sampling frequency, peaks at frequencies higher than 20 Hz alias into the spectrum between 0 and 10 Hz and appear as artefacts (see [Pre07]). Since it is not possible to adjust the length of the suspension wires in a way that their individual transversal frequencies are perfectly equal, beats occur due to that differences. Though according to Tab. 6.1 the frequencies of the transversal modes are far higher than the natural frequency of the mirror pendulums ($f_0 = 0.3$ Hz), they can fold back such that peaks due to violin modes appear at frequencies below the sampling frequency. A simple method of damping such violin modes has been proposed in [Gos04]. Each suspension wire can be coated with drops of materials like teflon at the antinodes of vibration. One could also think of reducing e.g. noise due to torsion modes with additional magnetic brakes. However this would complicate the setup of the experiment. Since the peaks due additional oscillation modes usually occur at high frequencies, the data can be easily cleared by averaging or by applying filter techniques. Thus the expenses of modifying the magnetic brakes would by far exceed its advantages.

6.4 Shape of the Resonance

In Chap. 2.5 it is assumed that the shape of the resonance is given by Eq. (2.11). Since the resonator is neither closed nor perfectly aligned, this equation is only an approximation. As shown in [Sch92], a resonator that is not closed leads to a resonance profile with additional tails on both sides. Furthermore a misalignment of the resonator may cause an asymmetric shape of the resonance which would bias the result of the resonance fit. In this section it is explained how the deviation of the resonance from (2.11) can be determined and how the fitted resonance frequencies can be corrected.

First of all n resonance frequencies, f_R, are measured. As explained in Chap. 2.5, each frequency is determined by sampling the resonance at m points and fitting the resonance curve (2.11) to these data. After each fit, the sum of the squared residuals

$$r^2 = \sum_{k=1}^{m} \big(U(f_k) - U_k\big)^2 = \chi^2 \cdot \sigma_U^2 \tag{6.8}$$

is calculated with f_k the frequencies and U_k the amplitudes at the m sampling points and $U(f_k)$ the expected amplitude according to Eq. (2.11). The error of an amplitude measurement is given by σ_U. If Eq. (2.11) describes the resonance profile sufficiently, the n values r^2/σ_U^2 should give a χ^2 distribution with $m-3$ degrees of freedom since 3 parameters (resonance frequency, width and maximal amplitude) are fitted. The error σ_U can be estimated by $\sigma_U = \sqrt{r^2/(m-3)}$ or it can be calculated by fitting the expected χ^2-distribution to the measured one with σ_U as an additional free parameter. Furthermore for each $k = 1 \ldots m$, the residuals $r_k = U(f_k) - U_k$ of the n fits should give a gaussian distribution with mean $\bar{r}_k = 0$ and width σ_U.

Frequency measurements have been carried out by sampling the resonance

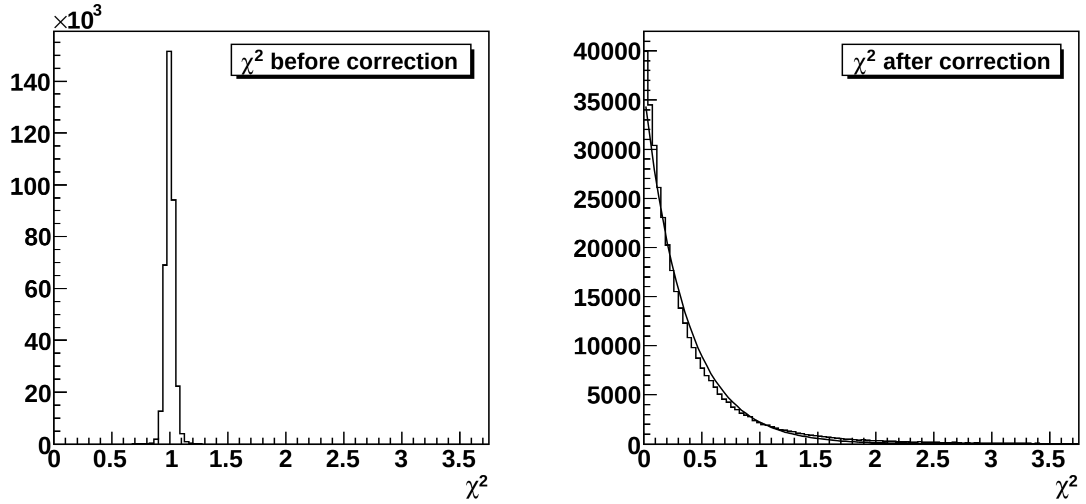

Figure 6.6: χ^2-distribution of a measurement with a 5 point fit, **left:** before and **right:** after the asymmetry correction. The solid line shows the expected distribution with 2 degrees of freedom.

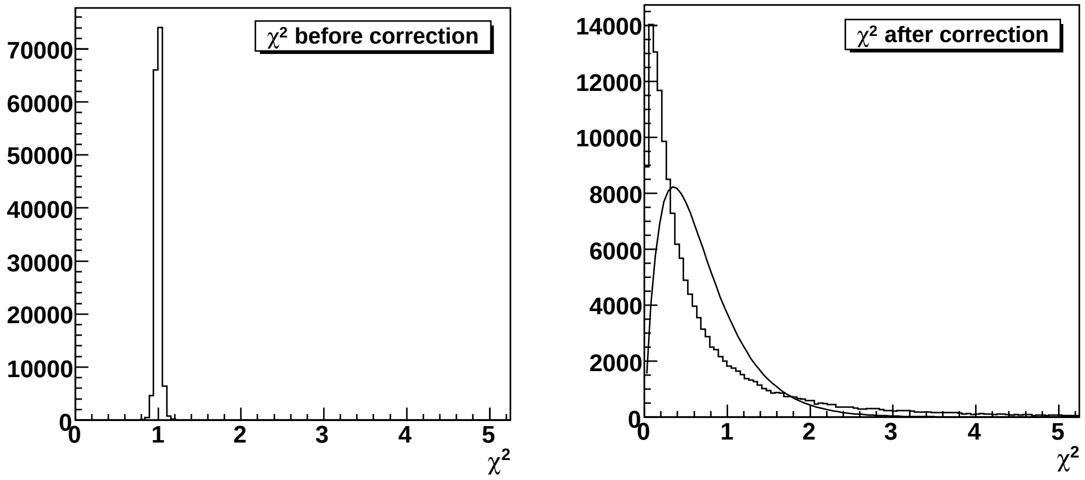

Figure 6.7: χ^2-distribution of a measurement with a 7 point fit, **left:** before and **right:** after the asymmetry correction. The solid line shows the expected distribution with 4 degrees of freedom.

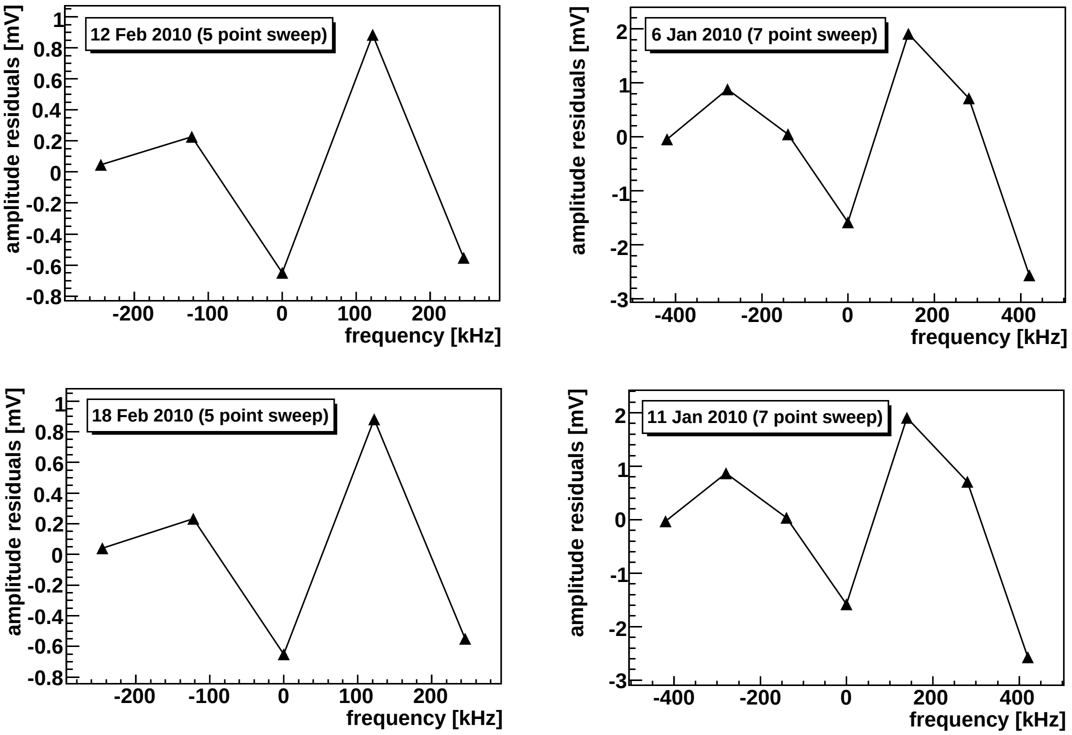

Figure 6.8: Averaged residuals of the resonance fit in the case of different measurements with 5- and 7-point fits, but with same setup and resonance mode. Since all plots show the same behaviour, the residuals indicate an asymmetry of the resonance profile.

shape at either $m = 5$ or $m = 7$ points. The left plots of Fig. 6.6 and 6.7 show the χ^2-distributions of an $m = 5$ respectively $m = 7$ measurement, assuming Eq. (2.11) as the shape of the resonance. In both cases the resonance mode with frequency 21.139 GHz, width 676 kHz and maximal amplitude 172 mV was used. Since both distributions differ largely from their expected ones, Eq. (2.11) does not describe the resonance adequately. The deviation is given by the means $\bar{r}_k$ of the residuals with $k = 1 \ldots m$. Fig. 6.8 shows these means in the case of four different measurements with either $m = 5$ or $m = 7$. The variance σ_U at each mean is about 0.03 mV in the case of $m = 5$ and 0.05 mV with $m = 7$. The pattern of the residuals looks similar in the case of the four measurements displayed in Fig. 6.8. These measurements have been carried out with the same resonance mode and the same setup of the experiment. Thus the pattern of the residuals is a real effect, maybe caused by a misalignment of the resonator.

After determining the deviation of the resonance shape from (2.11) that way, the fitted resonance frequencies can be corrected as follows. Each resonance frequency has to be fitted again. But before fitting Eq. (2.11) to the m pairs (f_k, U_k), from each amplitude U_k the corresponding mean of the residuals, $\bar{r}_k$, has

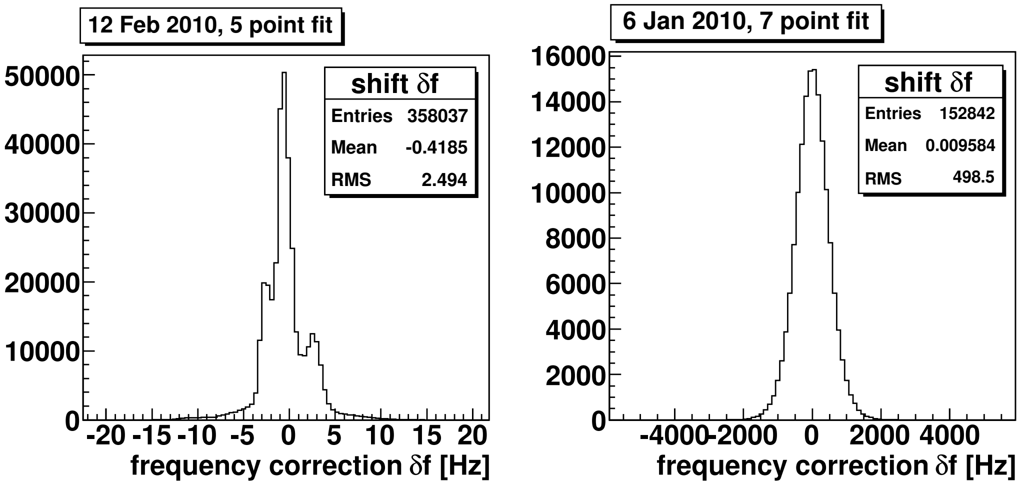

Figure 6.9: Difference, δf, between the fitted resonance frequency before and after the correction in the case of **left:** 5 point fits and **right:** 7 point fits.

to be subtracted.

Fig. 6.6, right, shows the χ^2 distribution after the correction in the case of sampling the resonance at 5-points. It is in good agreement with the expectation. Fig. 6.9, left, shows the distribution of the differences, δf, between the fitted resonance frequency before and after the correction. The frequencies shift by about -0.4 Hz. According to Chap. 2.1 and 2.5, we are only interested in frequency differences, Δf_R. Thus the correction only increases the noise of the resonance frequencies by about 2.5 Hz. Compared with the normal frequency noise, which is about 200 Hz, this additional noise is neglegible. The noise is increased because the correction assumes that the positions of the $m = 5$ sampling points f_k relative to the peak of the resonance do not change during the n fits. Since for each fit the f_k are calculated using the resonance frequency of the previous fit (see Chap. 2.5), the f_k fluctuate around the resonance peak. The assumption of non-fluctuating f_k therefore increases the noise.

In the case of sampling the resonance at 7 points, the results paint a different picture. Fig. 6.7, right, shows the χ^2 distribution after the correction. It agrees better with the expectation than before the correction but not as well as in the case of sampling at 5 points. As shown in Fig. 6.9, right, the distribution of differences between the fitted resonance frequency before and after the correction give a distribution that is centered around 0 Hz. Thus the frequency shift due to the correction is neglegible. In contrast the width of this distribution is about 500 Hz. Thus after the correction the noise is increased by the same amount. This can not be neglected anymore. Furthermore the 7 point fits lead to higher magnitudes of the residuals than the 5 point fits.

The differences between sampling the resonance at 5 and 7 points can be traced back to the fact that the 7 point fits use a larger frequency interval to estimate the resonance frequency. Since the quality of the fit is higher in the vicinity of the resonance peak than at the tails, the narrower 5 point fits lead to better results. If however both the 5 and the 7 point fits used frequency intervals of the same width, the results of course would be comparable. Since most of the measurements were carried out by sampling the resonance at 5 points, the deviation of the resonance shape from Eq. (2.11) can be neglected.

6.5 Variations of the local Gravity

The ambient pressure does not only influence the measured resonance frequency due to dielectric effects, as described in Chap. 6.7, or due to pressure induced deformations of the cryostat. A non-constant ambient pressure also influences the distribution of air around the experiment. The mass variation of the air that is usually associated with weather phenomena could be high enough to have an effect on the mirror pendulums. To study this effect in detail, the distribution of the areas of low and high pressure would have to be analysed. Furhermore the local gravity depends on the distribution of ground water or the tide of nearby rivers or seas.

The influence of all these effects on the measured resonance frequency is very complicated to estimate. But since the variation of the local gravity is slow compared with the period of the mass movement, these effects are only part of the slowly varying background that can be separated from the signal using the methods proposed in Chap. 4.2.

6.6 Brownian Motion

According to Chap. 2.8, the mirror pendulums are suspended inside a cryostat with a vacuum of 10^{-5} mbar. The remaining air particles randomly excite the mirrors to oscillate. To estimate how this effect contributes to the displacement noise of one mirror, each mirror is considered to be a grain with radius a. Its mean square deviation $\langle x^2 \rangle$ after time t is then given by

$$\langle x^2 \rangle = \frac{2kT \cdot t}{3\pi a \eta} \tag{6.9}$$

with $k_B = 1.38 \cdot 10^{-23}$ J/K the Boltzmann constant, T the temperature and $\eta \approx 17\ \mu\mathrm{Ns/m^2}$ the viscosity of the gas. The viscosity is given by

$$\eta = p \sqrt{\frac{2m}{\pi k_B T}}\, \lambda_m \tag{6.10}$$

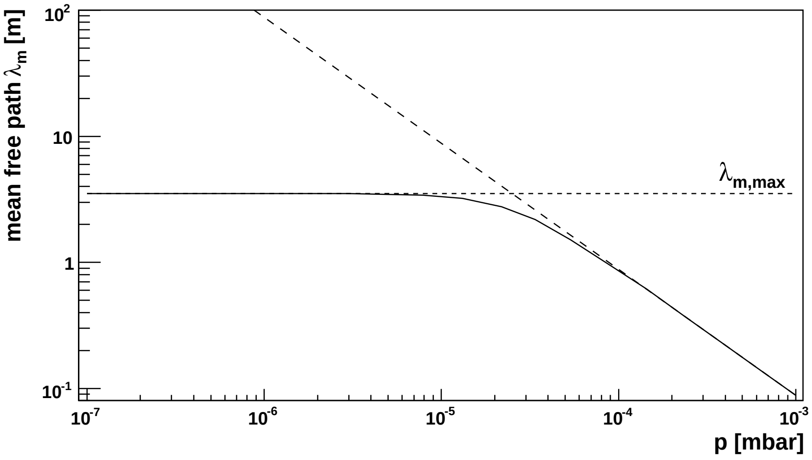

Figure 6.10: Illustration of the pressure dependence of the mean free path $\lambda_m(p)$: **Solid:** λ_m at $T = 290$ K, plotted against the pressure p. As molecules, N_2 are assumed with a diameter $d = 0.32$ nm, **Dotted:** maximal mean free path $\lambda_{\mathrm{m,max}}$ as constraint given by the vacuum vessel, **Dashed:** mean free path λ_m without this constraint.

with p the pressure, m the mass of an air molecule, d its diameter and λ_m the mean free path

$$\lambda_m = \frac{k_B T}{\sqrt{2}\pi p d^2} \tag{6.11}$$

In Fig. 6.10 the mean free path is plotted against the pressure. Combining Eq. (6.10) and (6.11) leads to the statement that the viscosity does not depend on the pressure as long as the mean free path of the air particles is much smaller than the dimensions of the cryostat. If λ_m reaches the dimensions of the cryostat, which corresponds to $p \approx 10^{-4}$ mbar, λ_m remains constant with decreasing pressure. Thus at lower pressures the viscosity (6.10) behaves like $\eta \propto p$.

Since the mirrors are suspended as pendulums, each mirror sits in a potential well. If a particle of energy $k_B T$ collides with a mirror, the potential energy will be increased, the mirror gets out of its equilibrium position and is deflected by

$$x = \sqrt{\frac{2 L k_B T}{g\, M_{\mathrm{mirr}}}} \tag{6.12}$$

with $L \approx 3$ m the pendulum length, k_B the Boltzmann constant, T the temperature, $g = 9.81$ m/s^2 the local acceleration due to gravity and M_{mirr} the mass of one mirror. Thus collisions with particles of energy $k_B T$ cause the mirror to deflect by $x = 3 \cdot 10^{-11}$ m, which corresponds to a shift of the resonance frequency of $\Delta f_R = 2$ Hz. According to Eq. (6.9), the mirrors oscillate very slowly. Since the damping due to the magnetic brakes is proportional to the oscillation speed, excitations due to Brownian motion can not be damped effectively. As a consequence, Brownian motion of the remaining air particles cause the displacement noise of the mirror distance to increase by approximately 2 Hz. Because of its gaussian character, this noise can be simply reduced by averaging the data.

6.7 Dielectric Effects

According to [Sch92] the relative dielectrical constant ε_r of the air between the mirror pendulums depends on the temperature and the ambient pressure. The dependency is given by

$$\varepsilon_r(T,p) = 1 + (\varepsilon_r - 1)\,\frac{p}{1013\,\mathrm{mbar}} \cdot \frac{273\,\mathrm{K}}{T} \tag{6.13}$$

with $\varepsilon_r = 1.00059$ in case of air. If T and p change, the corresponding variation of $\varepsilon_r(T,p)$ will be given by

$$\delta\varepsilon_r = (\varepsilon_r - 1) \cdot \frac{278\,\mathrm{K}}{1013\,\mathrm{mbar}} \cdot \frac{1}{T^2}\,(T\,\delta p - p\,\delta T) \tag{6.14}$$

with T the temperature in K, p the air pressure in mbar and δT respectively δp small changes of the temperature and the ambient pressure. The speed of light between the mirrors depends on ε_r according to $c = c_0/\sqrt{\varepsilon_r}$. Combining this relation with Eq. (2.1) leads in the first approximation to

$$f_R = \frac{c_0}{2b}\,q/\sqrt{\varepsilon_r} \tag{6.15}$$

Thus a small shift of ε causes a shift of f_R that is given by

$$\delta f_R = -\frac{f_R}{2\varepsilon_r}\,\delta\varepsilon_r \tag{6.16}$$

As shown in [Sch08], this relation is in accordance with the measurements of the resonance frequency performed in air. In order to reduce these influences, the mirror pendulums are suspended inside a thermally isolated cryostat that serves as a vacuum vessel. In that case the correlation between the resonance frequency and the ambient pressure nearly vanishes. However the frequency is still correlated with the temperature. But since in this case the temperature is also correlated with the tilt of the experiment, that variation of the resonance frequency is not caused by dielectric effects but by temperature induced changes of the resonator alignment which is mentioned in Chap. 6.1. In the case of measurements carried out using a vacuum, dielectric effects are neglegible.

6.8 Electromagnetic Induction

Fig. 6.11 shows the resonance frequency that has been measured on March 15, 2011, during a standard massage cycle of PETRA which is necessary to reduce magnetic history. The resonance frequency is correlated with the beam energy which is proportional to the current in the dipole magnets of PETRA. To study the correlation of Fig. 6.11 in detail, the different magnet circuits were ramped independently on April 21, 2010. Fig. 6.12 shows the first time derivative, dB_x/dt, of the x-component of the magnetic field that is caused by the current in the bus bars of different magnet circuits and that is measured at the position of the pendulum resonator. Furthermore it shows the resonance frequency, f_R, of the resonator that was measured at the same time. This plot reveals the relation

$$f_R \propto \frac{dB_x}{dt} \tag{6.17}$$

which also holds for the y- and z-components and can be traced back to electromagnetic induction.

The bus bars of the PETRA magnets are about $r = 10$ m away from the pendulum resonator and can be considered to be approximately parallel to the symmetry axis of the resonator. During the ramping process, the current that runs through the bus bars of the dipole magnets maximally changed with $dI/dt = 500$ A/min. Due to Ampere's law, this current produces a time dependent magnetic field that circulates around the bus bars. That causes the magnetic field in the vicinity of the pendulum resonator to change with $\mu_0/2r\pi \cdot dI/dt = 4 \cdot 10^{-7}$ T/s. Since the mirrors are conducting, this field causes a circular current of about $I_M = 0.3$ mA on the surface of each mirror. Both mirrors are exposed to a static magnetic field $B = 0.1$ T due to the magnetic brakes that are installed in order to damp the pendulum oscillations (see Chap. 2.3). This results in a Lorentz force

$$F_L = I_M \cdot l \times B = 3 \cdot 10^{-7}\mathrm{N} \tag{6.18}$$

which causes each mirror pendulum to deflect by 10^{-5} mrad resp. 30 nm. This shifts the resonance frequency, f_R, by about 2 kHz. In Eq. (6.18) $l = 1$ cm represents the length of each brake along the symmetry axis.

On the one hand the correlation between the resonance frequency and the magnetic fields of PETRA is well understood. Therefore one could try to correct the affected data as follows. First of all the part has to be subtracted that is due to dB_x/dt according to Fig. 6.12. But since the shift of the resonance frequency, Δf_R, has to be measured with an accuracy of at least 0.1 Hz, this would only be a first order correction. To reach the required accuracy, the data have to be corrected iteratively from the remaining electromagnetic influences that shift the frequency by more than 0.1 Hz. On the other hand ramping is not done very often so that only few data are affected. Thus a complex correction algorithm would

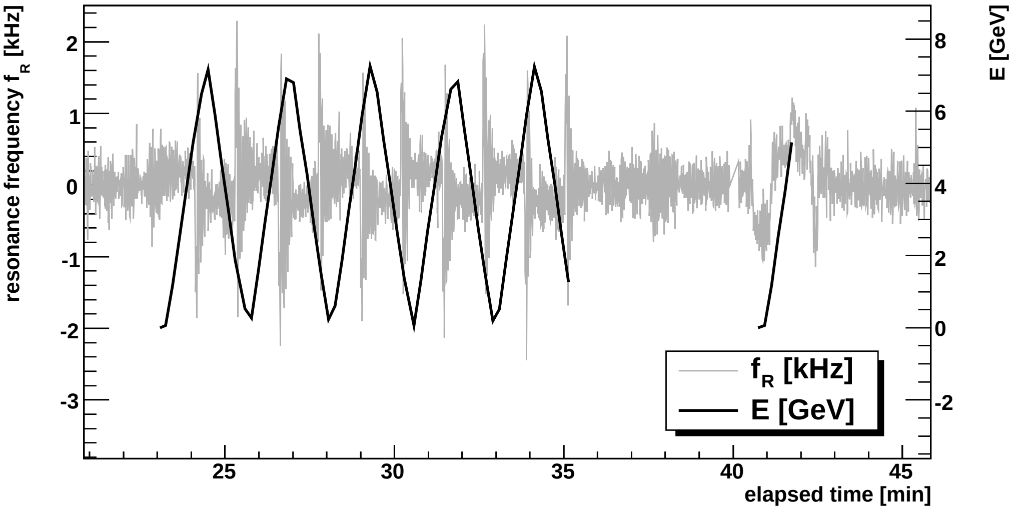

Figure 6.11: The measurement started on March 17, 2010, at 10:20, shows that the resonance frequency, f_R, of the pendulum resonator is connected with the beam energy, E, which is proportional to the dipole current of PETRA. From f_R a constant offset of about 21 GHz has been subtracted in order to increase the readability.

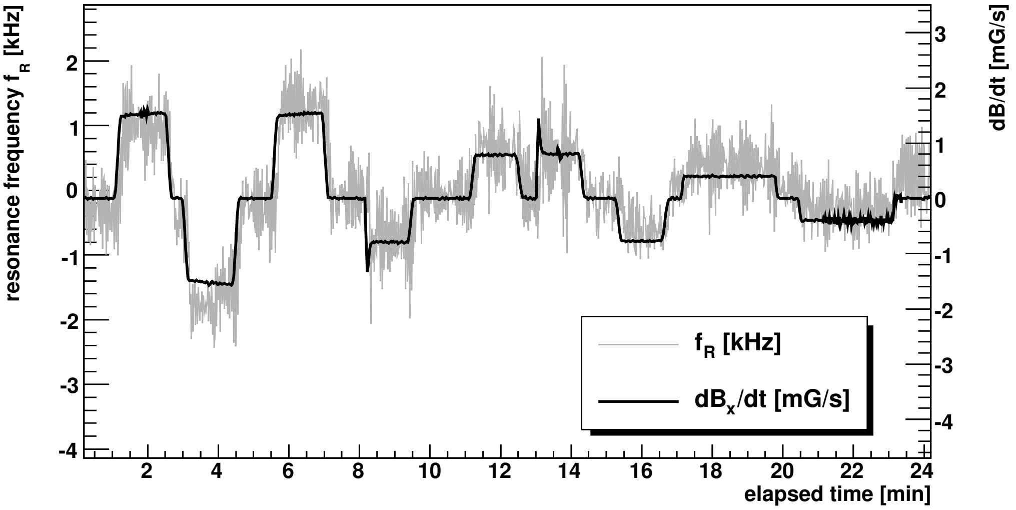

Figure 6.12: The measurement started on April 21, 2010, at 11:42, shows the correlation between the resonance frequency, f_R, and the first time derivative, dB_x/dt, of the x-component of the magnetic field caused by the ramping current of PETRA. Like in Fig. 6.11, a constant offset of about 21 GHz has been subtracted from f_R.

not be worth the effort of implemeting it. As a consequence the data measured during the ramping of the PETRA magnets are rejected.

6.9 Vacuum Effects

Fig. 6.13, upper part, shows a measurement of the resonance frequency that was started on April 5, 2010, and that can not be analysed because it is spoiled with a number of sharp peaks. The lower plot shows that the peaks of the resonance frequency are correlated with the pressure changes inside the vacuum vessel, that was measured at the same time.

On the one hand this could be a real effect which means that the pressure inside the cryostat varies with time. At the sharp peaks the vacuum suddenly improves. These sudden improvements can be caused by a malfunction of the compressor that is used to keep the angle valve open in order to maintain the vacuum during the measurement. If this compressor fails, the valve will close for a short period of time and the pressure inside the cryostat changes. According to Chap. 6.10, the mean free path of the remaining air particles at 10^{-5} mbar is of the order of the dimensions of the cryostat. The mode filter between the mirror pendulums closes the resonator up to a gap of about 1 mm. Since this gap is much smaller than the mean free path, the pressure variation propagates into the resonator with a delay. If the vacuum improves suddenly, for a short period of time the pressure outside the resonator is smaller than inside. Thus the mirrors are pulled apart and the resonance frequency decreases.

On the other hand the peaks of the vacuum plot could be artefacts due to the measurement process. According to Chap. 2.8, the vacuum is measured with a Penning gas discharge tube. Inside this tube, electrical discharges take place erratically while the vacuum is measured. To exclude this influence, the vacuum should not be measured at the same time the resonance is measured.

6.10 Frequency Jumps

Fig. 6.14 shows a measurement of the resonance frequency during September 16, 2009, that is spoiled by jumps of about 0.5 kHz. Contrary to the peaks shown in Chap. 6.9, such a jump causes the resonance frequency to change permanently. However these jumps have no effect on the amplitude and the width of the resonance which indicates that the mode remains the same. Fig. 6.15 shows the distribution of the jumps. It can be seen that jumps of large magnitude preferably occur at daytime, between 5:00 and 19:00.

First of all these jumps can be caused by sudden changes of the resonator geometry. On the one hand this could happen if the alignment of the cryostat or the frame changes. In that case the tilt measurement would also show permanent

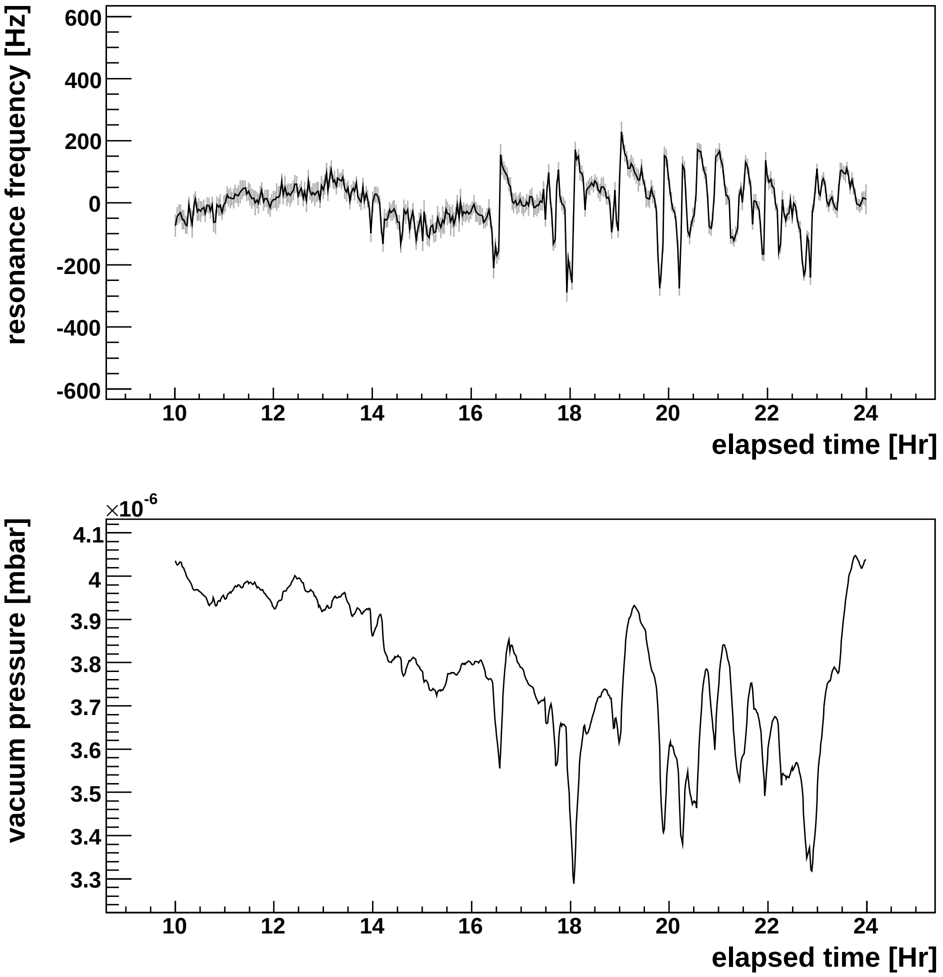

Figure 6.13: above: A measurement of the resonance frequency, started on April 5, 2010, at 23:45, after subtracting a 3-rd order background polynomial and averaging over 2 minutes, **below:** a measurement of the pressure inside the cryostat at the same time.

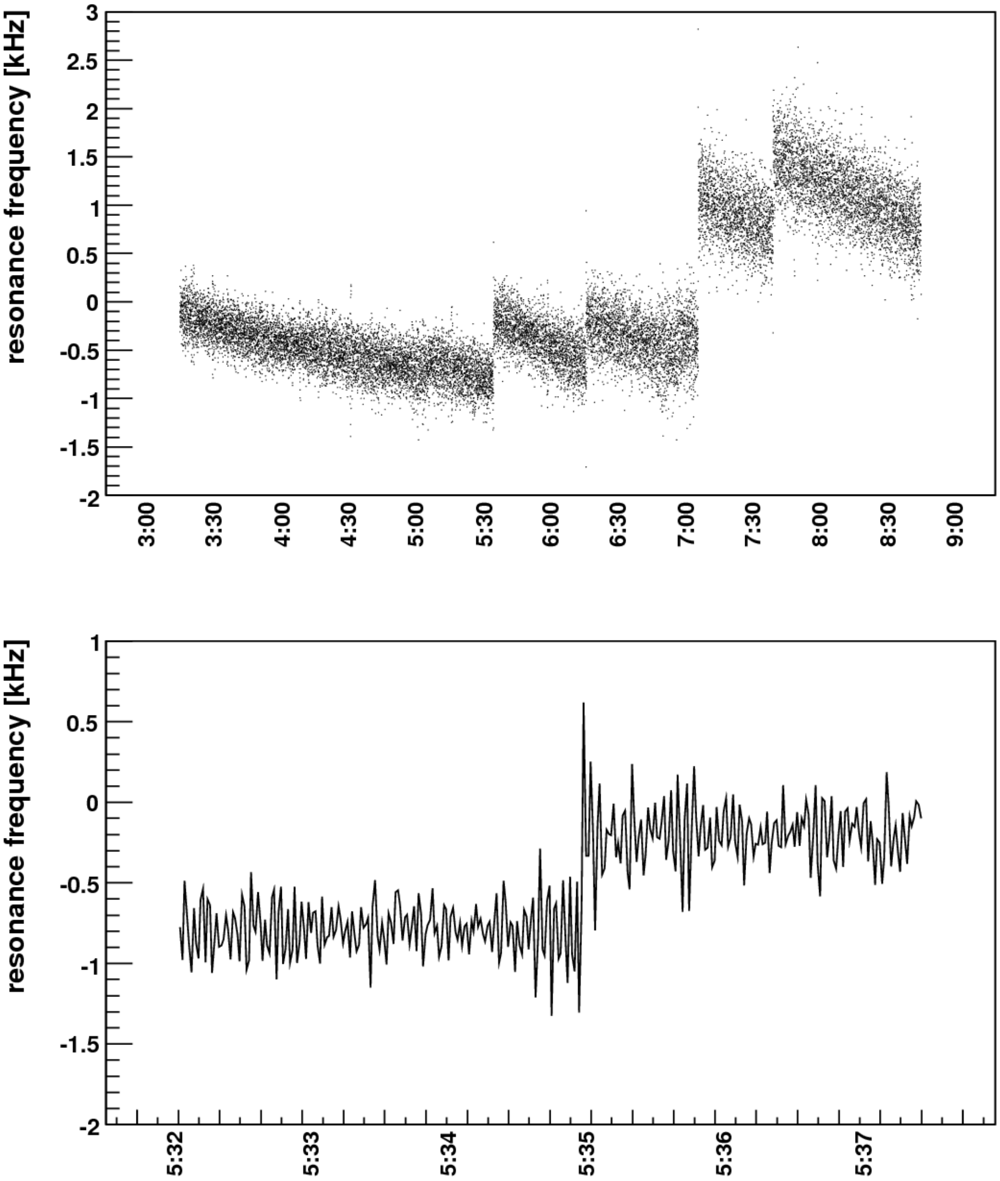

Figure 6.14: A measurement of the resonance frequency during September 16, 2009, plotted against the time: **above:** four permanent jumps of the resonance frequency of a magnitude of about 1 kHz, **below:** zoomed into the 5 minute interval around the first jump of the above plot.

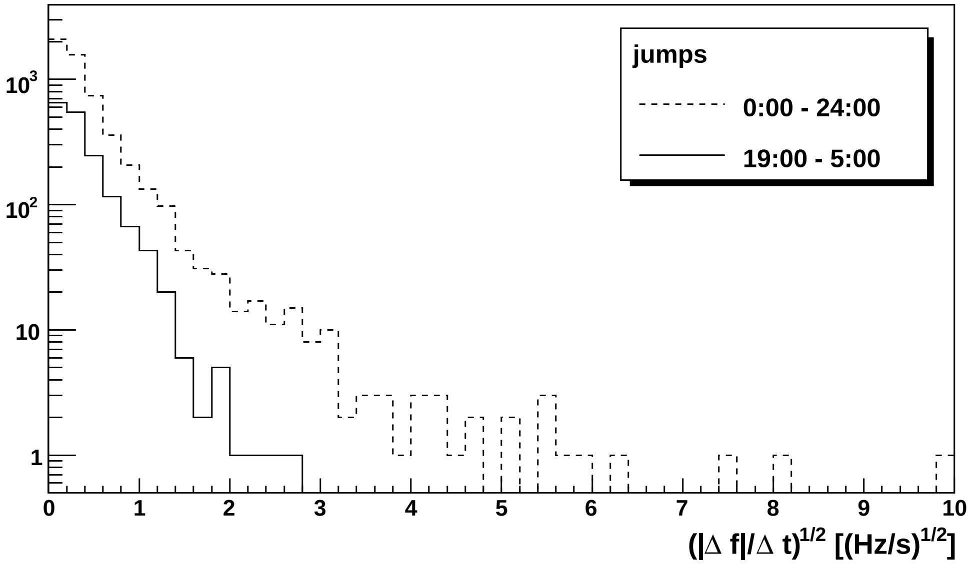

Figure 6.15: Distribution of the frequency jumps between September 2009 and February 2010, with $|\Delta f|/\Delta t$ the absolute value of the height of the jump, Δf, divided by its duration, Δt: **dotted:** all jumps, **solid:** jumps between 19:00 and 5:00.

jumps. Since no correlation can be found between the tilt and frequency jumps, this possibility has to be excluded. The resonator geometry will also change if the length of the suspension wires change due to molecular displacements or if the wires change its positions on the attachment. To suppress the latter effect, the wires are fixed by a dip of glue.

Electronics can be excluded as a source of the frequency jumps. In order to see whether the frequency generator causes the jumps due to e.g. a malfunction or an inaccuracy of the closed loop control, the Agilent HP8340b was temporarily replaced with a Rohde & Schwarz SMR40. However a difference could not be seen, neither in the number nor in the magnitude of the jumps. If the DVM that measures the amplitudes caused the jumps, a sudden jump of the measured amplitude would indeed worsen the resonance fit, but it would not translate directly into a jump of the fitted resonance frequency. Above all, the frequency jump would not be permanent in that case. Finally a surge absorber was used to protect the measurement electronics from over- or undervoltage but the jumps did not disappear. Thus sudden changes of the resonator geometry are the most likely reason for these frequency jumps.

To be able to analyse measurements affected by frequency jumps, the data are separated at the positions of the jumps into smooth intervals. If too many jumps are found within an interval the corresponding data have to be rejected.

6.11 Mechanical Instability

Between 2008 and 2010 the experiment was several times adjusted and upgraded with additional sensors to record environmental parameters. After working on the frame or on the lid of the cryostat it could be observed that the pendulums were usually excited in a way that for half an hour or longer after the modification no measurement was possible. Furthermore the resonance frequency was always very sensitive to small changes of the adjustment. Sometimes after small modifications of the adjustment measurements were not possible at all.

Fig. 6.16 shows a measurement of the resonance frequency during February 27, 2010. Two shocks caused by an earthquake can be seen. The earthquake has been identified as the one in Chile with a magnitude of 8.8. After that incident the mirror pendulums stopped their usual motion. Fig. 6.16, below, shows that during the second shock an additional oscillation with a period of $T = 30$ s appeared in the spectrum. After the earthquake the pendulums did not adiabatically return to the equilibrium as they usually did before. All further measurements were corrupt and could not be analysed.

Until that date, the croystat was suspended inside the steel frame at three points (see Fig. 6.17a). At these points damping elements were installed. A detailed description of this setup can be found in [Wal95], [Sch99] and [Kle02]. Due to the difficult alignment the three suspension points usually were not equally loaded. This led to mechanical tensions and instability. As an additional ingredient, it turned out that the damping elements at the suspension points were overloaded in a way that they could not damp seismical excitations sufficiently.

In order to increase the stability of the setup, the role of the steel frame and the suspension of the cryostat inside this frame was studied. To reduce the complexity, the cryostat was put directly on the ground without using the steel frame. This was done using three machine supports (see Fig. 6.17b). Since these supports were overloaded, the damping capabilities of this setup were even worse than the suspension of the cryostat inside the steel frame. As a result, measurements were not possible at all. After that the machine feets were replaced by ironbricks. In order to damp the oscillations of the cryostat, four pendulums were suspended from the cryostat (see Fig. 6.17c). In order to improve the damping characteristics, the bricks could be replaced by machine feets which are more flexible to adjust. If these machine supports would have active damping, further improvements could be expected.

6.12 Summary

The collection of systematics presented so far enables one to see the sensitivity of this experiment to various influences. Effects like e.g. Brownian motion are not a problem since they only increase the gaussian noise. Misalignment of the

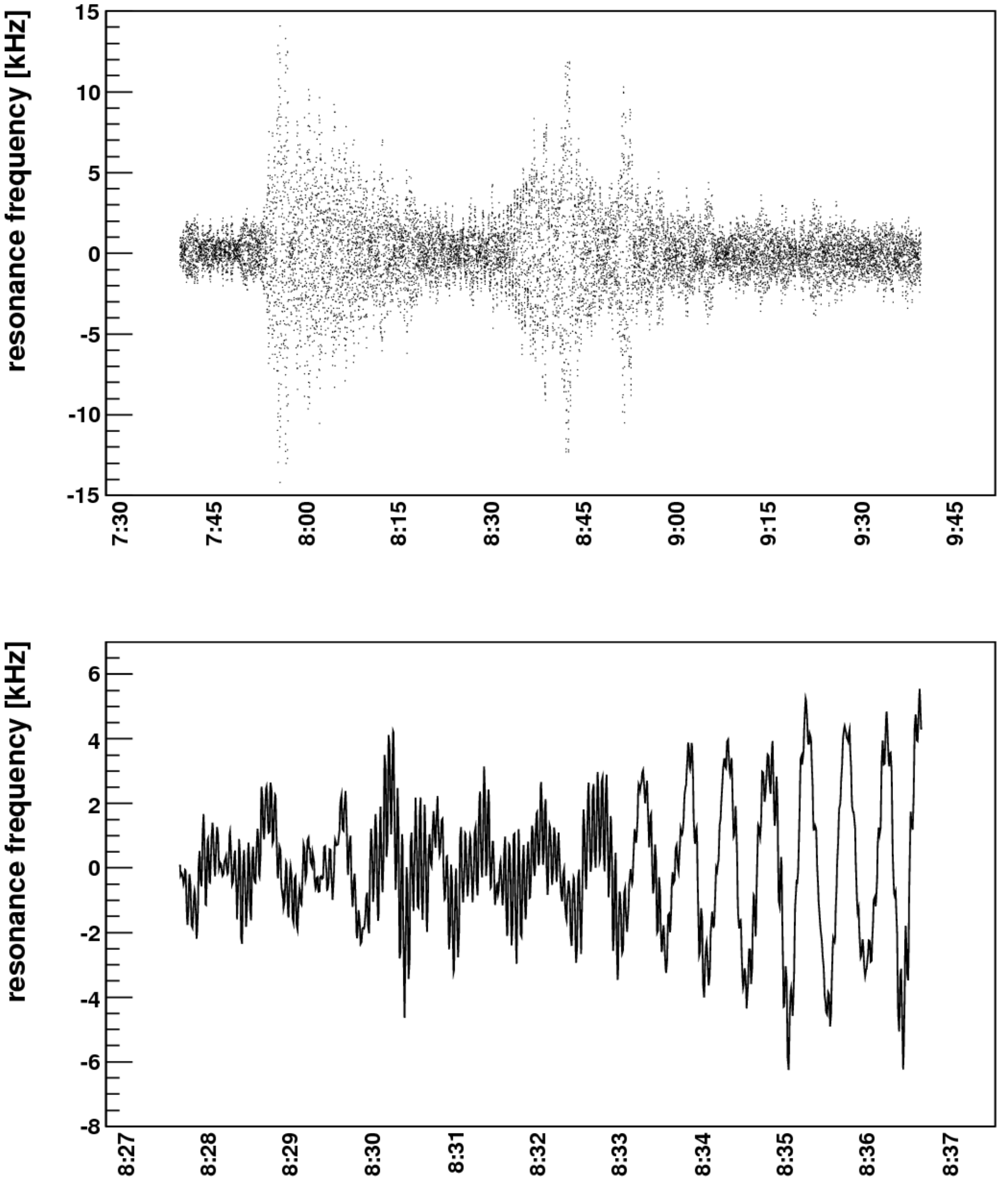

Figure 6.16: A measurement of the resonance frequency during February 27, 2010, plotted against the time: **above:** two subsequent shocks of the earthquake in Chile, **below:** zoomed into the 10 minute interval during the second shock of the above plot.

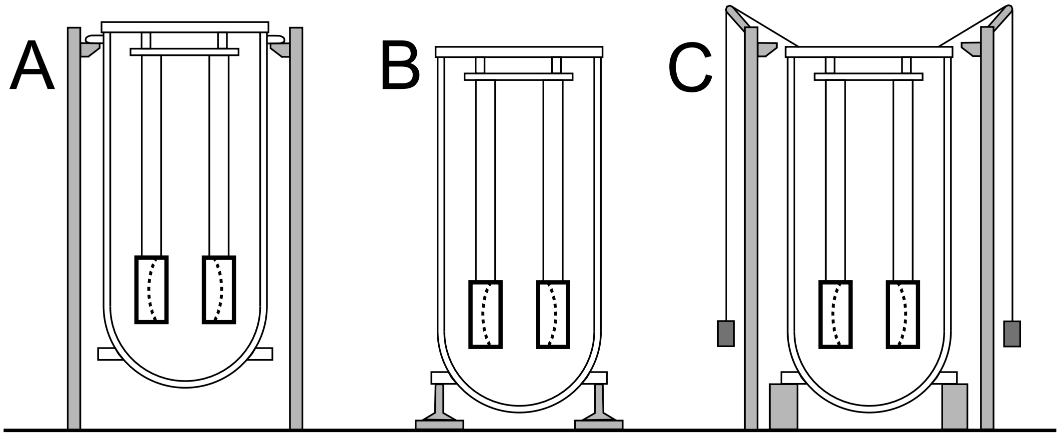

Figure 6.17: Different setups of the experiment: **A:** cryostat being suspended in the steel frame according to Chap. 2, **B:** cryostat standing on the ground using machine supports, **C:** cryostat standing on bricks and with pendulums to damp oscillations.

resonator leads to a bias but can at least be quantified. Electromagnetic induction or sudden frequency jumps result in data that can not be analysed at all. Consequently the data have to be selected carefully before analysing them.

This experiment is a modification of that one shown in [Kle02], [Sch99] and [Wal95]. The accuracy is comparable. Experiments like [Kap07], [Gun08] or [Par10] tested the Newtonian law of gravitation by measuring either G or the inverse square law. All these experiments confirm Newton's law. Their accuracy is of some orders of magnitude higher than [Kle02]. Nevertheless this does not make the experiment presented in Chap. 2 obsolete. In [Kap07] the inverse square law was tested with torsion-balance experiments. The restoring force of the pendulums was caused by the torsion of a tungsten wire, which is caused by electromagnetic forces within the material of the wire. Since this phenomenon is quite complex, it can be an additional source of systematic errors. In the case of our experiment the restoring force is caused by gravitation. In [Par10] the concept of [Kle02] was adopted and modified. They used a laser interferometer instead of a microwave resonator. This led to a more compact and robust setup.

In contrast to [Par10], [Kap07] and [Gun08], the apparatus shown in Chap. 2 has an important advantage: it can be modified without reinventing the whole experiment. The masses of the spheres, as well as their near and far positions, even the alignment of the resonator can be changed without big effort. This flexibility allows to study systematic influences in detail.

Chapter 7

Preparative Measurements

7.1 Amplitude Noise

As explained in Chap. 2.5 and 6.4, the resonance frequency is determined by fitting Eq. (2.11), page 17, to a number of amplitudes measured at equidistant frequencies around the expected resonance frequency. The amplitudes are measured as DC voltages. Thus the amplitude noise, σ_U, has contributions from electronic noise, σ_e, like pickup noise or readout noise of the DVM and from fluctuations of the resonance frequency, σ_f. While the electronic noise should be independent of the frequency at which the amplitude is measured, the contribution from the fluctuations of the resonance frequency is given by

$$\sigma_U(f) = \left| \frac{\partial U(f)}{\partial f} \right| \sigma_f \tag{7.1}$$

with σ_U the amplitude noise, $U(f)$ the expected resonance profile according to Eq. (2.11) and σ_f the noise due to the fluctuating resonance frequency. Solving Eq. (2.11) for f and replacing f in Eq. (7.1) with this expression, gives

$$\sigma_U(U) = 4U \frac{\sqrt{U(U_{\max} - U)}}{U_{\max} \cdot f_{1/2}} \sigma_f \tag{7.2}$$

with $U_{\max}$ the maximal amplitude of the resonance, $f_{1/2}$ its width and U an arbitrary amplitude between 0 and $U_{\max}$.

If the amplitude noise, σ_U, is measured at different amplitudes, U, of a resonance, it should distribute according to Eq. (7.2) as long as the noise is dominated by fluctuations of the resonance frequency. Furthermore a fit of Eq. (7.2) to the measured pairs (U, σ_U) should give the noise, σ_f, of the resonance frequency. As a cross-check, σ_f can be measured independently by calculating the rms of the fitted resonance frequencies.

Fig. 7.1 shows on the left hand side the expected profile (2.11) of the resonance

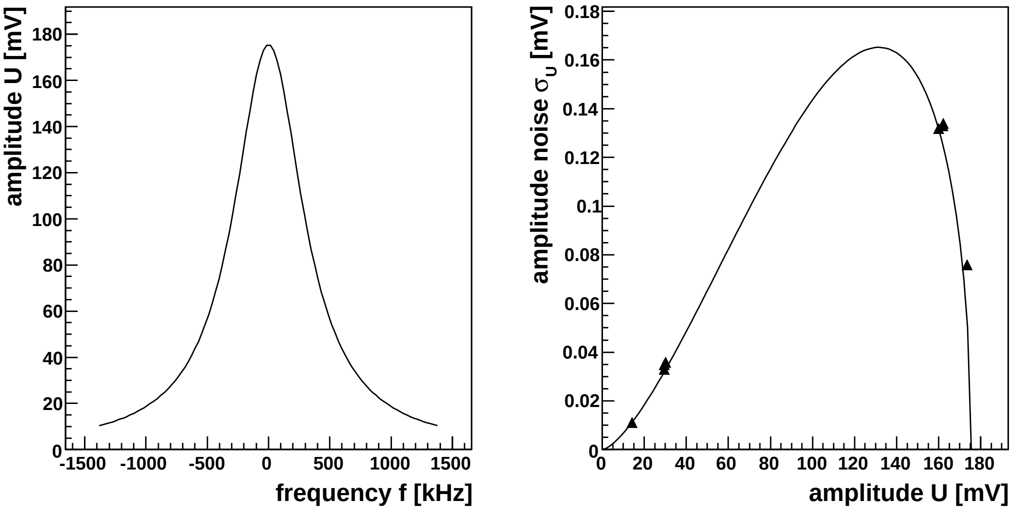

Figure 7.1: Resonance at 21.390 GHz, width 691 kHz and maximal amplitude 175 mV, **left:** the expected resonance profile and **right:** the amplitude noise, σ_U, dependent on the amplitude, U, measured and expected.

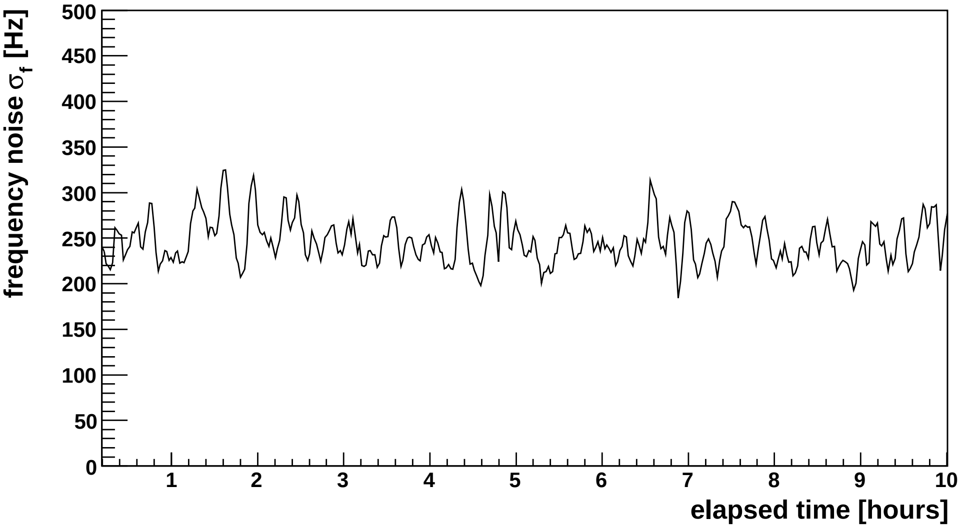

Figure 7.2: rms of fitted resonance frequencies that were measured each second (April 19, 2010). The same resonance as in Fig. 7.1 was used.

at 21.390 GHz with width 691 kHz and maximal amplitude 175 mV. The right hand side shows the associated distribution (7.2) of the amplitude noise: The six points represent the amplitude noise, σ_U, measured at amplitudes between 30 mV and 175 mV. To obtain the amplitude noise, a fixed frequency was chosen in the vicinity of the resonance frequency, the amplitude was measured each 50 ms and the rms was calculated. The solid line shows Eq. (7.2) fitted to these values. It can be seen that the measured amplitude noise, σ_U, distributes according to Eq. (7.2). Thus the amplitude noise is dominated by the noise of the resonance frequency. The readout noise of the DVM can be neglected. As an additional result of the fit, the noise of the resonance frequency is given by $\sigma_f \approx 500$ Hz.

Fig. 7.2 shows the rms, σ_f, of the fitted resonance frequencies that were measured with the same resonance mode and the same setup. This noise is about 250 Hz which seems to contradict the previous calculation. The discrepancy can be explained with the characteristics of the resonance fit. The measurement shown in Fig. 7.2 was carried out sampling the resonance shape at 5 points. Such a fit requires about 300 ms. Since the resonance frequency fluctuates during this time span, a fit already averages over the frequencies. This reduces the frequency noise by about a factor $\sqrt{5}$.

7.2 Mirror Distance

According to Chap. 2.1 and 2.2, the distance of the mirror pendulums, b, is about 24 cm. In order to calculate the expected distance shift as shown in Chap. 3, the exact value of b has to be known. It is given by

$$b = (24.0554 \pm 0.0007)\ \text{cm}$$

and has been calculated by analysing the mode spectrum of the resonator. This method leads to a more accurate result than the direct measurement which has only an accuracy of about 1 mm. In contrast to the methods proposed in [Sch92] and [Kle02], the knowledge of the knot parameters p, m, q and $N^{(\pm)}$ is not required. In the following the calculation of b is explained.

Tab. 7.1 shows the frequencies and amplitudes of the $n = 11$ largest resonance modes of the resonator. These modes have been found with the oscilloscope. First of all, the $n(n-1)/2$ mutual differences $\Delta f_k > 0$ of the n resonance frequencies of Tab. 7.1 are calculated. These differences are arranged into groups such that for each group $|\Delta f_k - \Delta f_l| \leq \Delta f_{\min}$ with Δf_k and Δf_l two arbitrary members of this group. Each group may contain several entries. The minimal difference, $\Delta f_{\min}$, is given by the smallest possible difference due to the expected mode spectrum, i.e. the frequency difference between the $N^{(+)}$ and the $N^{(-)}$ mode that share the same p, q and m with $m = 1$. Thus according to Eq. (2.1), page 13, $\Delta f_{\min}$ is

frequency [GHz]	amplitude [mV]
20.895429	11.5
20.947431	6.0
21.137756	50.0
21.168767	2.5
21.313257	3.0
21.384657	125.0
21.760858	38.0
22.007434	75.0
22.363984	6.5
22.630682	18.0
23.254004	13.0

Table 7.1: Mode spectrum of the resonator: resonance frequencies and maximal amplitudes of the resonance modes.

given by

$$\Delta f_{\mathrm{min}} = \frac{c^2}{2\pi^2 bRf_R} \tag{7.3}$$

with c the speed of light in vacuum, b and R the estimated mirror distance respectively curvature radius of the mirror surfaces and f_R the largest frequency of Tab. 7.1. If for b and R a range is specified, their maximal values will have to be used in Eq. (7.3). The arrangement of the frequency differences Δf_k into these groups can be done as follows. All possible differences $\Delta\Delta f_{kl} = \Delta f_k - \Delta f_l$ with $\Delta\Delta f_{kl} > 0$ are calculated. Then all $\Delta\Delta f_{kl} > \Delta f_{\mathrm{min}}$ are rejected. The remaining ones are sorted in ascending order. The smallest $\Delta\Delta f_{kl}$ is taken and the both associated frequency differences Δf_k and Δf_l are filled into the first group. After that the next smallest $\Delta\Delta f_{kl}$ is chosen and for each of the associated Δf_k and Δf_l it is separately tested whether they fit into the first group. This will be true e.g. for Δf_k if the first group contains only differences Δf_j with $|\Delta f_j - \Delta f_k| \leq \Delta f_{\mathrm{min}}$. If this is not true, a new group will be created with Δf_k as its first entry. The difference Δf_k will be rejected if it is already a member of a group. Then the next largest $\Delta\Delta f_{kl}$ is chosen and it is checked whether the associated frequency differences Δf_k and Δf_l fit into one of the existing groups. If one of these differences do not fit into these groups, a new group is created with the corresponding difference as its first entry. This procedure is repeated with ascending $\Delta\Delta f_{kl}$ until $\Delta\Delta f_{kl} > \Delta f_{\mathrm{min}}$.

After the $n(n-1)/2$ frequency differences have been arranged into $i = 1 \ldots m$ groups, for each the mean, $\Delta\bar{f}_i \pm \sigma_{\bar{f},i}$ of the contained differences is calculated. Groups that only contain one difference, are rejected. After that all mutual ratios

$r_{ij} \pm \sigma_{r,ij}$ of these means are calculated according to

$$r_{ij} = \frac{\Delta \bar{f}_i}{\Delta \bar{f}_j}, \qquad r_{ij} > 1 \tag{7.4}$$

The ratio r_{ij} will be rational, i.e. $r_{ij} \in \mathbb{Q}$, if the group that is associated with $\Delta \bar{f}_i$ only contains differences of frequencies whose modes only differ in the number q of the axial knots, i.e. by Δq_i. The same has to be true for $\Delta \bar{f}_j$ and Δq_j. In that case r_{ij} will also be given by

$$r_{ij} = \frac{\Delta q_i}{\Delta q_j} \tag{7.5}$$

This can be seen consulting Eq. (2.1), page 13. Since Δq_i and Δq_j can always be chosen such that every r_{ij} is rational within its error, Δq_i and Δq_j have to be restricted. This can be done as follows. The range of q is estimated by

$$q_{\min} = (f_R)_{\min} \cdot 2b/c - 1, \qquad q_{\max} = (f_R)_{\max} \cdot 2b/c + 1 \tag{7.6}$$

with c the speed of light in vacuum, b the estimated mirror distance and $(f_R)_{\min}$ and $(f_R)_{\max}$ the smallest and the largest frequency of Tab. 7.1 respectively. Since $r_{ij} > 1$, the enumerator, Δq_i, and the denominator, Δq_j, of the ratio (7.5) can be restricted to the values

$$\begin{array}{rcl} \Delta q_i & = & 2 \ldots (q_{\max} - q_{\min}) \\ \Delta q_j & = & 1 \ldots (q_{\max} - q_{\min} - 1) \\ \Delta q_i & > & \Delta q_j \end{array} \tag{7.7}$$

In order to find the rational ratios, all $r_{ij} \pm \sigma_{r,ij}$ have to be found that agree with $\Delta q_i / \Delta q_j$, with Δq_i and Δq_j restricted to (7.7). All other ratios are rejected. Combining Eq. (7.4) and (7.5) with Eq. (2.1) on page 13, for each of the remaining ratios r_{ij} the relation

$$\frac{\Delta \bar{f}_i}{\Delta q_i} = \frac{\Delta \bar{f}_j}{\Delta q_j} = \frac{c}{2b} \tag{7.8}$$

should be valid within the errors $\sigma_{\bar{f},i}/\Delta q_i$ respectively $\sigma_{\bar{f},j}/\Delta q_j$. For b, the estimated mirror distance is used. If this b is specified by a range $[b_{\min}, b_{\max}]$, the values $\Delta \bar{f}_i / \Delta q_i$ and $\Delta \bar{f}_j / \Delta q_j$ should be within $[c/2b_{\max}, c/2b_{\min}]$. Since the ratios r_{ij} are well separated, the estimated range of b can be quite large, e.g. $b \in [23.5\,\mathrm{cm}, 24.5\,\mathrm{cm}]$. Each frequency difference, $\Delta \bar{f}_i$, that is part of a ratio that satisifies Eq. (7.8), leads to an individual value of b according to

$$b_i = \frac{c}{2} \cdot \frac{\Delta q_i}{\Delta \bar{f}_i} \tag{7.9}$$

The final value of the mirror distance, b, is given by the weighted mean of all b_i

that follow from Eq. (7.9).

The algorithm presented in this section is implemented in the software HEXENWERK such that the mirror distance can be calculated automatically. As a cross check, the mirror distance has also been calculated using the mode spectra measured in [Sch92] and [Kle02]. The results are in agreement with those of [Sch92] and [Kle02].

7.3 Pendulum Frequency

The natural frequency, $\omega_0 = 2\pi f_0$, of the mirror pendulums is required to calculate the shift, Δb, of the mirror distance and the gravitational constant G (see Chap. 3.1 and 8.2). The value of f_0 can be determined by estimating the power spectrum of the time series of the resonance frequency.

In Fig. 7.3 the shaded curve shows this power spectrum: The power spectral density (PSD) is plotted against the frequency. In order to calculate this spectrum, 850 hours of resonance measurements between September 2009 and February 2010 have been evaluated. The resonace frequencies were measured with a period of 1s. These data have been separated into non-overlapping intervals of 4096 data points. For each interval the power spectrum has been calculated separately by Fourier transforming its data points. In order to prevent leakage, the data points were weighted with Slepian taper functions. This method is explained e.g. in [Pre07]. The final power spectrum, shown in Fig. 7.3, is given by the mean of all these spectra. A peak can be seen at the expected natural frequency of about 0.3 Hz. The sharp peaks at multiples of 1/60 Hz are caused by the environment measurement (see Chap. 2.6) which ran with a period of 60s. Due to an unknown electronic effect it caused every 60s a sharp peak in the time series of the resonance frequencies.

The power spectral density at frequency ω is proportional to the square of the part of the seismic noise at ω that is transmitted to the mirror distance respectively to the resonance frequency. If the seismic noise is independent of ω, the relation

$$\lambda_{\mathrm{PSD}}(\omega) \propto |H_b(\omega)|^2 \tag{7.10}$$

will be valid with $\lambda_{\mathrm{PSD}}(\omega)$ the power spectral density at ω and $H_b(\omega)$ the transition function according to Eq. (2.7), page 14. A fit of $|H_b(\omega)|^2$ to the spectrum of Fig. 7.3 around the peak gives the natural frequencies ω_{0_1} and ω_{0_2} of both mirror pendulums and their damping constants γ_1 and γ_2. The results of the fit are shown in Tab. 7.2. It can be seen that the difference of the natural frequencies is smaller than or at least comparable with the error. The same is true for the damping constants. Thus both the natural frequencies and the damping constants can be considered to be identical within the uncertainties. In the case of $\omega_{0,1}$ both the statistical and the larger systematic error are shown. The latter has been estimated by using different intervals for fitting $|H_b(\omega)|^2$ and comparing

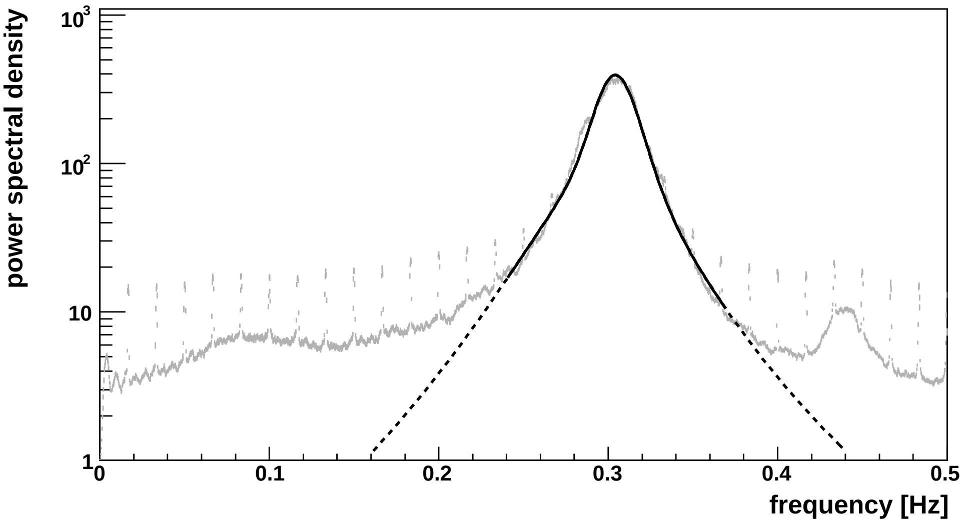

Figure 7.3: Power spectral density (PSD) of the measured resonance frequencies, plotted against the frequency: **grey:** measured, **solid line:** the fitted square, $|H_b(\omega)|^2$ of the transition function (2.7), page 14, **dotted line:** the expectation in the case of an ideal resonator.

$f_{0,1} = \omega_{0,1}/2\pi$ [Hz]	$0.30419 \pm 0.00002 \pm 0.001$
$\delta f_0 = f_{0,2} - f_{0,1}$ [Hz]	$(-6.66 \pm 0.24) \cdot 10^{-5}$
γ_1 [1/s]	0.3155 ± 0.0006
$\delta\gamma = \gamma_2 - \gamma_1$ [1/s]	$(7.213 \pm 0.021) \cdot 10^{-3}$

Table 7.2: Natural frequencies $f_{0,1}$ and $f_{0,2}$ of both mirror pendulums and their damping constants γ_1 and γ_2. The values of $f_{0,2}$ respectively γ_2 are shown relative to $f_{0,1}$ and γ_1. The second error of f_0 is the systematic error.

the different results of $\omega_{0,1}$.

According to Fig. 7.3, the expected $|H_b(\omega)|^2$ is in good agreement with the PSD around the resonance peak. Thus the seismic noise does not depend on the excitation frequency in the vicinity of the peak. Since the mirrors can oscillate in more complex ways than mathematical pendulums, the resonator is less capable of damping seismics than the ideal resonator with the transition function (2.7). As a consequence of this, the spectrum deviates from its expectation on both sides. The additional peak at 0.44 Hz can be caused by torsion modes or oscillations of the wave guides respectively the steel frame. Thus $|H_b(\omega)|^2$ is only a good approximation of the power spectral density in the vicinity of the resonance peak at $f_0 \approx 0.3$ Hz.

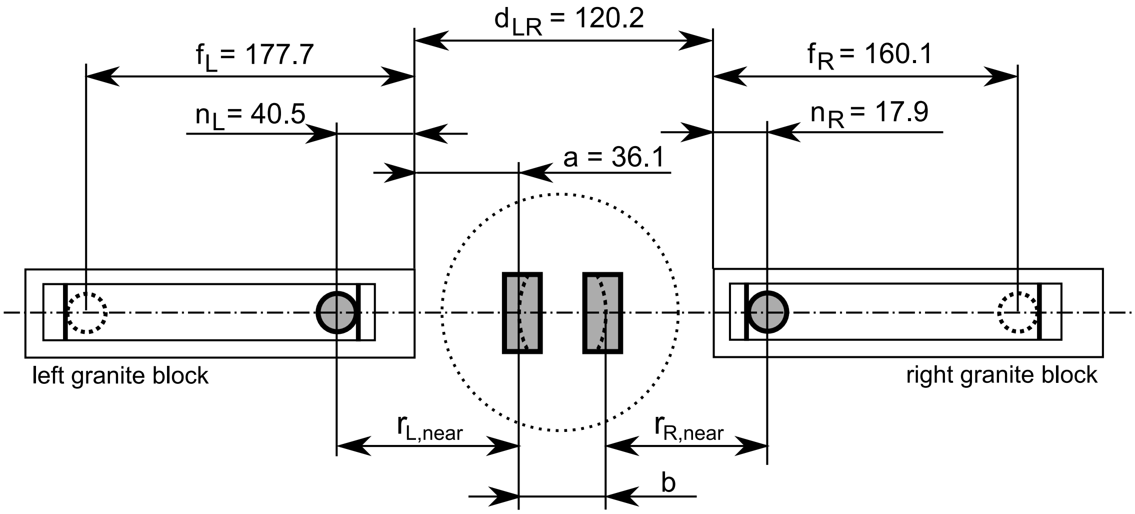

Figure 7.4: Schematic top view of the experiment: near and far positions of the spheres in mm, relative to the mirror pendulums. The mirror distance is given by $b = (24.0554 \pm 0.0007)$ cm. Its calculation is explained in Chap. 7.2.

7.4 Positions of the Spheres

Fig. 7.4 shows a simplified top view of the experiment. The mirror pendulums are surrounded by a dotted circle which illustrates the cryostat. Guide rails are mounted on the left and on the right granite block. Both spheres are in the near position. The distances f_L, n_L, f_R, n_R and d_{LR} have been measured with an accuracy of 1 mm. According to Chap. 7.2 the mirror distance is given by $b = (24.0554 \pm 0.0007)$ cm. The distance a between the left granite block and the center of mass of its adjacent mirror pendulum was measured with an estimated accuracy of about 5 mm. According to Fig. 7.4, the near distances are given by $r_{\mathrm{L,near}} = 76.6$ cm and $r_{\mathrm{R,near}} = 77.9$ cm. Thus both values can only be determined with an accuracy of at least 5 mm. Furthermore $r_{\mathrm{L,near}}$ and $r_{\mathrm{R,near}}$ are correlated due to the constraint

$$r_{\mathrm{L,near}} + r_{\mathrm{R,near}} + b = d_{LR} + n_L + n_R \tag{7.11}$$

In order to check the measured values of Fig. 7.4 for correctness, the distances $r_{\mathrm{L,near}}$ and $r_{\mathrm{R,near}}$ have also been determined with the following method: The frequency shift, i.e. the change of the mirror distance, was measured using different configurations. The spheres were moved either symmetrically on both sides, or a sphere was moved only on the left or on the right hand side. Furthermore spheres of different masses were used. All in all about $n \approx 50$ measurements were evaluated, each several hours long. If the validity of Fig. 7.4 is assumed, one will be able to calculate the expected frequency shift, as explained in Chap. 3, for each of these configurations. On the other hand one can assume the distances $r_{\mathrm{L,near}}$

	$r_{\mathrm{L,near}}$ [cm]	$r_{\mathrm{R,near}}$ [cm]	χ^2/n
with constraint	76.3 ± 0.8	77.7 ± 0.8	1.98
without constraint	78.2 ± 1.2	79.9 ± 1.3	1.47

Table 7.3: Values of $r_{\mathrm{L,near}}$ and $r_{\mathrm{R,near}}$ (see Fig. 7.4) obtained from fitting the expected to the measured frequency shifts with $r_{\mathrm{L,near}}$ and $r_{\mathrm{R,near}}$ as the free parameters. $n \approx 50$ measurements with different configurations have been analysed. The fit was done both with and without the constraint given by Eq. (7.11). The validity of Newton's law has been assumed.

and $r_{\mathrm{R,near}}$ to be unknown. In that case their values can be determined by fitting the expected frequency shifts to the measured ones using $r_{\mathrm{L,near}}$ and $r_{\mathrm{R,near}}$ as free parameters. This fit has been done both with and without the constraint given by Eq. (7.11). The results can be found in Tab. 7.3. The measured frequency shifts have been obtained with the analysis method A2 because it is faster than e.g. the methods A1 or A3. Nevertheless its results are consistent with the other methods (see e.g. Chap. 5 and 8). As can be seen in Tab. 7.3, the fit without the constraint leads to values with errors larger than 1 cm. Using the constraint (7.11) leads to smaller errors. Furthermore the values of $r_{\mathrm{L,near}}$ and $r_{\mathrm{R,near}}$ are in better agreement with Fig. 7.4. Nonetheless the fit without the constraint results in a better χ^2 which indicates that the data seem to favour the fit without the constraint. This points to inconsistencies regarding the measured distances shown in Fig. 7.4. In order to be conservative, an error of 1 cm is assumed for $r_{\mathrm{L,near}}$ and $r_{\mathrm{R,near}}$. Thus their values are given by $r_{\mathrm{L,near}} = (76.6 \pm 1.0)$ cm and $r_{\mathrm{R,near}} = (77.9 \pm 1.0)$ cm

Chapter 8

Results

Chap. 8.1 summarizes the shifts of the resonance frequency that have been measured using 1, 2.92 and 9.02 kg spheres. In Chap. 8.2 the gravitational constant G is calculated from these frequency shifts in order to check the measurements and the analysis methods for correctness. In Chap. 8.3 the measured frequency shifts are finally compared with the predictions of Newton's law and MOND.

8.1 Measured Frequency Shifts

Tab. 8.1 and Fig. 8.1 show the measured frequency shift, Δf_R, dependent on the mass of the spheres that have been moved between the far to the near positions. To get these results, measurements between September 2009 and February 2010 have been evaluated using the analysis methods explained in Chap. 4.4.

The results of the first three analyisis methods agree with each other separately for 1, 2.92 and 9.02 kg spheres. The following discussions will be based on the results of the method A1 if nothing else is mentioned. The other methods are used as control methods.

method	Δf_R(1.0kg) [Hz]	Δf_R(2.92kg) [Hz]	Δf_R(9.02kg) [Hz]
A1	2.06 ± 0.25	6.09 ± 0.24	18.65 ± 0.40
A2	2.00 ± 0.44	6.25 ± 0.32	19.12 ± 0.54
A3	2.06 ± 0.38	6.19 ± 0.34	18.53 ± 0.60
A4	2.94 ± 0.48	6.36 ± 0.31	19.30 ± 0.61
A5	1.72 ± 0.59	6.31 ± 0.36	20.09 ± 0.51
A6	1.60 ± 0.25	5.63 ± 0.23	17.00 ± 0.56

Table 8.1: Frequency shift, Δf_R, caused by the movement of 1, 2.92 and 9.02 kg spheres, separately plotted for the different analysis methods of Chap. 4.4.

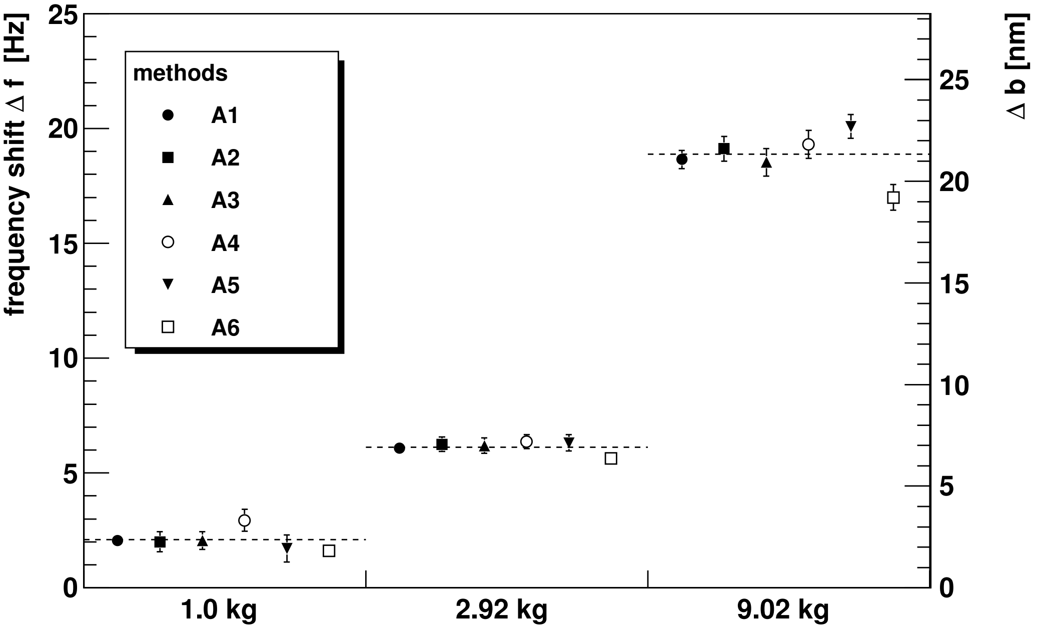

Figure 8.1: Measured frequency shift, Δf_R, and the associated change, Δb, of the mirror distance, dependent on the mass of the spheres and on the analysis method. The dotted lines show the expectations in the case of Newton's law.

8.2 Calculation of the gravitational Constant

In order to check the results of Tab. 8.1 for correctness, the gravitational constant G is calculated using these frequency shifts. Since the decision between Newon's law and MOND has not yet been reached, an assumption has to be made in order to continue: In the case of the measurements with 9.02 kg spheres, the acceleration on a mirror pendulum caused by its adjacent sphere at the near position ($r_{\text{near}} \approx 70$ cm) is far higher than the threshold acceleration a_0 of MOND (see e.g. Fig. 3.5, page 28). Tab. 8.8, page 91, shows the expected frequency shifts dependent on the law of gravitation. In the case of 9.02 kg measurements the predictions of MOND agree within 1% with Newton's law as long as MOND 5 is excluded. Thus G can be calculated with an accuracy of 1% by

$$G = \beta \frac{\Delta f_R}{\Delta b^*} \tag{8.1}$$

with β the conversion factor (2.5) on page 13, Δf_R the measured shift of the resonance frequency according to Tab. 8.1, Δb^* the expected change of the mirror distance (3.7) on page 23 in the case of Newton's law divided by G. As shown in Chap. 3.4, the mirrors can not be treated like point masses. Thus Δb^* has

method	$G \pm \sigma_G$ [10^{-11} m^3/kg s^{-2}]	$G - G_{\mathrm{CODATA}}$
A1	6.57 ± 0.22	-0.46σ
A2	6.74 ± 0.26	0.24σ
A3	6.53 ± 0.27	-0.53σ
A4	6.80 ± 0.28	0.45σ
A5	7.08 ± 0.26	1.56σ
A6	5.99 ± 0.25	-2.71σ

Table 8.2: Gravitational constant G and its error σ_G, calculated using Eq. (8.1) and the frequency shifts, Δf_R, in Tab. 8.1 in the case of the 9.02 kg measurements.

source	value	contrib. to σ_G/G [%]
near position of the spheres $r_{\mathrm{L,near}}$, $r_{\mathrm{R,near}}$ [cm]	76.6, 77.9, ±1.0	2.53
frequency shift Δf [Hz]	18.65 ± 0.40	2.14
pendulum frequency f_0 [Hz]	0.304 ± 0.001	0.66
correction due to numerical integration (scale factor)	0.976 ± 0.002	0.2
mass of the spheres [kg]	9.02 ± 0.01	0.11
mirror distance b [cm]	24.0554 ± 0.0007	0.007
resonance frequency [GHz]	21.3905 ± 0.0001	0.0005
curvature radius R [cm]	57.99 ± 0.01	0.0005

Table 8.3: Sources of systematic uncertainties and their contributions to the error of G which has been calculated in Tab. 8.2.

been integrated numerically. The calculation of the expected shift of the mirror distance is explained in Chap. 3.

The result $G = (6.57 \pm 0.24) \cdot 10^{-11}$ m^3/kg s^{-2} agrees within 1σ with the official CODATA value of 2010, $G = 6.67384(80) \cdot 10^{-11}$ m^3/kgs^2 (see [Nis11]). Tab. 8.2 summarizes results of all analysis methods. The G values have been calculated according to Eq. (8.1) using the frequency shifts of Tab. 8.1 in the case of measurements with 9.02 kg spheres. The results of the first three control methods also agree within 1σ with the official G value. The results of the methods A5 and A6 deviate by 1.6σ repectively 2.7σ. As can be seen in Tab. 8.1 and Fig. 8.1, the frequency shifts of method A6 are systematically smaller than the results of the other methods. The deviation is always about 3σ. The large spread of the results obtained by different analysis methods points to unknown systematics, e.g. caused by highly irregular noise during the frequency measurement. This presently is the most severe limitation of the experiment.

method	$\alpha(2.92, 1.0)$	$\alpha(9.02, 1.0)$	$\alpha(9.02, 2.92)$
A1	2.96 ± 0.38	9.05 ± 1.12	3.06 ± 0.14
A2	3.12 ± 0.71	9.56 ± 2.12	3.06 ± 0.18
A3	3.00 ± 0.58	9.00 ± 1.68	2.99 ± 0.19
A4	2.16 ± 0.37	6.56 ± 1.09	3.03 ± 0.18
A5	3.67 ± 1.28	11.68 ± 4.02	3.18 ± 0.20
A6	3.52 ± 0.57	10.62 ± 1.70	3.02 ± 0.16

Table 8.4: Ratios $\alpha(M_1, M_2) = \Delta f_R(M_1)/\Delta f_R(M_2)$ of the measured frequency shifts according to Tab. 8.1.

8.3 Newton vs. MOND

There are several ways of comparing the measurements with the predictions of Newton's law and MOND. One can either compare the measured frequency shifts Δf_R with their expectations or the ratios $\Delta f_R(M_1)/\Delta f_R(M_2)$, with M_1 and M_2 either 1.0, 2.92 or 9.02 kg. In the case of Newton's law, the relation

$$\frac{\Delta f_R(M_1)}{\Delta f_R(M_2)} = \frac{\Delta b(M_1)}{\Delta b(M_2)} = \frac{M_1}{M_2} \tag{8.2}$$

must apply. In the case of MOND, Eq. (8.2) is not valid anymore and the ratio $\Delta f_R(M_1)/\Delta f_R(M_2)$ additionally depends on the interpolation function. As an advantage the comparison of ratios does not require the knowledge of the factor β (see Eq. 2.5, page 13), which allows to convert frequency shifts into changes of the mirror distance or vice versa. This conversion factor depends on the resonance mode and the geometry of the resonator. Therefore it can be an additional source of systematic errors. If the frequency shifts are compared with their expectations, the factor β is needed to convert the expected change of the mirror distance into a frequency shift. Furthermore the ratios are not biased by systematics that rescale the measured frequency shift (see e.g. Chap. 6.1).

First of all the ratios of frequency shifts are compared. Tab. 8.4 shows the ratios of the measured frequency shifts (see Tab. 8.1). In Tab. 8.5 the expected ratios are shown, dependent on the law of gravitation. The measured ratio $\alpha(9.02, 2.92)$ has the smallest spread. The largest spread can be found in the case of $\alpha(9.02, 1.0)$. Tab. 8.6 shows the deviation of the measured mean ratio from the expected ratio in units of the standard deviation σ of the measured ratio, dependent on the law of gravitation. Only the ratio $\alpha(9.02, 2.92)$ can be used to make a statement. The ratio agrees within 1σ with Newton's law and MOND version 2, 3 and 4. MOND version 5 shows the largest deviation with $\approx 2\sigma$, which is not significant.

According to Tab. 8.6 the ratios do not provide sufficient information to

	$\alpha(2.92, 1.0)$	$\alpha(9.02, 1.0)$	$\alpha(9.02, 2.92)$
Newton	2.92 ± 0.09	9.00 ± 0.28	3.09 ± 0.10
MOND 1	3.03 ± 0.10	9.99 ± 0.33	3.29 ± 0.11
MOND 2	2.59 ± 0.08	7.65 ± 0.23	2.96 ± 0.09
MOND 3	2.84 ± 0.08	8.73 ± 0.26	3.08 ± 0.10
MOND 4	2.88 ± 0.09	9.05 ± 0.28	3.15 ± 0.10
MOND 5	2.50 ± 0.07	6.93 ± 0.20	2.77 ± 0.08

Table 8.5: Expected ratios $\alpha(M_1, M_2) = \Delta b(M_1)/\Delta b(M_2)$, dependend on the masses and on the gravitation law. The MOND laws are numbered according to the interpolation function $\mu(x)$ in Tab. 8.7. The errors are due to the uncertainty of the positions and the masses of the spheres. The positions can only be determined with an accuracy of 1 cm, the masses with 10 g.

	$\alpha(2.92, 1.0)$	$\alpha(9.02, 1.0)$	$\alpha(9.02, 2.92)$
Newton	0.11σ	0.05σ	-0.18σ
MOND 1	-0.20σ	-0.84σ	-1.69σ
MOND 2	0.98σ	1.26σ	0.76σ
MOND 3	0.32σ	0.29σ	-0.12σ
MOND 4	0.21σ	0.01σ	-0.61σ
MOND 5	1.20σ	1.90σ	2.13σ

Table 8.6: Deviations of the ratios of Tab. 8.4 from the expected ratios of Tab. 8.5 in units of the standard deviation σ of the measured ratios.

no.	$\mu(x)$	Literature
1	$x/\sqrt{1+x^2}$	[Mil83]
2	$x/(1+x)$	[Fam05]
3	$\frac{6}{\pi^2}x \int_0^{\frac{\pi^2}{6x}} \frac{z}{e^z-1}\,dz$	[Li10]
4	$y\,\frac{1-y^3}{1-y^4}, \quad y=y(x)$	[Men10]
5	$\frac{\sqrt{1+4x}-1}{\sqrt{1+4x}+1}$	[Bek05]

Table 8.7: MOND interpolation functions $\mu(x)$, associated with the five MOND laws in Tab. 8.5 and 8.6. In Chap. 1.2, page 5, these functions are presented in detail. There also the calculation of interpolation function 4 is explained.

distinguish Newton's law fom MOND. Therefore the frequency shifts are now compared with their expectations. Fig. 8.2 shows the measured frequency shifts, Δf (see Tab. 8.1) for $M = 1$, 2.92 and 9.02 kg spheres, divided by the mass M of the spheres. The bands show the expectations $\Delta f/M$ plotted against M, dependent on the law of gravitation. The MOND laws are numbered according to Tab. 8.7. In the case of Newton's law, the expectation does not depend on M because $\Delta f \propto M$.

Tab. 8.9 shows the χ^2 values associated with the different laws of gravitation which are given by

$$\chi^2 = \sum_M \frac{(\Delta f(M) - \Delta f_{\mathrm{exp}}(M))^2}{\sigma^2_{\Delta f} + \sigma^2_{\Delta f,\mathrm{exp}}} \tag{8.3}$$

with $M = 1$, 2.92 and 9.02 kg, $\Delta f(M) \pm \sigma_{\Delta f}$ the measured frequency shift in the case of spheres of mass M and $\Delta f_{\mathrm{exp}} \pm \sigma_{\Delta f,\mathrm{exp}}$ the expectation dependent on the law of gravitation. The χ^2 value should be around 3. Newton's law, MOND 3 and MOND 4 fit very well. MOND 1 is disfavoured. MOND 5 can be excluded which is in accordance with [Fam05].

8.4 Conclusion

The results of Tab. 8.1 respectively Tab. 8.4 have been obtained by using six different analysis methods, which are explained in Chap. 4.4. The individual results of these methods are statistically correlated because they are based on

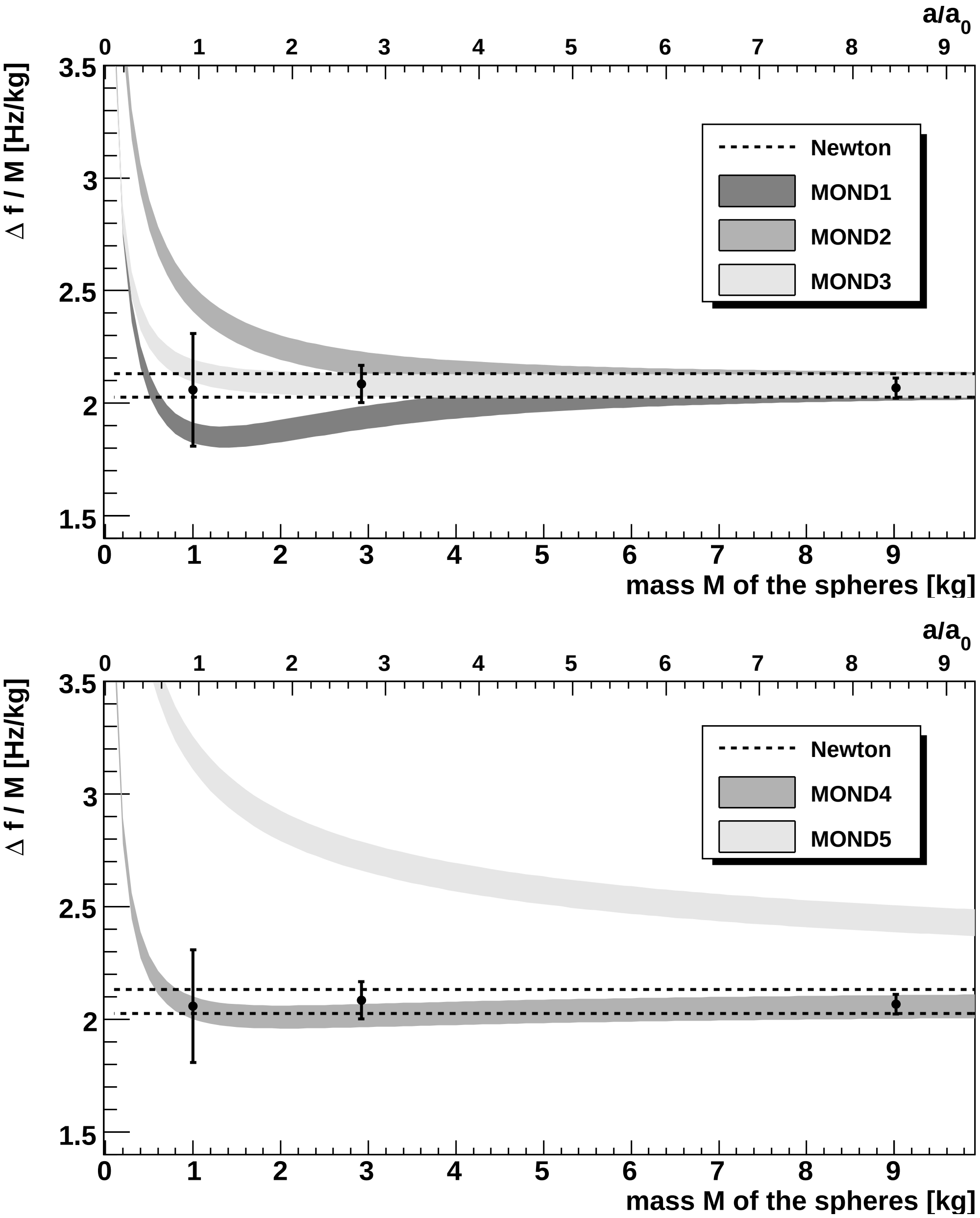

Figure 8.2: Measured and expected frequency shift, Δf, divided by the mass of the spheres, M, plotted against M. The points show the measured frequency shift for 1, 2.9 and 9.02 kg spheres. The dotted and the shaded bands show the expectation dependent on the law of gravitation according to Tab. 8.7.

	Δf(1.0kg) [Hz]	Δf(2.92kg) [Hz]	Δf(9.02kg) [Hz]
Newton	2.10 ± 0.04	6.12 ± 0.13	18.88 ± 0.42
MOND 1	1.88 ± 0.04	5.69 ± 0.13	18.74 ± 0.42
MOND 2	2.48 ± 0.05	6.41 ± 0.14	18.96 ± 0.42
MOND 3	2.16 ± 0.04	6.12 ± 0.13	18.86 ± 0.42
MOND 4	2.06 ± 0.04	5.93 ± 0.13	18.65 ± 0.42
MOND 5	3.20 ± 0.06	8.02 ± 0.17	22.21 ± 0.48

Table 8.8: Expected frequency shift, Δf_{exp}, dependent on the mass of the spheres and on the law of gravitation.

	Newton	MOND				
		1	2	3	4	5
χ^2	0.16	2.54	4.10	0.28	0.32	87.16

Table 8.9: χ^2 according to Eq. (8.3), calculated for Newton's law and for the five MOND versions of Tab. 8.7.

the same data. The spread reflects the influence of systematic effects on different analysis methods.

The accelerations of the mirror pendulums caused by the 1 and 3 kg spheres are in the vicinity of the threshold acceleration of MOND $a_0 \approx 1.2 \cdot 10^{-10}$ m/s^2. In this regime Newton's law has been tested and confirmed with an accuracy of 3%. The MOND versions 1, 3 and 4 can not be distinguished from Newton's law. MOND 2 is disfavoured and MOND 5 can be excluded. Even if the precision could be increased, MOND in general could not be rejected by this experiment because one could not exclude the existence of an interpolation function $\mu(x)$ that make MOND indistinguishable from Newton within the errors.

If the prediction of MOND deviates from that of Newton's law only in the case of weak gravitational fields, this experiment, which is carried out in the gravitational field of earth, will not be able to distinguish between these both laws, even if MOND was realised in Nature (see Chap. 1.4). This experiment can only check whether Newton is correct in the case of small relative accelerations. Since it is still an open question whether graviational fields have to be weak to measure deviations from Newton, this experiment provides at least an opportunity to answer this question.

Bibliography

[Aka74] **Akaike, H.:** *A new look at the statistical model identification,* IEEE Transactions on Automatic Control 19 (6), 1974, p. 716 - 723

[Bek05] **Bekenstein, J.:** *Relativistic gravitation theory for the modified Newtonian dynamics paradigm,* Physical Review D, 70, 2004

[Bek06] **Bekenstein, J.:** *The modified Newtonian dynamics - MOND and its implications for new physics,* Contemporary Physics, Vol. 47, No. 6, 2006, p. 387 - 403

[Bis95] **Bishop, C.M.:** *Neural Networks for Pattern Recognition,* Oxford University Press, 1995

[Blo98] **Blobel, V.; Lohrmann, E.:** *Statistische und numerische Methoden der Datenanalyse,* Teubner, Stuttgart/Leipzig 1998

[Cap09] **Capozziello, S.; et al.:** *Testing an exact $f(R)$-gravity model at Galactic and local scales,* 2009, arXiv:0906.5430v2 [gr-qc]

[Fam05] **Famaey, B.; Binney, J.:** *Modified Newtonian Dynamics in the Milky Way,* 2005, arXiv:astro-ph/0506723v2

[Gos04] **Gossler, S.:** *The suspension systems of the interferometric gravitational-wave detector GEO 600,* Dissertation, Fachbereich Physik, Universität Hannover 2004.

[Gun08] **Gundlach, J.H.; et al.:** *Test of the Equivalence Principle Using a Rotating Torsion Balance,* Physical Review Letters, 100, 041101, 2008

[Her11] **Hernandez, X.; et al.:** *The Breakdown of Classical Gravity?,* 2011, arXiv:1105.1873v1 [astro-ph.GA]

[Kap07] **Kapner, D.J.; et al.:** *Tests of the Gravitational Inverse-Square Law below the Dark-Energy Length Scale,* Physical Review Letters, 98, 021101, 2007

[Kle99] **Kleinevoss, U.; et al.:** *Absolut measurement of the Newtonian force and a determination of G,* Measurement Science and Technology, 10, 1999, p. 492-494

[Kle02] **Kleinevoss, U.:** *Bestimmung der Newtonschen Gravitationskonstanten G,* WUB-DIS 2002-2, 2002

[Li10] **Li, X.; Chang, Z.:** *Debye entropic force and modified Newtonian dynamics,* 2010, arxiv:1005.1169v1 [hep-th]

[McG11] **McGaugh, S.:** *A Novel Test of the Modified Newtonian Dynamics with Gas Rich Galaxies,* 2011, arXiv:1102.3913v1 [astro-ph.CO]

[Men10] **Mendoza, S.; et al.:** *A non-relativistic approach to extended Newtonian gravity: tests and predictions across astrophysical scales,* 2010, arxiv:1006.5037v2 [astro-ph.GA]

[Mil83] **Milgrom, M.:** *A modification of the Newtonian dynamics as a possible alternative to the hidden mass hypothesis,* Astrophysical Journal 270, 1983, p. 365

[Mil94] **Milgrom, M.:** *Dynamics with a Nonstandard Inertia-Acceleration Relation: An Alternative to Dark Matter in Galactic Systems,* Annals of Physics 229, 1994, p. 384-415

[Mil01] **Milgrom, M.:** *MOND - a pedagocial review,* 2001,
arXiv:0112069v1 [astro-ph]

[Mil11] **Milgrom, M.:** *MD or DM? Modified dynamics at low accelerations vs dark matter,* 2011,
arXiv:1101.5122v1 [astro-ph.CO]

[Nis11] **National Institute of Standards and Technology (NIST):** *The NIST Reference on Constants, Units and Uncertainty,* July 2011
http://physics.nist.gov/cuu/Constants/index.html

[Par10] **Parks, H.V.; Faller, J.E.:** *A Simple Pendulum Determination of the Gravitational Constant,* 2010, arXiv:1008.3203v3 [physics.class-ph]

[Paz11] **Pazy, E.:** *Particles statistics of the holographic screen lead to Modified Newtonian Dynamics (MOND),* 2011,
arXiv:1106.4108v1 [hep-th]

[Pre07] **Press, W. H.; et al.:** *Numerical Recipes: The Art of Scientific Computing,* 3rd edition, Cambridge University Press 2007

[Sca06] **Scarpa, R.:** *Modified Newtonian Dynamics, an Introductory Review,* 2006,
arXiv:astro-ph/0601478v1

[Sch78] **Schwarz, G.:** *Estimating the dimension of a model,* Annals of Statistics 6, No. 2, 1978, p. 461-464
doi:10.1214/aos/1176344136

[Sch08] **Schubert, S.:** *Überprüfung des Newtonschen Gravitationsgesetzes bei kleinen Werten der Beschleunigung,* DESY-THESIS-2008-025, Hamburg 2008

[Sch99] **Schumacher, A.:** *Systematische Untersuchungen zur Messung der Newtonschen Gravitationskonstanten mit einem Pendelresonator,* WUB-DIS 99-13, Wuppertal 1999

[Sch92] **Schurr, J.:** *Eine neue Methode zum Test des Newtonschen Gravitationsgesetzes,* WUB-DIS 92-8, Wuppertal 1992

[Tul77] **Tully, R.B.; Fisher, J.R.:** *A New Method of Determining Distances to Galaxies,* Astronomy and Astrophysics 54, No. 3, 1977, p. 661-673

[Ver10] **Verlinde, E.:** *On the Origin of Gravity and the Laws of Newton,* 2010, arxiv:1001.0785v1 [hep-th]

[Wal95] **Walesch, H.:** *Test des Newtonschen Gravitationsgesetzes und die präzise Bestimmung von G,* WUB-DIS 95-4, Wuppertal 1995

[Zwi33] **Zwicky, F.:** *Die Rotverschiebung von extragalaktischen Nebeln,* Helvetica Physica Acta, Vol. 6, 1933, S. 110-127

Acknowledgements

Here I would like to thank all those who contributed, every one in his own special way, to the accomplishment of this thesis. These are:

- Prof. Hinrich Meyer who was always willing to discuss the experiment from a broader point of view and who gave me the space that I needed so much to ‚recalibrate‘ my soul in order to work productively. He also made sure that my supply lines were never cutted such that I was always connected to a continuous stream of the newest papers related with my thesis.

- Prof. Erich Lohrmann who escorted me some steps deeper into the jungle of numbers and statistics and showed me tools with which I could defend myself against the most dreadful creatures that jumped out from behind the trees greedy for pulling me into the darkness.

- Eberhard Wuensch who was always a very enthusiastic supporter of the experiment and with whom I could have uplifting conversations about the possibilities of personality development in disadvantageous places like e.g. dark and humid cellar offices. He also played the role of an ambassador of the rich universe beyond physics.

- Carsten Niebuhr, Bernd Loehr, Wulfrin Bartel and Gerhard Kempf who spent a significant amount of their time supporting the experiment in all matters and who established regular meetings even though some of them sometimes suffered from inconveniences due to unreliable means of transport. Furthermore Carsten Niebuhr was never tired of preaching for a systematic approach which finally put the whole experiment on a firm footing.

- Alexandre Glazov and again Carsten Niebuhr, Erich Lohrmann and Bernd Loehr for contributing substantially to the progress of our data analysis by developing the control analysis methods and with whom I could always discuss about that topic. Erich Lohrmann also developed the Monte Carlo generator such that the analysis methods could be checked for consistency.

- Torsten Külper, Sven Karstensen, Uwe Cornett and Marian Gil who created a speciose zoo of mechanical or electronical gadgets which helped to domesticate the furious beast that is also called experiment in this thesis.

- Carsten Muhl, Hans-Juergen Seidel, Dieter Habercorn and Volkert Sturm who constructed other important parts of the experiment

- Jörn Schaffran (FLA) who helped us to install and maintain the vacuum system, patiently answering the same questions again and again.

- Wilhelm Bialowons and the DESY seismic group who provided us with adequate measurement devices and valuable advices
- Henning-Christof Weddig and the DESY HF group (MHF-p) who supported us in the case of HF problems.
- All other groups of DESY that are part of the infrastructure and that gave us technical support.
- Christoph Kasemann from the Max-Planck-Institut für Radioastronomie in Bonn who lent us the R&S SMR40 frequency generator for test purposes
- Sebastian Johnert and my former office mates Danny Bot and Joachim Franck with whom I could talk about anything. Thanks to them I also benefited from delightful bus respectively boat trips which made the long and always fatiguing travel to work bearable for me.
- Iraida whose unexpected emergence let suddenly the sun arise and illuminate my life which was enveloped in abysmal darkness before.